

**COMBINED EXPERIMENTAL AND NUMERICAL STUDY OF
SPONTANEOUS DYNAMIC RUPTURE ON FRICTIONAL INTERFACES**

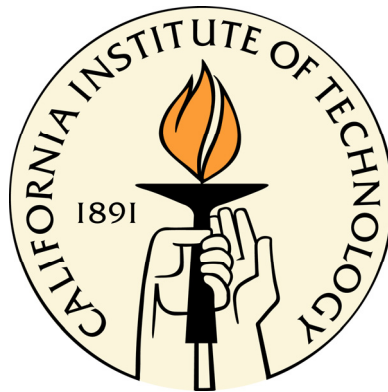
Thesis by

Xiao Lu

In Partial Fulfillment of the Requirements

for the Degree of

Doctor of Philosophy



California Institute of Technology

Pasadena, California

2009

(Defended October 14, 2008)

© 2009

Xiao Lu

All Rights Reserved

Acknowledgements

My foremost gratitude goes to my two advisors, Professor Nadia Lapusta and Professor Ares J. Rosakis, whose advice, guidance, and friendship have been invaluable during my years at Caltech. Prof. Lapusta provided unwavering support while allowing me complete freedom to pursue my ideas. Her enthusiasm about research and vast knowledge in solid mechanics motivated me to carry the commitment and fascination in science not only for my PhD study but also for my upcoming career. I thank Prof. Lapusta for so much I learned from her lectures and our collaborations. I also deeply appreciate her understanding and suggestions during several transitions in my personal life. Prof. Rosakis offered the grounding of my understanding in experimental mechanics, and his encouragement constantly motivated me to explore the new boundaries in my work. He is the mentor who is always willing to share my happiness of the new discovery and give me sincere trust and tolerance at bad times. His intuition and innovative mindset are unequalled, and always inspire new ideas in our research group. Looking back at every step I took forward since my arrival to Caltech, I'm so fortunate to have outstanding advisors like Prof. Lapusta and Prof. Rosakis as my source of wisdom. I believe this memorable experience will be savored throughout my entire life.

I also would like to thank all other members of my thesis committee, Professors Guruswami Ravichandran, Professor James Knowles, Professor Jean-Philippe Avouac, and Professor Chiara Daraio for reviewing my thesis and providing valuable suggestions and

iv

criticism. Prof. Ravichandran was very accessible when I sought help and suggestions on experiments. I benefited tremendously from attending his group meetings as an apprentice in my first years. I'm also grateful to Professor Yonggang Huang, who gave me insightful advice during his visit to Caltech.

I owe many thanks to the current and former members of our research group. I thank Mike Mello for devoting so much time to teach me experimental methodologies and for giving me valuable advice on my career development. I'm so fortunate to have him as my colleague and mentor. Mike's passion and dedication to the perfection of work are truly influential to me in many ways. I enjoy the long friendship with Yi Liu very much and the discussion with him often gave me new perspectives in research. I'm very grateful to Yoshihiro Kaneko, who shared with me his expertise in earthquake sciences. I am deeply thankful to Kaiwen Xia and George Lykotrafitis for their great contribution to the development of the laboratory where I completed this work. And it is such a great pleasure to work with Ting Chen, Leslie Lamberson, Harsha Bhat, Ajay Harish, Chi Wan Ko, Veronica Eliasson, and Hiroyuki Noda. Special thanks to Donna Mojahedi for her help during my thesis study. Her professionalism and dedication make the group well organized. I also want to extend my appreciation to Petros Arakelian, who was always very helpful and resourceful. I thank Joe Haggerty, Ali Kiani, and Bradley St. John for their help in the machine shop.

I also want to express my sincere appreciation to my fellow students and postdocs. Dr. Jianheng Zhao and Dr. Xue Feng selflessly shared their experience and knowledge with

me during their visit to Caltech. I benefited from the refreshing discussions with them many times, which helped me advance my research significantly. People who I also want to thank for their help and friendship include Min Tao, Benny Poon, Christian Franck, Rongjing Zhang, Theresa Kidd, Samantha Daly, Sharlotte Kramer, Winston Jackson, Vijay Chalivendra, Soonsung Hong, Yong Hao, Xin Guo, Zhiyi Li, Changling Pang, and many others.

If there were anybody who deserves a special award, it would have to be my wife Pingping Yao. Thanks to her for always being there to support me to go through all the ups and downs. My daughter Serene Lu and the upcoming second baby are the brightest color in my life, always bringing joy and surprises to me. Also I would like to thank my parents and parents-in-law in China, who have been supporting me unconditionally.

Abstract

The process of spontaneous dynamic frictional sliding along the interface of two elastic solids is of great interest to a number of disciplines in engineering and sciences. Applications include frictional rupture processes in earthquakes, delamination of layered composite materials, and sliding between soft membranes in biological systems. The transient nature of rupture dynamics presents an array of fascinating yet challenging questions, including the nucleation process, the mechanism of interface failure, and the speed and mode of rupture propagation.

This thesis presents such a combined experimental and theoretical study aimed at understanding the conditions for selecting pulse-like vs. crack-like rupture modes and subshear vs. supershear rupture speeds. There are two major contributions in this work. The first one is high-resolution experimental study of the rupture modes on a frictional interface. The study presents first experimental observations of spontaneous pulse-like ruptures in a homogeneous linear-elastic setting that mimics crustal earthquakes, reveals how different rupture modes are selected based on the level of fault prestress, demonstrates that both rupture modes can transition to supershear speeds, and advocates, based on comparison with theoretical studies, importance of velocity-weakening friction for earthquake dynamics. The second major contribution is the numerical modeling of the rupture experiments that reveal the importance of the rupture nucleation mechanism and friction formulations. The modeling of sub-Rayleigh to supershear transition has demonstrated the in-

fluence of rupture nucleation mechanism on supershear transition distance, as well as on the mechanism of supershear transition. The modeling of pulse-like to crack-like rupture mode transition has confirmed the necessity of velocity weakening friction for producing pulse-like rupture to match the experimental observations.

Table of Contents

Acknowledgements	iii
Abstract.....	vi
Table of Contents	viii
List of Illustrations and Tables	x
Chapter 1: Introduction	1
Chapter 2: Numerical Analysis of Supershear Transition Regimes in Rupture Experiments: the Effect of Nucleation Conditions and Friction Parameters	13
2.1 Introduction	13
2.2 Model for simulating supershear transition.....	20
2.3 Simulations of supershear transition for the seismic ratio $s = 0.5$ ($f_d = 0.2$)	27
2.3.1 Comparison of experimental and simulated transition distances for the parameters of Xia et al. (2004)	27
2.3.2 Rupture evolution and direct supershear transition at the rupture tip.....	33
2.3.3 Set of parameters that fits experimental data	36
2.3.4 Dependence of supershear transition on parameters of the rupture initiation procedure.....	39
2.3.5 Dominance of the direct supershear transition for the seismic ratio $s = 0.5$ ($f_d = 0.2$)	44
2.4 Simulations of supershear transition for the seismic ratio $s = 1.0$ ($f_d = 0.34$).....	45
2.4.1 Good agreement between experimental and simulated transition distances for pressure-independent $D_c = 1 \mu\text{m}$	46
2.4.2 Supershear transition by the Burridge-Andrews (daughter-crack) mechanism.....	49
2.4.3 Simulations with pressure-dependent D_c	52
2.4.4 Dependence of supershear transition on parameters of the rupture initiation procedure and cases with the direct supershear transition.....	53
2.5 Discussion of the two parameter regimes.....	56
2.6 Conclusions	62
Chapter 3: Rupture Modes in Laboratory Earthquakes: Effect of Fault Prestress and Nucleation Conditions.....	66
3.1 Introduction.....	66
3.2 Experimental design.....	67
3.2.1 Configuration that mimics crustal earthquakes.....	67
3.2.2 Mechanism of rupture nucleation	70
3.2.3 Surface preparation for specimens.....	71
3.2.4 High-resolution diagnostics: dynamic photoelasticity and laser velocimetry	73
3.3 Experimental measurements and their interpretation.....	74

3.3.1	Measurements of particle velocity and full-field photoelastic snapshots	74
3.3.2	Criteria for determining rupture initiation and locking times	78
3.3.3	Three-dimensional (3D) effect of the plate thickness	80
3.4	Experimental observations of systematic variation from pulse-like to crack-like rupture modes	84
3.4.1	Variation of rupture mode with nondimensional shear prestress	84
3.4.2	Variation of rupture mode with the compressive load	87
3.4.3	Collective analysis of rupture duration	89
3.5	Qualitative agreement between the experimentally observed rupture modes and theoretical predictions based on velocity-weakening friction	91
3.6	Effect of nucleation procedure	98
3.6.1	Measurements of fault-normal motion	98
3.6.2	Influence of nucleation strength	103
3.7	Rupture speeds of pulse-like and crack-like modes	104
3.7.1	Observations of supershear pulses and cracks	105
3.7.2	Evolution of rupture speeds for supershear pulses and cracks	109
3.8	Map of rupture modes and speeds under a range of experimental conditions	111
3.9	Conclusions	115
Chapter 4: Numerical Analysis of Rupture Mode Variation with Slip-weakening Friction and Rate-and-state Friction		118
4.1	Introduction	118
4.2	Difficulty of simulating pulse-like ruptures using slip-weakening friction	119
4.3	Simulating rupture mode variation with enhanced rate-and-state friction	125
4.3.1	Experimental measurements of rate-and-state friction parameters on Homalite interfaces	126
4.3.2	Comparison of experimental and simulated rupture modes	136
4.4	Conclusions and discussions	153
Chapter 5: Future Work		156
5.1	Localized Friction Measurement at High Slip Rates	156
5.2	Quantification of the Wire Explosion	162
5.3	Effect of Inhomogeneities and Complex Fault Geometries on Rupture Dynamics	165
References		172

List of Illustrations and Tables

Figure 2.1: Our model for simulations of supershear transition. Motivated by the experimental setup of Xia *et al.*, 2004 (left panel), we consider a planar interface in a thin plate (middle panel). The interface is prestressed both in compression, with $\sigma_0 = P \cos^2 \alpha$, and in shear, with $\tau_0 = P \sin \alpha \cos \alpha$. For $\alpha = 25^\circ$ used in the experiments, $\tau_0 / \sigma_0 = 0.47$. The rupture is initiated by applying a transient reduction $\Delta\sigma$ of normal stress in the region of length $2a$ in the middle of the interface for time T_o . The time dependence of the normal-stress reduction is shown in the top of the right panel. The interface is governed by linear slip-weakening friction (bottom of the right panel) with the static coefficient $f_s = 0.6$. Several values of the dynamic friction coefficient f_d and critical slip D_c are considered... 15

Figure 2.2: Simulation results for $f_d = 0.2$, $\Delta\sigma = 5$ MPa, $a = 3$ mm, and $T_o = 5$ μ s. **(a)**

The dependence of supershear transition distances L on the compression P obtained in our simulations with pressure-independent $D_c = 10$ μ m (the solid red curve). The experimental results (dots), the results with pressure-independent $D_c = 10$ μ m (and hence $L \sim P^{-1}$) from Xia et al. (2004) (the blue dashed curve), and the results with pressure-dependent $D_c \propto P^{-1/2}$ ($L \sim P^{-3/2}$) from Xia et al. (2004) (the violet double-dashed curve) are given for comparison. **(b)** An attempt to better fit experimental results in our simulations by incorporating pressure-dependent $D_c \propto P^{-1/2}$ with $D_c =$

10 μm for $P = 15 \text{ MPa}$ (the solid red curve). In this case, rupture arrests for $P < 12 \text{ MPa}$. **(c) and (d)** Rupture 30

Figure 2.3: An illustration of the direct supershear transition at the rupture tip. **(a) and (b)**

Snapshots of sliding velocity and normalized shear stress before and after supershear transition for the simulation of Fig. 2.2c. The shear stress peak traveling with the shear wave speed in front of the main rupture has not yet reached the static friction strength and no daughter crack is initiated. Instead, supershear transition occurs right at the rupture tip as its speed directly jumps from the Rayleigh wave speed to a supershear speed. **(c)** Locations of the shear wave front and rupture tip when supershear transition occurs for the case of Fig. 2.2a. We see that, for all P , the location of supershear transition is behind the shear wave peak. 35

Figure 2.4: Simulation results for $f_d = 0.2$ with a set of parameters that provides a better

fit to experimental transition distances. **(a) and (b)** The dependence of the simulated supershear transition distances L on the compression P (solid red curve) for $D_c = 13 \mu\text{m}$ (panel a) and $D_c \propto P^{-1/2}$ with $D_c = 13 \mu\text{m}$ for $P = 9 \text{ MPa}$ (panel b), with $a = 5 \text{ mm}$, $\Delta\sigma = 5 \text{ MPa}$, and $T_o = 5 \mu\text{s}$. The overall fit is improved in comparison to Figs. 2a and 2b; the segmentation of the simulated curves is discussed in the text. The results of Xia *et al.* (2004) are shown for the same parameters as in Fig. 2.2a, for comparison. **(c) and (d)** Rupture speed vs. the location of the rupture tip in the case of pressure-independent $D_c = \dots\dots\dots 38$

Figure 2.5: Dependence of transition distances on the parameters of the initiation

procedure for the case of $f_d = 0.2$ and pressure-independent $D_c = 13 \mu\text{m}$. The reference set of the rupture initiation parameters is that of Fig. 2.4a, $a = 5 \text{ mm}$, $\Delta\sigma$

= 5 MPa, and $T_o = 5 \mu s$. In each panel, one of these parameters is varied and the results are shown for simulations with different values of: (a) the half size a of the rupture initiation procedure, (b) normal stress reduction $\Delta\sigma$, and (c) duration T_o . In each panel, the blue dashed line gives transition distances for the largest value of the parameter studied, and that line has two branches for lower values of P . The two branches correspond to a failed attempt to transi..... 41

Figure 2.6: A representative case with two supershear transition stages, for $f_d = 0.2$, $D_c = 13 \mu m$, $a = 5 mm$, $\Delta\sigma = 5.5 MPa$, and $T_o = 5 \mu s$. **(a)** Rupture speed vs. the location of the rupture tip for $P = 9 MPa$. The failed and successful attempt of supershear transition are marked by a solid blue circle and square, respectively, and blue dotted lines. **(b)** The dependence of transition distances on P . Plotting both the failed and the successful attempt results in two branches for lower values of P 43

Figure 2.7: Simulation results for $f_d = 0.34$, pressure-independent $D_c = 1 \mu m$, $\Delta\sigma = 3 MPa$, $a = 0.8 mm$, and $T_o = 5 \mu s$. **(a)** The dependence of supershear transition distances L on the compression P in our simulations (the solid red curve). The simulations fit the experimental results (shown as dots) quite well. The transition distances based on the work of Andrews (1976) and the subsequent analysis of Xia et al. (2004) with the pressure-independent $D_c = 1 \mu m$ (and hence $L \sim P^{-1}$) are 30%-50% larger (dashed blue curve). Note that the vertical axis has a different range compared to Fig. 2.2a, 2.4a. **(b)-(d)** Rupture speed vs. the location of the rupture tip for the cases of $P = 11 MPa$, $12 MPa$, 48

Figure 2.8: Supershear transition by the Burridge-Andrews mechanism. **(a) and (b)** Snapshots of sliding velocity and normalized shear stress right after supershear

transition and at a later time for the simulation of Fig. 2.7b. The shear stress peak traveling with the shear wave speed in front of the main rupture has reached the nondimensional static friction strength of 0.6 and a daughter crack is initiated (panel a). The daughter crack has supershear speeds and overtakes the shear wave front (panel b). **(c)** Locations of the shear wave front and rupture tip when supershear transition occurs, for the case of Fig.2.7a. We see that, for all P , the location of supershear transition and the shear stress 51

Figure 2.9: Comparison of supershear transition distances L in simulations with pressure-independent $D_c = 1 \mu\text{m}$ (solid red curves) and pressure-dependent $D_c \propto P^{-1/2}$ with $D_c = 1 \mu\text{m}$ for $P = 9 \text{ MPa}$ (dashed blue curves). **(a)** Results for parameters of Fig.2.7a, $f_d = 0.34$, $\Delta\sigma = 3 \text{ MPa}$, $a = 0.8 \text{ mm}$, and $T_o = 5 \mu\text{s}$. Pressure-independent D_c fits the experimental measurements well in this case, while pressure-dependent D_c does not. **(b)** Results for slightly modified parameters $f_d = 0.345$, $\Delta\sigma = 3 \text{ MPa}$, $a = 0.55 \text{ mm}$, and $T_o = 5 \mu\text{s}$. In this case, pressure-dependent D_c results in a good match..... 53

Figure 2.10: Dependence of transition distances on the parameters of the initiation procedure for the case of $f_d = 0.34$ and pressure-independent $D_c = 1 \mu\text{m}$. The reference set of parameters is that of Fig. 2.7a, $a = 0.8 \text{ mm}$, $\Delta\sigma = 3 \text{ MPa}$, $T_o = 5 \mu\text{s}$. In each panel, one of these parameters is varied and the results are shown for simulations with different values of: (a) the half size a of the rupture initiation procedure, (b) normal stress reduction $\Delta\sigma$, and (c) duration T_o . In panel (a), the

snapshots of sliding velocity and shear stress for two values of P show that, for $a = 0.9$ mm, supershear transition occurs by the Burridge- 55

Figure 2.11: Slip velocity histories at the location of 40 mm along the interface for **(a)** an experimental measurement of Lu *et al.* (2007), **(b)** a simulation with the direct supershear transition at the rupture tip, and **(c)** a simulation with the Burridge- Andrews transition mechanism. In all cases, the supershear transition has already occurred, since the rupture tip arrives at this location faster than the shear wave front indicated by the dashed vertical line. Overall, the shape of the slip-velocity profile is similar for all three cases..... 61

Figure 3.1: (a) Schematic illustration of the experimental configuration. Homalite samples are cut with an inclination angle α and compressed with the far-field load P . Dynamic photoelasticity and laser velocimetry are used to capture the full field information of rupture propagation as well as local sliding velocity of the interface. Rupture nucleation is achieved by a local pressure release due to an explosion of a thin wire. (b) A photograph of the experimental setup..... 69

Figure 3.2: Surface preparation of specimens. (a) SEM (Scanning Electron Microscopy) image of the specimen surface after cutting, showing periodic scratches. (b) SEM image..... 72

Figure 3.3: Illustration of the experimental diagnostics for an experiment with the inclination angle $\alpha = 30^0$ and compressive load $P = 14$ MPa. (a) and (c) Fault-parallel velocity histories measured 20 mm and 40 mm from the rupture nucleation site, respectively. The velocities of the upper and lower measurement points are

shifted by 3 m/s. P-wave and shear wave arrivals are indicated by dashed lines. The estimated rupture initiation time is marked by a green dot. Once initiated, the sliding continues throughout the observation window, corresponding to the crack-like rupture mode. The rupture is supershear, since rupture initiation occurs earlier than the shear wave arrival time. (b) and (d) Dynamic photoelastic images captured 16 μ s and 40 μ s after the rupture nucleation, re 77

Figure 3.4: Comparison of fault-parallel velocity measurements between (a) a regular sample and (b) a twice thinner sample. For both cases, the inclination angle is $\alpha = 20^\circ$, the compressive load is $P = 10$ MPa, and the measurement location is 20 mm. The wavelengths of oscillations in the slip velocity profile becomes twice smaller for the twice thinner samples, indicating that the oscillations are at least partially due to the 3D effect. 81

Figure 3.5: Evaluation of deviations from anti-symmetry of the fault-parallel velocity on the two sides of the interface measured at (a) 20 mm and (b) 40 mm from the nucleation region. For both measurements, $\alpha = 30^\circ$ and $P = 10$ MPa. Dashed lines are smoothed velocity profiles that are constructed by averaging the measurement within the window of 5 μ s, in an attempt to approximately remove the 3D effect. Deviations from asymmetry in the upper and lower measurements are present at 20 mm but virtually disappear at 40 mm. Smoothing the velocity profiles decreases the asymmetry, indicating that it is partially due to the 3D effect. 83

Figure 3.6: Variation of rupture mode with the inclination angle α and hence with the nondimensional shear prestress, illustrated using $\alpha = 20^\circ$ (left column), $\alpha = 25^\circ$ (middle column), and $\alpha = 30^\circ$ (right column) for two values of the compressive

load, $P = 14$ MPa (top row) and $P = 10$ MPa (middle row). Panels in the bottom row show the relative displacement profiles for two compressive loads. As α increases from 20° , to 25° , and then to 30° , the rupture mode varies from a narrower pulse-like, to a wider pulse-..... 86

Figure 3.7: Variation of rupture mode with the compressive load P for $\alpha = 25^\circ$ (top row) and $\alpha = 27.5^\circ$ (bottom row). Velocity histories are measured at the distance of 40 mm 88

Figure 3.8: Collective analysis of rupture duration for different inclination angles and compressive loads measured at the distance of (a) 20 mm and (b) 40 mm. Rupture duration is normalized by the total possible sliding time at the location, which is equal to the time window of observation minus the rupture arrival time. The normalized duration of 1 corresponds to crack-like ruptures and smaller values correspond to progressively narrower pulse-like ruptures..... 90

Figure 3.9: Illustration of the definition of theoretical parameters τ_{pulse} and T used to predict rupture mode in our analysis, based on the study of Zheng and Rice (1998), for two sets of velocity-weakening parameters: (a) $f_w = 0.2$, $V_w = 1.4$ m/s and (b) $f_w = 0.34$ and $V_w = 0.5$ m/s. The dependence of the steady-state friction coefficient on sliding velocity is shown as a dotted blue line. The (straight) lines of the normalized elastodynamic stress $f_{el}(V) = \tau_{el}(V) / \sigma$ are also plotted, for three different inclination angles. $\alpha = 20^\circ$ corresponds to the shear prestress level lower than τ_{pulse} and parameter T is not defined in that case. Higher angles of 25° and

30° result in the lines of elastodynamic stress intersecting the lines of steady-state friction, with the corresponding values of parameter T given in the Figure..... 94

Figure 3.10: Schematic illustration of the experimental setup for fault-normal velocity measurements. Two measurement locations are separated by $500\ \mu\text{m}$. Note that the exploding wire is $100\ \mu\text{m}$ in diameter and the distance between the wire and the measurements location is $20\ \text{mm}$. Any wave radiated from the nucleation site will continuously decay as it propagates..... 99

Figure 3.11: Fault-normal measurements at the distance of $20\ \text{mm}$ for the experiments with $\alpha = 20^{\circ}$ (left column) and $\alpha = 30^{\circ}$ (right column). The compressive load is $P = 10\ \text{MPa}$ for both cases. (a)-(b) Fault parallel velocity measurements above and below..... 102

Figure 3.12: Comparison of fault-parallel velocity histories obtained with different explosion intensity, for $\alpha = 25^{\circ}$ and $P = 10\ \text{MPa}$. (a) The capacitor bank used for the wire explosion is charged with the regular voltage of $1600\ \text{V}$. (b) The charging voltage is reduced to 75% of the regular value. The peak slip velocity in (b) is slightly reduced but the rupture duration is similar. 104

Figure 3.13: Representative cases of supershear pulse-like and crack-like ruptures. Fault-parallel relative velocity histories shown are measured at $40\ \text{mm}$ in experiments with $P = 14\ \text{MPa}$. (a) $\alpha = 27.5^{\circ}$ results in a supershear pulse-like rupture. (b) Superposition of the photoelastic image captured at $44\ \mu\text{s}$ and the velocity measurement from panel (a) The rupture front is clearly ahead of the circular shear wave front, a part of which is marked with a curved yellow line. (c) $\alpha = 28^{\circ}$ results in a crack-like rupture that has almost arrested at the end of the observation window.

(d) $\alpha = 30^\circ$ produces a spuershear rupture that is clearly crack-like. The inset shows a part of the corresponding photoelastic image with the resulting Mach lines.

..... 106

Figure 3.14: Evolution of rupture speed for a pulse-like rupture (diamonds) and a crack-like rupture (circular dots). Both ruptures have supershear speeds within the open interval between $\sqrt{2}c_s$ to c_p . The pulse-like rupture has lower supershear speeds than those of the crack-like rupture. Both observations are consistent with theories based on velocity-weakening interfaces. 111

Figure 3.15: Map of pulse-like (diamonds) vs. crack-like (circular dots) modes and sub-Rayleigh (open symbols) vs. supershear (filled symbols) rupture propagation observed in our experiments. The boundary between pulse-like and crack-like modes (orange dashed line) is drawn based on the experimental results to qualitatively separate the two regimes. The boundary between ruptures that do and do not have supershear propagation (black dashed line) is drawn based on the theoretical analysis as discussed in the text. 117

Figure 4.1: Numerical simulations with linear slip-weakening friction with the parameters $f_s = 0.6$, $f_d = 0.2$, and $D_c = 13 \mu\text{m}$. Only supershear ruptures or no ruptures occurs for the experimental parameters studied. There are no pulse-like ruptures. Two representative cases separated by 0.5 degree in the inclination angle and marked by the small rectangles are illustrated in Fig. 4.2. 120

Figure 4.2: Snapshots of sliding velocity and accumulated slip distributions for two representative simulations with a 0.5 degree difference in the inclination angle. The left col 124

Figure 4.3: Simulations with linear slip-weakening friction with parameters $f_s = 0.6$, $f_d = 0.34$, and $D_c = 1 \mu\text{m}$. In this case, the same conclusion could be drawn that no pulse-like rupture is likely to exist. (a) and (b) are two representative cases with half degree difference in the inclination angle..... 124

Figure 4.4: Experimental setup of the double shearing tests to measure rate-and-state friction properties. (a) Schematic drawing of the configuration. Two pairs of Homalite plates are confined by the side blocks to form double frictional mating interface. Sliding is enforced by the movement of central block upside down. (b) Real Homalite specimens during the test. The short plate has the size of $50 \text{ mm} \times 50 \text{ mm}$, while the longer plate is $80 \text{ mm} \times 50 \text{ mm}$ (work in progress in collaboration with Brian Kilgore and Nick Beeler, USGS)..... 129

Figure 4.5: Schematic illustration of rate-and-state friction response to velocity stepping tests. The normalized friction is plotted against slip. When a positive velocity change occurs, direct effect will drive friction to a higher level instantaneously. Then depending on whether the friction is velocity-weakening or velocity-strengthening, friction gradually evolves into a steady state level for the new slip rate. Opposite change occurs when we impose a negative velocity change. It is notable that for the Dieterich-Ruina rate-and-state friction implemented in our model, the evolution profiles of velocity increase and decrease are not symmetric. 131

Figure 4.6: Laboratory measured rate-and-state friction of Homalite through velocity stepping tests. Velocity jumps are between $0.1 \mu\text{m/s}$ and $0.01 \mu\text{m/s}$. Three cycles of tests are conducted for both jump-up and jump-down cases. The spikes in friction which correspond to peaks of direct effect are labeled with letters A-F, in which parameter a can be inferred. In addition, two steady-state sliding levels are marked with dash lines to obtain parameter $(a-b)$. The characteristic slip L is determined when evolution of friction has completed 82.6% of the entire change for the jump-down test in this measurement (work in progress in collaboration with Brian Kilgore and Nick Beeler, USGS). 132

Figure 4.7: Rupture mode simulations with rate-and-state friction enhanced with flash heating. Friction parameters are chosen as: $f_* = 0.58$, $f_w = 0.2$, $L = 0.3 \mu\text{m}$, $a = 0.011$, $b = 0.016$, $(a-b) = -0.005$, $V_* = 1 \times 10^{-6} \text{ m/s}$, $V_w = 0.2 \text{ m/s}$, initial $\theta = 60 \text{ s}$. Same nucleation procedure as in slip-weakening calculations has been applied with the half nucleation size 6 mm and maximum normal stress reduction 7 MPa . Different rupture modes are marked by different symbols. The transition from pulse-like to crack-like with increasing the inclination angle is broadly consistent with our experimental results. 139

Figure 4.8: Three representative simulations with inclination angles of 25, 27, and 30 degrees and compressive load of 10 MPa . Left column is the sliding velocity distribution at $15 \mu\text{s}$. The right column illustrates local sliding velocity and friction at 10 mm away from the center of the interface. 141

Figure 4.9: (a) Comparison of effective slip dependence of rate-and-state friction and linear slip-weakening friction. The local sliding history is at the location 10mm is

$a = 0.005$, $b = 0.01$ shown (b) Friction evolution during the rupture propagation process. For crack-like rupture, friction eventually resides on the steady-state friction curve..... 143

Figure 4.10: (a) Rupture mode simulations with flash-heating parameters $f_w = 0.1$ and $a = 0.005$, $b = 0.01$ and $V_w = 0.1$ m/s. Compared with Fig. 4.7, more crack-like ruptures are present. (b) Effective slip dependence of friction. The residual friction is reduced to 0.1 and hence seismic ratio is smaller. Ruptures are more likely to transition to supershear speeds..... 147

Figure 4.11: (a) Rupture mode simulations with rate-and-state friction parameters, $(a - b) = -0.005$. Note that the direct effect is reduced but velocity weakening is maintained. According to the steady-state analysis of Zheng and Rice (1998), we would not anticipate a change in rupture modes. However, because of the lower effective static friction and fracture energy, this change promotes crack-like rup. 149

Figure 4.12: Growing pulse-like rupture at 25 degrees inclination angle and 14 MPa compressive load. The friction parameters are . (a) Snapshots of velocity distribution every 5 μ s. (b) Snapshots of accumulated slip every 5 μ s. 151

Figure 4.13: Rupture mode variation with different selection of characteristic slip L of the rate-and-state friction. Snapshots of sliding velocity at 15 μ s are shown. Experimental conditions are the inclination angle of 20 degrees and compressive load of 10 MPa. (a) $L = 0.3$ μ m. (b) $L = 0.2$ μ m. (c) $L = 0.1$ μ m. (d) $L = 0.05$ μ m. 153

Figure 5.1: Experimental configuration for high-speed friction measurements. Two flat Homalite plates are compressed with P . At a chosen location, reflective membranes

and a strain gage rosette are put near each other to measure the local sliding velocity as well as the stress components. A Steel-Homalite composite projectile is launched with a gas gun at a high speed of the order of 1~10 m/s. Interfacial sliding is induced by the impact shearing effect. A steel bar is attached to the side of the Homalite plate to avoid shattering. 158

Figure 5.2: Finite element simulation of the horizontal velocity field by ABAQUS.

Compressive load $P = 2$ MPa and initial impact speed $V = 10$ m/s are used. The interface is modeled using linear slip-weakening friction with $f_s = 0.6$, $f_d = 0.2$, $D_c = 13$ μm . The transmission waves from Steel-Homalite boundary in the projectile have higher speed. This would induce a velocity jump as evident by comparing the velocity field at 15 μs and 45 μs 160

Figure 5.3: FEM-simulated sliding velocity at the location of 50 mm from the impact.

There are two levels of sustained high velocity and a velocity jump from about 1.5 m/s to 3.5 m/s due to the transmission waves from the material boundary of Steel and Homalite in the projectile. This velocity profile can be used to study high-speed friction at two different levels and the frictional response to the velocity jump, similar to rate-and-state velocity stepping test but operating at a slip rate relevant to our dynamic rupture experiment. 161

Figure 5.4: Proposed quantification of the explosion. An array of velocimetry

measurement locations is positioned around the explosion site. The effect nucleation region is modeled as a distributed zone. Through numerical inversion, we plan to quantify the details of nucleation mechanism, such as strength and duration. 163

Figure 5.5: Preliminary velocimetry measurements for explosion quantification. Two laser beams are positioned along horizontal and vertical as shown. For a horizontal interface, there is no sliding, hence the measurement is entirely the response to the explosion. Two independent experiments are conducted to prove the good repeatability of the measurements. The fact that the vertical measurement has higher initial peak indicates that the wave front of the explosion is not perfectly axisymmetric.....	164
Figure 5.6: Stress inhomogeneities due to inclusions in the bulk of the material (a) Strong and weak patches model. (b) Array of holes model.....	167
Figure 5.7: Inhomogeneous far-field loading: (a) High central stress (b) Step loading .	168
Figure 5.8: Interface strength inhomogeneity models: (a) Random dots (b) Periodic strips	169
Figure 5.9: Complex Fault Geometries with steps and offsets (a) Zigzag fault system. (b) Multiple faults system.....	171

Table 2. 1: Experimentally measured supershear transition distances L for different P .. 31

Table 3.1: Values of the mode-predicting parameter T for the ranges of inclination angles and compressive loads explored in our experiments, computed using (a) $f_w = 0.2$, $V_w = 1.4$ m/s and (b) $f_w = 0.34$ and $V_w = 0.5$ m/s. Other friction parameters are specified in the text. Values of T close to 0 predict crack-like modes, while values close to 1 predict pulse-like modes. Empty cells correspond to experimental conditions for which parameter T is not defined, predicting either a pulse-like rupture or no rupture. The region $T < 0.3$ is shown in orange, to qualitatively indicate the experimental parameter space that is predicted to correspond to crack-like ruptures. The critical value of 0.3 is chosen based on simulations of Zheng and Rice (1998)..... 97

Table 4.1:Rate-and-state friction parameters..... 136

Table 4.2: Fracture energy for different friction laws (per unit area)..... 145

Table 4.3: Table of T generated based on the theory of Zheng and Rice (1998). Two sets of friction parameters are used: (a) $f_w = 0.2$, $V_w = 0.2$ m/s (b) $f_w = 0.1$, $V_w = 0.1$ m/s..... 145

Chapter 1

Introduction

Destructive large earthquakes occur as dynamic frictional ruptures along pre-existing interfaces (or faults) in the Earth's crust. Inversions of seismic and other field observations have significantly advanced our understanding of earthquake ruptures. At the same time, detailed inversions are often impossible due to limited data availability or due to limited knowledge of the structure and properties of the crust.

This reality highlights the need for combined experimental and theoretical studies that both record dynamic rupture phenomena in highly-instrumented experiments and analyze the experimental findings through numerical models to understand implications for fault friction and rupture dynamics. To illuminate relevant dynamic processes, the laboratory experiments should reproduce enough of the basic physics governing rupture dynamics of crustal earthquakes. However, the experiments should preserve enough simplicity so that clear conclusions can be obtained either by direct observation or through numerically

tractable models. One example of such experiments is the work of Xia et al. (2004) which has demonstrated for the first time the ability of spontaneous dynamic ruptures to transition from sub-Rayleigh to supershear speeds.

This thesis presents such a combined experimental and theoretical study aimed at understanding the conditions for selecting pulse-like vs. crack-like rupture modes and subshear vs. supershear rupture speeds. In Chapter 2, a numerical model of the experiments by Xia et al. (2004) is developed to understand the effect of the experimental rupture initiation procedure on supershear rupture transition. The model is based on linear slip-weakening friction to enable comparisons with prior studies. In Chapter 3, we adopt and further develop the experimental setup of Xia et al. (2004), and then use it to study pulse-like and crack-like rupture modes. We show that our experimental results are consistent with theories of ruptures on interfaces governed by velocity-weakening friction. In Chapter 4, the numerical model of Chapter 2 is used with both slip-weakening and velocity-weakening friction formulations in an effort to reproduce the experimentally observed pulse-like and crack-like rupture modes presented in Chapter 3. We find that linear slip-weakening friction cannot produce pulse-like modes, even in the presence of the dynamic nucleation procedure used in experiments, while velocity-weakening friction can indeed reproduce both pulse-like and crack-like modes, as expected from our analysis in Chapter 3. At the same time, the particular form of velocity-weakening friction considered in Chapter 4 has difficulty in reproducing the full range of experimental observations. The discussion in Chapter 5 contains several ideas on how to improve the experimental setup,

the interpretation of the experimental results, and the corresponding numerical models and friction formulations.

Rupture transition from sub-Rayleigh to supershear speeds (also called “supershear transition”) has been the subject of many theoretical and numerical investigations dating back to the early 70’s (Burridge 1973; Andrews 1976; Das and Aki 1977; Burridge *et al.* 1979; Freund 1979; Day 1982; Broberg 1989; Needleman and Rosakis 1999; Abraham and Gao, 2000; Madariaga and Olsen 2000; Gao *et al.* 2001; Geubelle and Kubair 2001; Dunham and Archuleta 2005; Festa and Vilotte 2006; Rosakis *et al.* 2007 and references therein; Liu and Lapusta 2008; Shi *et al.* 2008). The occurrence of this phenomenon has been inferred from seismic observations of large earthquakes (Archuleta 1984; Olsen *et al.* 1997; Bouchon *et al.* 2001; Bouchon and Vallee 2003; Dunham and Archuleta 2004; Ellsworth *et al.* 2004; Robinson *et al.* 2006; Das, 2007), and the possibility of such transition has been confirmed in the laboratory (Rosakis *et al.* 1999; Rosakis 2002; Xia *et al.* 2004; Lu *et al.* 2007; Rosakis *et al.* 2007). In particular, Xia *et al.* (2004) reported the first direct observations of supershear transition in rupture experiments designed to mimic crustal earthquakes. Studies of supershear transition have important practical implications. Supershear ruptures can cause much stronger shaking far from the fault than subsonic ruptures (Aagaard and Heaton, 2004; Bernard and Baumont 2005; Dunham and Archuleta 2005; Bhat *et al.* 2007), as Mach fronts generated by intersonic ruptures carry large stresses and particle velocities far from the fault. In addition, understanding which fault properties and conditions do and do not favor supershear transition allows to constraint properties and conditions on real faults.

Motivated by the experiments of Xia *et al.* (2004), in Chapter 2 we consider the effect of rupture nucleation conditions and friction parameters on supershear transition of Mode II ruptures on interfaces governed by linear slip-weakening friction. In Xia *et al.* (2004) the experiments were analyzed using the Burridge-Andrews (Burridge 1973, Andrews 1976) model of supershear transition, in which a supershear daughter crack is nucleated in front of the main mother rupture. In particular, the experimentally determined transition distances were compared with the ones from the Burridge-Andrews model and by a subsequent analysis which was based on micromechanical considerations. It was concluded that the critical slip of the linear slip-weakening formulation needs to be pressure-dependent for a good match with experiments. However, the rupture initiation mechanism in the experiments was conceptually different from the one adopted in the numerical work used for comparison.

We numerically model the experiments of supershear transition with a rupture initiation procedure intended to closely capture the dynamic nature of the wire explosion mechanism used in the experiments to induce rupture initiation. A spectral boundary-integral method (BIM) is adopted because of its efficiency and accuracy in solving dynamic sliding problem in homogeneous interface. Our goal is to find parameter regimes that would match the experimentally observed transition distances for the entire range of experimental conditions. Two regimes of friction parameters are considered, with different seismic ratios that result in significantly different nondimensional transition distances of earlier studies. Our simulations show that, for the two regimes under consideration, the dynamic

rupture initiation procedure significantly affects the resulting transition distances, shortening them by about 30%-50% compared to those predicted through the smooth rupture initiation process. Moreover, for some cases, the dynamic initiation procedure changes the very mode of transition, causing a direct supershear transition at the tip of the main rupture instead of the mother-daughter mechanism. We find reasonable parameter regimes which match experimentally determined transition distances with both direct supershear transition at the rupture tip and the Burridge-Andrews (mother-daughter) mechanism, using both pressure-independent and pressure-dependent critical slip. The results show that there are trade-offs between the parameters of the rupture initiation procedure and the properties of interface friction. This underscores the importance of quantifying experimental parameters for proper interpretation of the experiments and highlights the importance of the rupture initiation procedure, in simulations of both experiments and real-life earthquake events.

Our simulations in Chapter 2 use linear slip-weakening friction to enable comparison with earlier studies. This friction law is widely used in simulations of frictional ruptures. However, accumulating experimental, observational, and theoretical findings discussed in the following paragraphs suggest that friction is intrinsically velocity-dependent. In fact, most friction laws formulated based on laboratory experiments and theories of frictional resistance combine velocity dependence of friction with transient and slip-dependent effects (Dieterich, 1979, 1981; Ruina, 1981). At the same time, the simplified friction model of linear slip-weakening friction is convenient, easy to implement, produces results that can be compared to classical theoretical developments, and captures one of the

essential features of frictional resistance that leads to dynamic rupture, namely the decrease of friction during sliding. It is important to understand whether the linear slip-weakening formulations of friction are adequate to describe all basic rupture phenomena, or whether inclusion of velocity-dependent features is necessary.

One research topic that can help us determine whether velocity dependence of friction is important to include in rupture modeling, or whether linear slip-weakening description is adequate, is the issue of pulse-like vs. crack-like rupture modes. Numerical simulations in models that involve homogeneous elastic and interface properties and velocity-independent fault strength result in the crack-like mode of earthquake propagation, in which the duration of slip at each point on the fault is comparable to the overall rupture duration (Andrews 1976; Kostrov 1966; Ida 1972; Madariaga 1976; Harris and Day 1993). However, seismic inversions indicate (Heaton 1990) that ruptures on real faults may propagate in the pulse-like mode, in which slip duration at a point is much shorter than the overall rupture duration. Theoretical and numerical studies have shown that the issue of rupture modes may have important implications for fault constitutive laws, stress conditions on faults, energy partition and heat generation during earthquakes, scaling laws, and spatio-temporal complexity of slip (Beele and Tullis 1996; Ben-Zion 2001; Shi et al 2008; Heaton 1990; Cochard and Madariaga 1994; Perrin et al. 1995; Cochard and Madariaga 1996; Zheng and Rice 1998; Nielsen et al 2000; Nielsen and Madariaga 2003). Pulse-like ruptures have been obtained in a number of numerical simulations that include significant weakening of interface friction with sliding velocity (Beele and Tullis 1996; Shi et al 2008; Cochard and Madariaga 1994; Perrin et al. 1995; Cochard and Ma-

dariaga 1996; Zheng and Rice 1998; Nielsen et al 2000; Lapusta and Rice 2004). This implies that fault friction may be characterized by significant velocity weakening, a conclusion further supported by a number of recent rock experiments and theoretical studies that have uncovered strongly velocity-weakening friction at seismic slip velocities (Tsunami and Shimamoto 1997; Tullis and Goldsby 2003; Di Toro et al 2004; Rice 2006). Other explanations for the occurrence of pulse-like ruptures include interaction of rupture with fault geometry or local heterogeneities (Day 1982; Johnson 1992; Beroza and Mikumo 1996; Olsen et al 1997; Day et al 1998), and normal stress variation due to difference in material properties across the interface (bimaterial effect) (Andrews and Ben-Zion 1997; Cochard and Rice 2000; Ben-Zion 2001). Which mechanism dominates in real earthquakes remains an open research question.

In Chapter 3 we adopt and further develop the experimental setup of Xia et al (2004) to investigate conditions leading to the selection of pulse-like vs. crack-like rupture modes in a setting which mimics crustal earthquakes. The geometry, loading, and nucleation mechanism are essentially two-dimensional (2D). This configuration is relevant for understanding the dynamics of large strike-slip earthquakes which are dominated by in-plane sliding and constitutes an experimental equivalent of 2D in-plane or Mode II numerical models of dynamic rupture which are common in earthquake studies (Andrews 1976; Das and Aki 1977; Beeler and Tullis 1996; Andrews and Ben-Zion 1997, Cochard and Rice 2000; Ben-Zion 2001; Festa and Vilotte 2006; Shi and Ben-Zion 2006; Liu and Lapusta 2007; Shi et al 2008).

In our experiments presented in Chapter 3, there are no heterogeneities in interface properties or prestress and no bimaterial effect. Our goal is to determine whether pulse-like ruptures can occur in such a homogeneous configuration and if so, what controls the selection of rupture modes. The only prior experimental study of different rupture modes under similarly homogeneous conditions was done with strong impact loading and interfaces with no shear prestress (Lykotrafitis et al. 2006). However, those loading conditions are quite different from the ones on tectonically loaded faults in the Earth's crust. In the present study, we use an experimental configuration with an interface prestressed both in compression and in shear (Xia et al. 2004), simulating a tectonically loaded fault, and combine it with experimental diagnostics that lets us conclusively determine the mode and speed of rupture propagation (Lu et al. 2007; Lykotrafitis et al. 2006; Rosakis 2002).

By systematically varying fault prestress, we observe pulse-like and crack-like ruptures, and systematic transition between them, as described in Chapter 3. Our results are consistent with the theoretical study of Zheng and Rice (1998) who considered velocity-weakening interfaces and showed that selection of rupture modes depends on fault prestress and velocity-weakening properties of faults. We also present the first experimental observations of pulse-like ruptures transitioning to supershear speeds. A number of experiments are conducted to investigate the influence of the rupture nucleation procedure and sample geometry. Results show that the strength of the nucleation affects the peak sliding velocity, but not the rupture mode. More importantly, our results indicate that there is no fault-normal stress reduction at the measurement location. Hence the variation

in rupture modes and rupture speeds that we observe cannot be caused by the nucleation-induced normal stress decrease, and velocity-weakening friction remains the most viable explanation.

To study the effect of experimental setup on observed rupture modes reported in Chapter 3, in Chapter 4 we conduct numerical modeling of the experiments using the model of Chapter 2. Given the absence of bi-material effect and local heterogeneities, the experimental results indicate the importance of velocity-weakening friction for producing pulse-like ruptures. In fact, the comparison between experiments and theoretical analysis of velocity-weakening interfaces by Zheng and Rice (1998) results in a qualitative agreement. However, the analysis by Zheng and Rice (1998) does not consider the effect of the rupture nucleation mechanism. In Chapter 2, we model the wire explosion as a dynamic normal stress reduction to analyze the rupture transition to supershear speeds. The results show that such initiation procedure significantly affects the resulting transition distances and even changes the mechanism of supershear transition. The study of Chapter 2 raises two questions. First, is it possible to produce pulse-like ruptures and match experimentally observed variation of rupture modes with linear slip-weakening friction, due to a short duration of the wire explosion which may favor the pulse-like rupture? Second, are the general conclusions of rupture mode selection based on velocity-weakening friction and fault prestress still valid in the light of the rupture initiation mechanism?

In Chapter 4, we first adopt linear slip-weakening friction, with parameter choices that have enabled us to match supershear transition experiments in Chapter 2, and numerically simulate a series of experiments that lead to crack-like and pulse-like rupture modes. Our simulations show that the rupture either propagates in a crack-like mode, or dies out right after the end of the nucleation procedure, which is clearly inconsistent with the experiments. This demonstrates that linear slip-weakening friction is not sufficient to promote pulse-like sliding, even with the dynamic rupture initiation mechanism

We then use the rate-and-state friction enhanced with flash heating as motivated by laboratory experiments. Standard rate-and-state friction parameters are quantified through the velocity stepping tests at low slip velocity (collaboration with B. Kilgore, N. Beeler, and C. Marone). For the regime of high slip velocity, we incorporate strong velocity weakening motivated by flash heating. The results exhibit qualitative agreement with experiments: rupture mode varies from pulse-like to crack-like with increase of prestress level. However, precise match is difficult to obtain due to many uncertainties in friction parameters and in the modeling of rupture nucleation.

Although the simulation results endorse the general conclusion of experimentally observed rupture mode variation, we notice that, with the same friction parameter choice, the theoretical prediction based on the theory of Zheng and Rice (1998) differs substantially from our simulations. This discrepancy leads to two implications. First, the rupture nucleation mechanism could vary the rupture mode selection in a systematic way. In our model, the short duration of the nucleation procedure associated with the healing phase at

the end of the nucleation may act to favor pulse-like rupture. Hence compared to the predicted map of rupture mode, the simulation results shift to the pulse-like side significantly. Second, several rate-and-state friction parameters do not enter the theory of Zheng and Rice (1998), for instance, the characteristic slip L , individual values of a and b . However, simulations show that these parameters can also alter the rupture mode distribution, sometimes in a significant way. After all, the length scale of problem is associated with L , and direct effect and healing effect of the rate-and-state friction are determined by the individual values of a and b . These elements coupled with nucleation mechanism will affect the rupture dynamics and hence cannot be ignored in the analysis of rupture mode.

In Chapter 5, we outline the plan to extend our current efforts of combined experimental and theoretical study. In order to set up a good benchmark problem, we outline ways to quantify a number of parameters. One important aspect is the high-speed friction properties of the experimental interfaced; and consequently a localized friction-velocity measurement plan is proposed. In addition, we discuss quantification of rupture nucleation procedure as this thesis has proven it to be important. Finally, several potential rupture experiments are proposed to investigate the effect of heterogeneities, either in terms of a global stress field or local interface strength.

Overall, this thesis is focused on several theoretically and numerically important problems in rupture dynamics, such as pulse-like to crack-like rupture mode variation, and sub-Rayleigh to supershear rupture speed transition. Our approach to attack these prob-

lems is to integrate experimental observations and numerical simulations, and to compare the results obtained from different methodologies. That way, we try to benefit from the simplicity of experimental design, the state-of-art high-resolution experimental diagnostics, and the convincing power of direct experimental observations. On the other hand, we are aided by the rigorousness of theoretical analysis, its capacity to reveal every details of the simulation results, and the flexibility to adopt different theories into the numerical model. The combination of these two methods provides a powerful methodology for understanding different rupture phenomena and motivates new research ideas.

Chapter 2

Numerical Analysis of Supershear Transition Regimes in Rupture Experiments: the Effect of Nucleation Conditions and Friction Parameters

In this Chapter, we investigate the effect of rupture nucleation conditions and friction parameters on supershear transition of Mode II ruptures on interfaces governed by linear slip-weakening friction.

The Chapter is based on a manuscript by Lu, Lapusta, and Rosakis (2008, submitted to GJI).

2.1 Introduction

This study is motivated by the experiments described in Xia *et al.* (2004) and Rosakis *et al.* (2007). In these experiments, the Earth's crust was simulated by a square (150 mm x

150 mm) photoelastic plate cut to introduce a frictional interface inclined at the angle $\alpha = 25^\circ$ to the horizontal (Fig. 2.1). Uniform pressure P was applied at the top and bottom ends of the plate, inducing shear traction $\tau_0 = P \sin \alpha \cos \alpha$ and normal traction $\sigma_0 = P \cos^2 \alpha$ on the interface. The ratio of shear to normal tractions, $f_0 = \tau_0 / \sigma_0 = \tan \alpha = 0.47$, was smaller than the static friction coefficient $f_s = 0.6$ of the interface, and hence the interface simulated a tectonically loaded fault locked due to friction. A series of experiments was done, with P varying from 8.8 to 15 MPa. Initiation of spontaneous dynamic rupture was achieved by means of an exploding wire acting in the middle of the plate interface across the entire plate thickness. The experiments were done using a photoelastic material, which allowed to capture and analyze rupture progression using high-speed photography. The images revealed a bilateral spontaneous dynamic shear rupture propagating along the interface, initially with sub-Rayleigh speeds and then transitioning to supershear speeds. The details of the experimental set up, exploding wire mechanism, and optical diagnostics are described in Rosakis *et al.* (2007).

Xia *et al.* (2004) reported the transition distance for each experiment, i.e., the distance between the middle of the interface and the position of the rupture tip when the rupture transitioned to a supershear speed, and compared these transition distances with the ones in the numerical study by Andrews (1976). The numerical work of Andrews (1976), building upon an earlier analytical study of Burridge (1973), showed that supershear transition can be achieved by nucleating a supershear daughter crack ahead of the main rupture, which immediately propagates at a supershear speed and also spreads backwards to unite with the main rupture. This mechanism is often referred to as the Burridge-Andrews

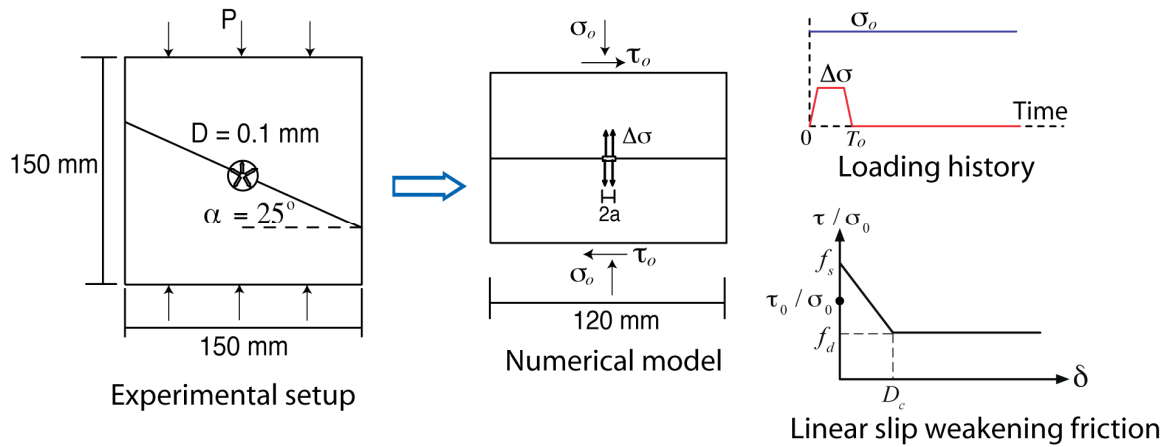


Figure 2.1: Our model for simulations of supershear transition. Motivated by the experimental setup of Xia *et al.*, 2004 (left panel), we consider a planar interface in a thin plate (middle panel). The interface is prestressed both in compression, with $\sigma_0 = P \cos^2 \alpha$, and in shear, with $\tau_0 = P \sin \alpha \cos \alpha$. For $\alpha = 25^\circ$ used in the experiments, $\tau_0 / \sigma_0 = 0.47$. The rupture is initiated by applying a transient reduction $\Delta\sigma$ of normal stress in the region of length $2a$ in the middle of the interface for time T_0 . The time dependence of the normal-stress reduction is shown in the top of the right panel. The interface is governed by linear slip-weakening friction (bottom of the right panel) with the static coefficient $f_s = 0.6$. Several values of the dynamic friction coefficient f_d and critical slip D_c are considered.

mechanism (Rosakis, 2002) or the mother-daughter mechanism (Abraham and Gao, 2000). Andrews (1976) assumed linear slip-weakening friction, in which the shear strength of the interface decreases linearly from static frictional strength level of τ_s to the dynamic frictional strength level of τ_d over the critical slip D_c , and then remains at τ_d during subsequent sliding (Fig.2.1). Using this model, he demonstrated that the transition distance depends only on the critical crack half length L_c and on the seismic ratio s as follows:

$$L = F(s)L_c, \quad L_c = \frac{\mu(\tau_s - \tau_d)D_c}{\pi(1-\nu)(\tau_0 - \tau_d)^2}, \quad s = \frac{\tau_s - \tau_0}{\tau_0 - \tau_d}. \quad (2.1)$$

In eq.(2.1), $F(s)$ is a numerically determined function that can be approximated by $F(s) = 9.8(1.77 - s)^{-3}$ as discussed by Rosakis *et al.* (2007). The parameters μ and ν are the shear modulus and Poisson's ratio of the elastic solid and τ_0 is the initial resolved shear stress acting on the interface. In terms of the geometry of Fig. 1, eq.(2.1) can be expressed as (Rosakis *et al.*, 2007):

$$L = F(s) \frac{\mu(f_s - f_d)D_c}{\pi(1-\nu)(\sin \alpha - f_d \cos \alpha)^2 P} \propto \frac{1}{P}, \quad s = \frac{f_s - \tan \alpha}{\tan \alpha - f_d}, \quad (2.2)$$

where $f_s = \tau_s / \sigma_0$ and $f_d = \tau_d / \sigma_0$ are the static and the dynamic friction coefficients, respectively. Eq.(2.2) predicts that the experimentally observed transition distance L should be proportional to P^{-1} , assuming that critical slip D_c does not depend on the far-field compression level P .

The experimentally determined transition distances of Xia *et al.* (2004) were indeed smaller for larger values of P , in qualitative agreement with the results of Andrews

(1976), however the dependence was stronger than P^{-1} . Xia *et al.* (2004) explained the discrepancy by introducing the dependence of critical slip D_c on compression P as $D_c \propto P^{-1/2}$, based on experiments of Ohnaka (2003) and a micromechanical model described in detail by Rosakis *et al.* (2007). The resulting scaling $L \propto P^{-3/2}$ provided a better match with the experimental measurements, as reviewed in the following sections. While the main contribution of the work by Xia *et al.* (2004) was the demonstration that spontaneous supershear transition is possible, the comparison of the experimental measurements with the theory of Andrews (1976) provided additional insights, pointing to the daughter-crack mechanism as the likely explanation and suggesting that the critical slip D_c is pressure-dependent and that $L \propto P^{-3/2}$.

The mechanisms of rupture initiation in the experiments of Xia *et al.* (2004) and in the numerical simulations of Andrews (1976) are conceptually different. Our goal is to determine how much the comparison between experimental and numerical results is affected when we consider a numerical model with a nucleation procedure which is closer to the experimental one. In the experiments, the initiation of dynamic rupture was achieved by a local explosion of a thin (0.08 mm in diameter) nickel wire. The wire was embedded within a tunnel (cylindrical hole) of 0.1 mm in width located in the middle of the plate interface, and piercing the entire plate thickness. The ends of the wire were connected to a charged capacitor. Following a sudden discharge, the nickel wire was heated by the current surge and turned into high-pressure plasma, relieving the applied compression locally. This allowed shear ruptures to initiate around the explosion site under the action of the resolved shear stress. In contrast, Andrews (1976) used a rupture

initiation procedure intended to model smooth rupture acceleration from its critical size $2L_c$. Hence the initiation procedures had two key differences: The initiation procedure in the experiments was (i) relatively abrupt and (ii) the same in intensity, rise time and spatial extent for all compression loads P , while the initiation procedure in the Andrews' model was (a) smooth and (b) dependent on L_c and hence it varied with the level of the far-field load P . The potential influence of rupture initiation on subsequent rupture propagation and supershear transition was highlighted in some recent studies (Festa and Vilotte 2006; Liu and Lapusta 2008; Shi *et al.* 2008). However, this factor was not considered in the original analysis by Xia *et al.* (2004). Details of rupture initiation may affect transition distances and, in particular, may offer an alternative explanation for the stronger dependence of transition distances on the far-field compression P . Our model, including the initiation mechanism, is described in section 2.2.

In terms of friction properties, one parameter in particular seems to be of determining influence on supershear transition in the context of the work by Xia *et al.* (2004). Indeed, the study of Andrews (1976) showed that transition distances strongly depend on the seismic ratio s . For the experiments of Xia *et al.* (2004), the seismic ratio s is given by (2) with $f_s = 0.6$ and $\alpha = 25^\circ$, resulting in

$$s = 0.13 / (0.47 - f_d). \quad (2.3)$$

Hence transition distances strongly depend on the dynamic friction coefficient f_d which has not been precisely quantified for the Homalite interfaces used in the experiments. Xia *et al.* (2004) used $f_d = 0.2$ in their analysis, based on an additional set of experi-

ments in which they started with a near-horizontal interface ($\alpha = 10^\circ$) and increased the inclination angle until the explosion-induced rupture was able to propagate through the entire sample. Based on the tangent of that critical angle, they estimated that $f_d = 0.2$, which results in $s = 0.5$. This corresponds to $L/L_c = 4.8$ (a result which is based on the equation (2.1) as described by Xia *et al.* (2004) and in more detail by Rosakis *et al.* (2007)). Hence, for $f_d = 0.2$, the transition distance L is only about 5 times larger than the critical crack half-length L_c . Given that the initiation region itself has to be of the order of L_c and that the abrupt initiation procedure shortens the transition distances (as we show in the following sections), the case with $f_d = 0.2$ corresponds to supershear transition being close to the initiation site in comparison with the critical crack size. We study both this case (section 2.3), as well as the case with a different seismic ratio $s = 1.0$ ($f_d = 0.34$), which results, according to eq. (2.1), in transition distances much larger than the critical crack size, $L/L_c = 21.5$ (section 2.4).

The two primary goals of this work are to study supershear transition with an initiation procedure that mimics the experiments and also to consider two different parameter regimes that result in significantly different ratios of transition distances and critical crack sizes. These goals are closely related. One would expect the initiation procedure to have a different effect on the length and mode of supershear transition, depending on how close the location of the transition is to the rupture initiation region. This expectation is supported by our study, as described in sections 2.3 and 2.4. Indeed, even the mechanism of the supershear transition is different in the two parameter regimes, for cases that match

experimentally determined transition distances. Comparisons between the two regimes and conclusions are given in sections 2.5-2.6.

2.2 Model for simulating supershear transition

Our model (Fig.2.1) is based on the configuration used by Xia *et al.* (2004). We consider a planar interface in a thin Homalite plate, in the context of a two-dimensional plane-stress problem. Homalite has the following material properties (Dally and Riley, 1991): Young's modulus $E = 3860$ MPa, shear modulus $\mu = 1429.63$ MPa, Poisson's ratio $\nu = 0.35$, density $\rho = 1200$ kg/m³, and shear wave speed $c_s = 1078.10$ m/s. The interface is prestressed with shear and normal stresses $\tau_0 = P \sin \alpha \cos \alpha$ and $\sigma_0 = P \cos^2 \alpha$ respectively, with the non-dimensional prestress $\tau_0 / \sigma_0 = \tan \alpha$ being independent of P . Following Xia *et al.* (2004), we set $\alpha = 25^\circ$ and use several values of P , ranging from 8 to 16 MPa. As in the study of Andrews (1976), the interface friction is modeled as linear slip-weakening friction with the static friction coefficient f_s , dynamic friction coefficient f_d , and critical slip D_c . The static friction coefficient for the interfaces in the experiments of Xia *et al.* (2004) is well constrained as $f_s = 0.6$, a typical value for many materials including rocks.

The values of the dynamic friction coefficient f_d and critical slip D_c are less certain, and we study two values of f_d and several options for D_c . Xia *et al.* (2004) used $f_d = 0.2$

and, based on the analysis of the experiments using the results of Andrews (1976), determined that $D_c = 10 \mu\text{m}$ for $P = 9 \text{ MPa}$. As described in detail by Rosakis *et al.* (2007) the best fit to experiments was achieved with a pressure-dependent D_c derived based on experiments by Ohnaka (2003) and a micromechanical model:

$$D_c = c[(\tau_s - \tau_d) / \tau_d]^M \sqrt{H} a_0 \cos \alpha \cdot P^{-1/2} \propto P^{-1/2}, \quad (2.4)$$

where c and M are experimentally determined constants, H is the hardness of the material, and a_0 is the average radius of contacting asperities (which is assumed constant). Substituting (2.4) into (2.2), one finds that the transition length L is then proportional to $P^{-3/2}$ as follows:

$$L = F(s) \frac{\mu(f_s - f_d)}{\pi(1-\nu)(\sin \alpha - f_d \cos \alpha)^2} c \left(\frac{f_s - f_d}{f_d} \right)^M \sqrt{H} a_0 \cos \alpha \cdot P^{-3/2} \propto P^{-3/2} \quad (2.5)$$

In the cases where we consider effects of the pressure-dependent D_c , we set the value of $D_c = D_c^{ref}$ for one value of the external compression $P = P^{ref}$, and assign the rest of the values according to $D_c = D_c^{ref} (P / P^{ref})^{-1/2}$.

In section 2.3, we use the set of values proposed by Xia *et al.* (2004). We consider both pressure-independent and pressure-dependent D_c . As mentioned in section 1, transition distances of the Burridge-Andrews mechanism strongly depend on the dynamic friction coefficient. If $f_d = 0.2$, then the seismic ratio $s = 0.5$ and the transition distance $L / L_c = 4.8$. However, the value $f_d = 0.2$ has been determined only approximately, as discussed in section 1, and it may represent a lower bound on the dynamic friction coefficient. In section 2.4, we consider cases with the different seismic ratio of $s = 1.0$, corre-

sponding to $f_d = 0.34$ and resulting in a substantially different normalized transition length $L / L_c = 21.5$. Since the ratio of the transition distance L to the critical crack half size L_c is almost an order of magnitude larger in the second regime, in section 2.4 we use an order of magnitude smaller value of D_c (and hence L_c), so that the predicted unnormalized lengths of the transition distance still matches the experimental measurements with a drastically different set of parameters.

The numerical simulations in this work are performed using a spectral boundary-integral method (Geubelle and Rice 1995; Liu and Lapusta 2008). The elastodynamic response of the surrounding medium is expressed as an integral relationship between the stress and slip on the interface, in the form:

$$\tau(x, t) = \tau_l(x, t) + \varphi(x, t) - \frac{\mu}{2c_s} \dot{\delta}(x, t), \quad (2.6)$$

where $\tau(x, t)$ is the shear stress on the interface, $\tau_l(x, t)$ is the shear stress that would act on the interface in the absence of slip, $\varphi(x, t)$ is the functional of slip history on the interface, and $\dot{\delta}(x, t)$ is the slip (or sliding) velocity. The functional $\varphi(x, t)$ is related to slip history in the Fourier domain. This means that the simulated spatial domain is periodically replicated along the interface. The spatial domain in the simulations is chosen to be large enough to ensure that no waves arrive from replicated rupture processes within the time window of interest. This is consistent with the experimental approach in which supershear transition and propagation were observed for times short enough that no wave reflections could have arrived from the sample boundaries (Rosakis *et al*, 2007). We use the numerical implementation of the boundary-integral method of Liu and Lapusta

(2008). In our model, the interface is discretized uniformly with such a grid that the ratio of the critical crack half length L_c and cell size h is more than 50 for all calculations. In some cases, higher resolution is used to validate the numerical convergence. The cohesive zone size is well-resolved in all simulations.

Our procedure of the rupture initiation (Fig.2.1) is intended to capture the dynamic nature of the wire explosion described in section 2.1. While the wire is less than 0.1 mm thick, it turns into plasma due to the electric current surge, and hence it can affect a larger region along the interface than the 0.1-mm thickness would suggest. After each experiment, the interface surfaces contain a thin layer of metallic particles around the explosion site. The spatial extent of the layer is typically 4-10 mm along the interface. We model the effect of the plasma by applying a reduction $\Delta\sigma$ of normal stress over a region of size $2a$. For simplicity, we keep the normal stress reduction uniform over that region. In most of our simulations, the duration of the normal-stress reduction is $T_o = 5 \mu\text{s}$, consistently with estimates of Rosakis *et al.* (2007). Normal stress is reduced by $\Delta\sigma$ linearly over $1 \mu\text{s}$, kept at the level $(\sigma_0 - \Delta\sigma)$ for $3 \mu\text{s}$, and then brought back to the original level linearly over $1 \mu\text{s}$ (Fig.2.1). We explore the consequences of varying the duration T_o of the normal-stress reduction in sections 2.3.4 and 2.4.4. The normal-stress variation reduces the frictional strength of the interface and allows the sliding to initiate and develop under the applied shear stress. Note that the normal-stress reduction $\Delta\sigma$ used is always smaller than the applied normal stress σ_0 so that there is no interface opening. In the experiments, the wire explosion might cause local opening of the interface; investigating such scenarios is a goal for future research. As discussed in section 2.1, our repre-

sentation of the initiation procedure allows us to explore two aspects that were not a part of the original analysis by Andrews (1976): the dynamic and transient nature of the initiation procedure and the fact that, in the experiments, the initiation procedure is independent of the far-field pressure P .

The goal of this study is to determine the suite of potential transition scenarios relevant to the experimental setup of Xia *et al.* (2004). To that end, for each set of friction properties that we study, we consider a range of the parameters a and $\Delta\sigma$ and choose the ones that give us the best match to experimental observations. This approach not only allows us to determine the range of potential rupture behaviors consistent with the experimental measurements but also outlines the space of plausible initiation parameters, which would be helpful in our future work on quantifying the explosion. Once a set of friction properties has been specified, the choice of rupture initiation parameters becomes relatively restricted by the fact that the same initiation procedure has to initiate spontaneous rupture propagation for all P of interest, from 8 to 16 MPa. The range of P implies a range in the values of the critical crack half size L_c , and it is likely that, for successful rupture initiation, the half size a of the initiation region should be comparable to L_c for all P of interest, with the parameter a/L_c being comparable to 1. Also, the normal stress change $\Delta\sigma$ should be large enough to initiate sliding for all values of P , which means that the condition $(\sigma_0 - \Delta\sigma)f_s < \tau_0$ should be satisfied for all P . This condition is the most restrictive for the largest value of P and, for $\alpha = 25^\circ$ and P from 8 to 16 MPa, translates into the requirement $\Delta\sigma \geq 2.9$ MPa. Since we consider here cases with no opening, we also require that $\Delta\sigma < \sigma_0$ for all P , which results in $\Delta\sigma < 6.6$ MPa.

How do the different initiation parameters affect the rupture nucleation and evolution? Clearly, the larger the parameter a/L_c , the better are the conditions for the initiation of spontaneous rupture. Since larger values of P correspond to smaller values of L_c , a constant value of a would result in the parameter a/L_c being larger for larger P , and hence more favorable for initiation. The effect of the normal stress decrease $\Delta\sigma$ can be measured by the initial slip velocity $\dot{\delta}_{ini}$ that such decrease would cause if it happened instantaneously. That slip velocity can be computed from the elastodynamic relation (2.6). After an abrupt stress drop, we have, in the beginning of sliding, $\varphi=0$, $\tau_l = \tau_0$, $\tau = (\sigma_0 - \Delta\sigma)f_s$, and

$$\dot{\delta}_{ini} = \frac{2c_s}{\mu}(f_s\Delta\sigma + \tau_0 - f_s\sigma_0) = \frac{2c_s}{\mu}(0.6\Delta\sigma - 0.1P). \quad (2.7)$$

Hence the larger $\Delta\sigma$ is, the larger the slip velocity which would be induced. However, the slip velocity also depends on P , with larger values for smaller P . For example, an abrupt drop of $\Delta\sigma = 5$ MPa would induce slip velocity of 3.3 m/s for $P = 8$ MPa and 2.7 m/s for $P = 12$ MPa. Hence a particular value of $\Delta\sigma$ would favor rupture development for smaller values of P . In the initiation procedure in our model, we apply the stress drop over the time of 1 μ s, so the effect would be more complex than estimated here, however the above calculation gives an order-of-magnitude estimate. Finally, the duration of the rupture initiation procedure is important, since, after the normal stress is again increased to the initial value in the region of the nucleation procedure, the slip velocities would be reduced in that region. That should have a different effect on the rupture development, depending on how large the rupture is at that point. The length of the rupture would de-

pend on how the rupture speed evolves. To get an order-of-magnitude estimate, let us assume that the rupture velocity would be close to c_R , so that in time T_o the rupture would advance by about $c_R T_o$. Then $(c_R T_o + a) / a$ would give an estimate of how much larger the rupture is than the region affected by the reduced slip velocities, whereas $c_R T_o / L_c$ would indicate how much beyond the initiation region the rupture has had the chance to propagate before the normal stress reduction effect disappears, with respect to the critical half size L_c .

In this work, we use the critical crack half size L_c as the relevant spatial scale for rupture propagation. Uenishi and Rice (2003) studied the initiation of a frictional shear crack subjected to peaked quasi-static loading and demonstrated that the crack would become dynamic when its half length reaches the critical value

$$L_{nucl} = \frac{0.579 \mu D_c}{(1-\nu)(\tau_s - \tau_d)}. \quad (2.8)$$

Neither parameter L_c nor parameter L_{nucl} are directly relevant to the initiation procedure in this study, since the crack neither starts from its critical quasi-static state nor nucleates under quasi-static peaked loading. We use L_c as the reference length to enable easy comparison with previous studies. Note that the ratio

$$L_{nucl} / L_c = 0.579 \pi \frac{(\tau_0 - \tau_d)^2}{(\tau_s - \tau_d)^2} = 0.579 \pi \frac{1}{(1+s)^2} \quad (2.9)$$

does not depend on the compression P . For $s = 0.5$ and $s = 1.0$, $L_{nucl} / L_c = 0.81$ and $L_{nucl} / L_c = 0.43$, respectively. Hence we see that the two parameters are comparable for the cases we consider in this work.

2.3 Simulations of supershear transition for the seismic ratio $s = 0.5$ ($f_d = 0.2$)

We start by exploring the case of dynamic friction coefficient $f_d = 0.2$ proposed by Xia *et al.* (2004). In this case, the seismic ratio (2.3) becomes $s = 0.5$, and the ratio L/L_c of the transition distance to the critical crack half length is predicted to be 4.8 based on equation (2.1). As we discuss in the following, the ratio of L/L_c becomes even smaller in our simulations, due to the dynamic rupture initiation procedure. Since the supershear transition occurs when the crack length is only 2-3 times larger than the critical crack size, and given that the initiation region itself is of the order of the critical size, we refer to this regime as the one in which the transition occurs close to the initiation region, in nondimensional terms.

2.3.1 Comparison of experimental and simulated transition distances for the parameters of Xia *et al.* (2004)

Fig.2.2(a) shows the experimentally measured transition distances (shown as dots); they vary from about $L = 20$ mm for $P = 9$ MPa to about $L = 10$ mm for $P = 15$ MPa. The exact values are given in Table 2.1. To compare these results with the work of Andrews (1976), Xia *et al.* (2004) and Rosakis *et al.* (2007) matched the observed and theoretical

transition distances for the first experimental data point of Fig.2.2(a) ($P = 8.8$ MPa, $L = 23.4$ mm) inferring $L_c = 5.5$ mm and $D_c = 10$ μm respectively. By assuming the pressure-independent value of $D_c = 10$ μm and pressure-dependent values of D_c given by eq. (2.4), they used eqs. (2.2) and (2.5) respectively to predict the dependence of the transition length on P as shown in Fig. 2.2(a). These curves are indicated as Xia *et al.* (2004) $L \sim P^{-1}$ and $L \sim P^{-3/2}$ respectively. Clearly, the pressure-dependent D_c gives a better match.

The red solid line in Fig.2.2(a) shows the transition distances obtained through the current simulations with pressure-independent $D_c = 10$ μm and rupture initiation parameters $a = 3$ mm and $\Delta\sigma = 5$ MPa. Note that this selection of a is consistent with the size of the region covered by the wire debris particles discussed in section 2. As P varies from 8 to 16 MPa, L_c varies from 6 mm to 3 mm, and a/L_c varies from 0.5 to 1.0. In comparison to the results (2.2) of Xia *et al.* (2004), the simulated transition distances in our model are 30% to 40% smaller, indicating that the dynamic rupture initiation mechanism indeed acts to shorten the transition distance. The ratio of the numerically simulated L to L_c is only about 3 on average. The overall trend with P is similar between the predictions (2.2) and our simulations. The simulated values do not fit the experimental results (shown as dots), underestimating transition distances for lower values of compression P . We have studied a number of different parameters for the rupture initiation procedure, and it seems impossible to make the simulations agree with the experimental values for $D_c = 10$ μm . In particular, as parameters a and/or $\Delta\sigma$ are decreased, the simulated tran-

sition distances for lower values of P remain too short until the initiation procedure fails to initiate ruptures for these lower values of P .

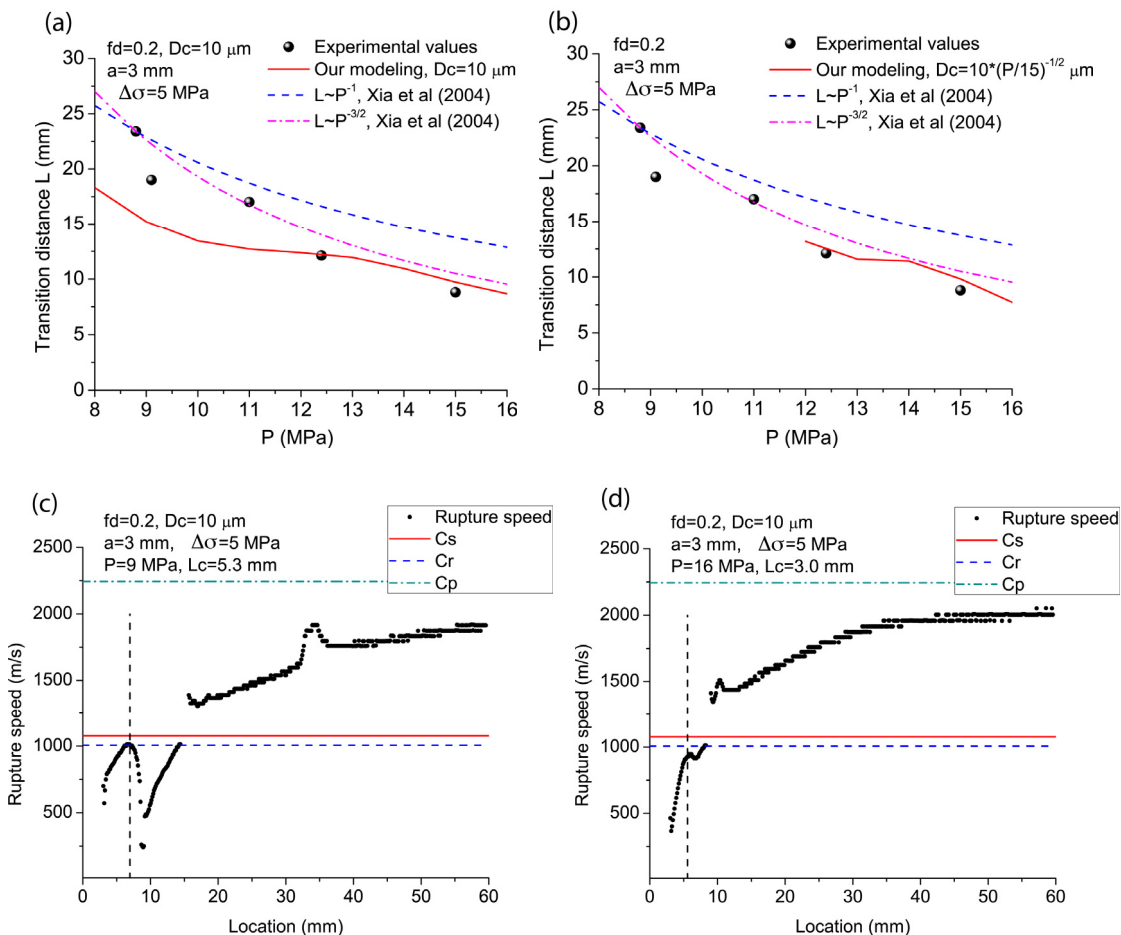


Figure 2.2: Simulation results for $f_d = 0.2$, $\Delta\sigma = 5$ MPa, $a = 3$ mm, and $T_o = 5 \mu\text{s}$. **(a)**

The dependence of supershear transition distances L on the compression P obtained in our simulations with pressure-independent $D_c = 10 \mu\text{m}$ (the solid red curve). The experimental results (dots), the results with pressure-independent $D_c = 10 \mu\text{m}$ (and hence $L \sim P^{-1}$) from Xia et al. (2004) (the blue dashed curve), and the results with pressure-dependent $D_c \propto P^{-1/2}$ ($L \sim P^{-3/2}$) from Xia et al. (2004) (the violet double-dashed curve) are given for comparison. **(b)** An attempt to better fit experimental results in our simulations by incorporating pressure-dependent $D_c \propto P^{-1/2}$ with $D_c = 10 \mu\text{m}$ for $P = 15$ MPa (the solid red curve). In this case, rupture arrests for $P < 12$ MPa. **(c) and (d)** Rupture speed vs. the location of the rupture tip for the cases of $P = 9$ MPa (panel c) and $P = 16$

MPa (panel d), with the pressure-independent $D_c = 10 \mu\text{m}$. The supershear transition distances plotted in Fig. 2a correspond to the location of the crack tip when the speed transition occurs ($L = 15 \text{ mm}$ for $P = 9 \text{ MPa}$ and $L = 8 \text{ mm}$ for $P = 16 \text{ MPa}$). The vertical dashed line corresponds to the rupture tip position at end of the initiation process, when $t = T_o = 5 \mu\text{s}$. For $P = 9 \text{ MPa}$, there is a prominent slow-down in the rupture speed due to the end of the normal stress reduction in the rupture initiation region. For $P = 16 \text{ MPa}$, the rupture speed is reduced much less.

Table 2. 1: Experimentally measured supershear transition distances L for different P

(Xia et al., 2004; Rosakis et al., 2007).

P (MPa)	8.8	9.1	11.0	12.4	15.0
L (mm)	23.4	19.0	17.0	12.1	8.8

The following question arises: Would incorporating the pressure-dependent D_c help to match the transition distances better? Keeping the same $D_c = 10 \mu\text{m}$ for $P = 9 \text{ MPa}$ and decreasing D_c for larger values of P , as done in Xia *et al.* (2004), clearly would not work, as this would simply retain the shorter transition distances for lower P and shorten the transition distances for higher P , making the overall comparison with experimental results even worse. We have confirmed this conclusion in our simulations. However, we can keep the value of $D_c = 10 \mu\text{m}$ for $P = 15 \text{ MPa}$ and increase the value of D_c for

smaller values of P in accordance with (2.5). Theoretically, this should produce the desired effect, as larger values of D_c translate into larger values of L_c and, for the same seismic ratio, potentially result in larger values of the transition distance L . However, simulations for this case show that the initiation procedure fails to start a spontaneous crack for $P < 12$ MPa. The results, in terms of supershear transition distances, are shown in Fig.2.2b (red solid curve). For $P < 12$ MPa, the rupture does not propagate, and hence it does not transition to supershear speeds.

Why does the rupture fail to initiate for smaller values of P ? This is because smaller values of P result in larger critical crack half sizes L_c (everything else being equal), which has two effects on the rupture initiation. First, the ratio a/L_c decreases, so that the normal stress reduction affects a smaller portion of the critical crack size. Second, in the time T_o that the normal stress reduction lasts ($T_o = 5 \mu\text{s}$ here), the rupture tends to acquire a smaller length in proportion of L_c , and hence the rupture may be less developed when the normal stress goes back to its original value and increases the resistance to sliding over a part of the rupture. This effect is discussed further in section 2.3.2. Note that $c_R T_o / L_c$, the related parameter discussed in section 2, varies from 0.6 to 1.7 as P varies from 8 to 16 MPa, illustrating why the rupture would be affected by the end of the rupture initiation procedure for all values of P but especially for smaller P .

2.3.2 Rupture evolution and direct supershear transition at the rupture tip

The typical simulated rupture evolution is illustrated in Fig.2.2(c) and Fig.2.2(d) where the rupture speed is plotted for two cases from Fig.2.2(a), $P = 9$ MPa and $P = 16$ MPa, both with $D_c = 10$ μm . For both cases, the rupture accelerates and approaches the Rayleigh wave speed c_R during the normal-stress reduction in the nucleation region. However, when the normal stress goes back to the original level in the nucleation region (vertical dashed lines in Fig.2.2c and Fig.2.2d), the frictional resistance increases relatively abruptly in the nucleation region causing decrease in slip velocities. When the information about that decrease arrives at the rupture tip, the rupture speed decreases. The decrease in rupture speed is more substantial for the case of $P = 9$ MPa and only slight for the case of $P = 16$ MPa, consistently with our discussion of the differences between lower and higher values of P at the end of section 2.3.1. The critical crack half-sizes L_c are 5.3 mm and 3.0 mm for 9 and 16 MPa, respectively. Fig. 2.2(c) and Fig.2.2(d) show that, at the time of the rupture speed decrease that signifies the end of the normal stress reduction in the initiation region, the rupture lengths are 6.9 mm = $1.3L_c$ for $P = 9$ MPa and 5.6 mm = $1.9L_c$ for $P = 16$ MPa. Hence, at the end of the initiation procedure, the rupture is less developed, in terms of L_c , for $P = 9$ MPa than for $P = 16$ MPa. (This distinction is qualitatively captured by the parameter $c_R T_o / L_c$ discussed in section 2.2, which is equal to 0.9 for $P = 9$ MPa and 1.7 for $P = 16$ MPa, indicating that the crack is likely to be less developed for $P = 9$ MPa.) That is why the rupture slows down much

more for the case of $P = 9$ MPa. In both cases, the rupture recovers and transitions to supershear speeds soon after.

To illustrate how the transition takes place, we plot, in Fig.2.3, two snapshots of the slip velocity and shear stress distribution, one before the transition and one after, for the case of $P = 9$ MPa, $D_c = 10$ μm . The values of shear stress normalized by the normal stress σ_o are shown, with 0.6 corresponding to the static friction coefficient. At the time $t = 16$ μs (Fig.2.3a), the rupture tip is at the location of $x = 14.2$ mm ($x = 0$ corresponds to the middle of the initiation region and hence the middle of the rupture) and the region $0 \leq x \leq 14.2$ mm represents half of the current extent of the rupture. The normalized shear stress value at the location of the rupture tip is 0.6, as appropriate for the point which has just reached the static friction threshold. The shear stress peak at $x = 20$ mm is a classical feature of mode II ruptures described in the work of Burridge (1973) and Andrews (1976). That peak travels with the shear wave speed and represents a pile-up of stress due to shear waves. If the peak reaches the static friction level, a supershear daughter crack would nucleate there, resulting in the Burridge-Andrews transition mechanism. At the time $t = 16$ μs , the shear stress peak is still below the static friction level; Fig.2.2c shows that, when the crack tip is at the location of 14.2 mm, the rupture is still sub-Rayleigh. At $t = 20$ μs , not much has changed in the shape of the shear stress, which

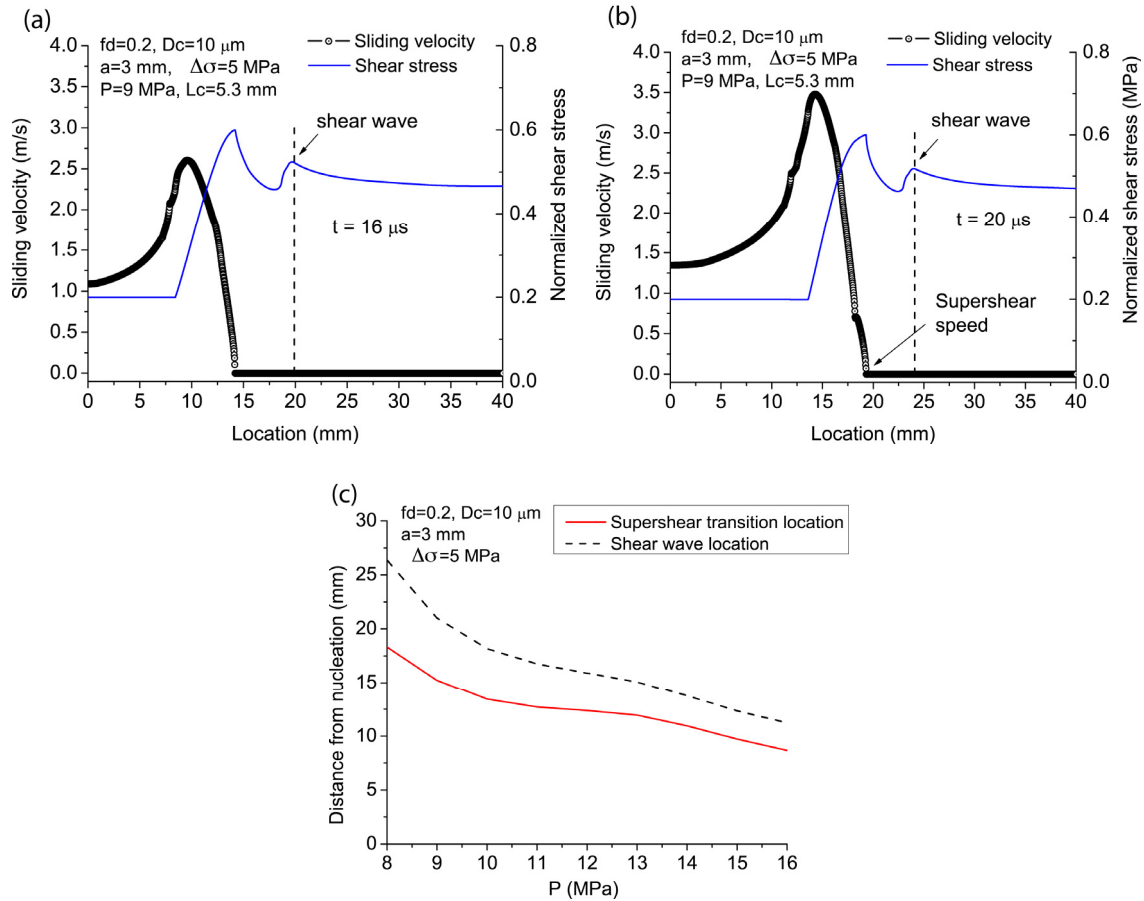


Figure 2.3: An illustration of the direct supershear transition at the rupture tip. **(a) and (b)** Snapshots of sliding velocity and normalized shear stress before and after supershear transition for the simulation of Fig. 2.2c. The shear stress peak traveling with the shear wave speed in front of the main rupture has not yet reached the static friction strength and no daughter crack is initiated. Instead, supershear transition occurs right at the rupture tip as its speed directly jumps from the Rayleigh wave speed to a supershear speed. **(c)** Locations of the shear wave front and rupture tip when supershear transition occurs for the case of Fig. 2.2a. We see that, for all P , the location of supershear transition is behind the shear wave peak.

simply advanced along the interface. However, the rupture front is now at $x = 19.3$ mm, and Fig.2.2c indicates that the rupture is supershear at this point. Clearly, there is no daughter crack, at the shear stress peak or otherwise; rather, we see a perturbation in slip velocities right at the rupture tip, indicating that the crack front itself is transitioning to supershear speeds. This *direct transition at the rupture tip* has been mentioned in the work of Geubelle and Kubair (2001) and studied in detail in Liu and Lapusta (2008) in a different setting with favorable heterogeneities.

Hence we find that supershear transition in this parameter regime occurs by the direct change of rupture speed at the rupture tip, and not by the Burridge-Andrews mechanism. There is an easy way to check this for other values of P . For the case of Fig. 3ab, the actual transition distance is $L = 15.2$ mm. Note that the shear stress peak is ahead by about 5 mm in both snapshots, which means that the shear stress peak was at about $x = 20$ mm at the time of the transition. To check whether the transition occurs at the shear stress peak or not, one can simply plot the transition distance and the location of the shear stress peak at the time of the transition and see whether they coincide or not. This is done in Fig.2.3c, which demonstrates that the shear stress peak is clearly ahead of the supershear transition location for all values of P , indicating that supershear transition occurs not by the Burridge-Andrews (mother-daughter) mechanism but rather by the direct transition at the rupture tip.

2.3.3 Set of parameters that fits experimental data

Section 2.3.1 considers supershear transition distances obtained with the values of D_c inferred by Xia *et al.* (2004). The simulated transition distances with $D_c = 10 \mu\text{m}$ are mostly smaller than the experimental values (Fig.2.2a), especially for lower values of compression P . Based on those results, we have conducted a series of simulations with larger D_c aiming to increase L_c and hence the transition distances L , assuming that L/L_c stays approximately the same. Fig.2.4(a) shows the results for $D_c = 13 \mu\text{m}$ and $a = 5 \text{ mm}$. Overall, the transition distances are matched better than for $D_c = 10 \mu\text{m}$, but discrepancies remain. In particular, the dependence of the simulated transition distances on P is segmented into two parts separated by $P = 12 \text{ MPa}$. Note that, as P varies from 8 to 16 MPa, L_c varies from 7.8 mm to 3.9 mm, a/L_c varies from 0.64 to 1.28, and the ratio of a/L_c acquires the value of 1 at approximately $P = 12 \text{ MPa}$. This means that the rupture initiation procedure is the likely cause of the segmentation, and in particular the rupture slow-down it causes as normal stress returns to the original value in the rupture initiation region. Similarly to the discussion in section 2.3.2, the rupture is not yet well-developed for $P < 12 \text{ MPa}$, in terms of L_c , at the time of the slow-down, and that is why the rupture slow-down is more pronounced for lower P . That results in longer rupture recovery from the slow-down, and hence in larger transition distances than the rupture would have had without the slow-down (Fig.2.4c). For $P \geq 12 \text{ MPa}$, the slow down is

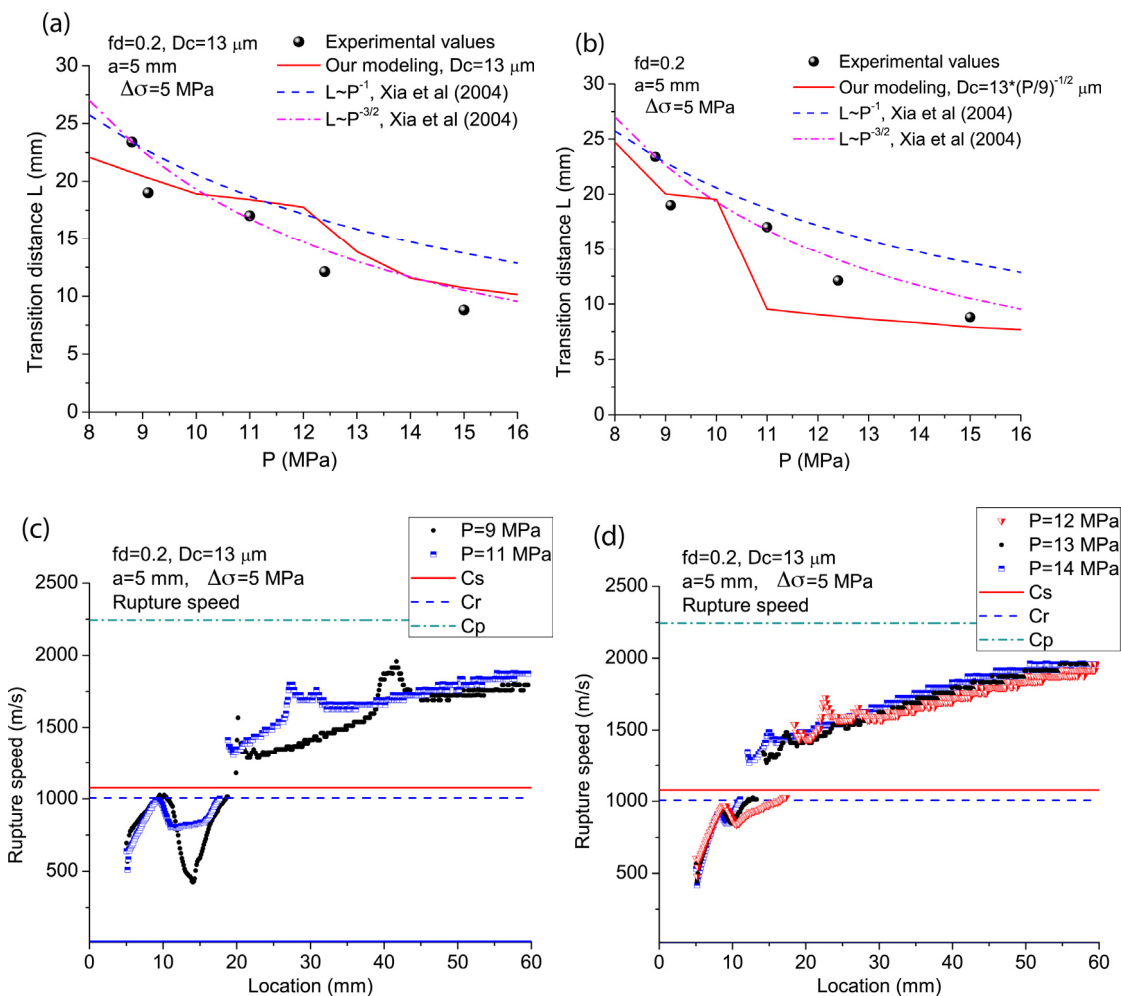


Figure 2.4: Simulation results for $f_d = 0.2$ with a set of parameters that provides a better fit to experimental transition distances. **(a) and (b)** The dependence of the simulated supershear transition distances L on the compression P (solid red curve) for $D_c = 13 \mu\text{m}$ (panel a) and $D_c \propto P^{-1/2}$ with $D_c = 13 \mu\text{m}$ for $P = 9 \text{ MPa}$ (panel b), with $a = 5 \text{ mm}$, $\Delta\sigma = 5 \text{ MPa}$, and $T_o = 5 \mu\text{s}$. The overall fit is improved in comparison to Figs. 2a and 2b; the segmentation of the simulated curves is discussed in the text. The results of Xia *et al.* (2004) are shown for the same parameters as in Fig. 2.2a, for comparison. **(c) and (d)** Rupture speed vs. the location of the rupture tip in the case of pressure-independent $D_c =$

13 μm (Fig. 2.4a) for $P = 9$ MPa, 11 MPa (panel c) and $P = 12$ MPa, 13 MPa, and 14 MPa (panel d). The rupture speed experiences a longer slow-down for the smaller values of P , which is the likely cause of the curve segmentation of Fig. 2.4a.

much smaller and approximately the same for all P (Fig.2.4d), resulting in transition distances decreasing with P in a manner more similar to, if slightly faster than, the results of Xia *et al.* (2004).

In Fig.2.4b, we plot the transition distances L simulated with pressure-dependent $D_c \propto P^{-1/2}$, $D_c = 13$ μm for $P = 9$ MPa. The dependence of L on P is still separated into two trends, similarly to the case of Fig.2.4a. For the pressure-dependent D_c , L_c decreases faster with P than for the case with the constant, pressure-independent D_c of Fig.2.4a, and hence the separating point of the two trends on the transition curve moves from 12 MPa to 10 MPa. The overall agreement of the simulated and experimental values of L is somewhat worse for the pressure-dependent D_c than for the constant one (Fig. 2.4b vs. Fig.2.4a), although it is possible that small adjustments in the parameters of the rupture initiation procedure would result in a better fit.

2.3.4 Dependence of supershear transition on parameters of the rupture initiation procedure

In section 2.3.3, we used the following parameters of the rupture initiation procedure: $a = 5$ mm (with a/L_c varying from 0.64 to 1.28 for the range of P considered), $\Delta\sigma = 5$ MPa, and $T_o = 5$ μ s. Fig.2.5 shows how supershear transition distances are affected when these parameters are varied. Overall, the behavior is not a simple translational change. For example, one might expect that larger values a of the size of the initiation zone would create a larger initial crack, enhance the rupture acceleration, and hence shorten transition distances. However, this expectation is not supported by simulations for some combinations of a and P (Fig.2.5a). This is because the crack evolution history is quite complex and differs for different values of P , as discussed in sections 2.3.2 and 2.3.3, and there are competing effects. One competing effect is that a larger value of a means that a larger part of the expanding rupture will be affected by the end of the initiation procedure, causing a larger slow-down in the rupture speed and delaying the supershear transition. For different values of P , different competing effects win, resulting in complex dependencies shown in Fig.2.5. Similar considerations apply to results for different values of the stress drop $\Delta\sigma$ and explosion duration T_o . Note that all simulations are well-resolved numerically.

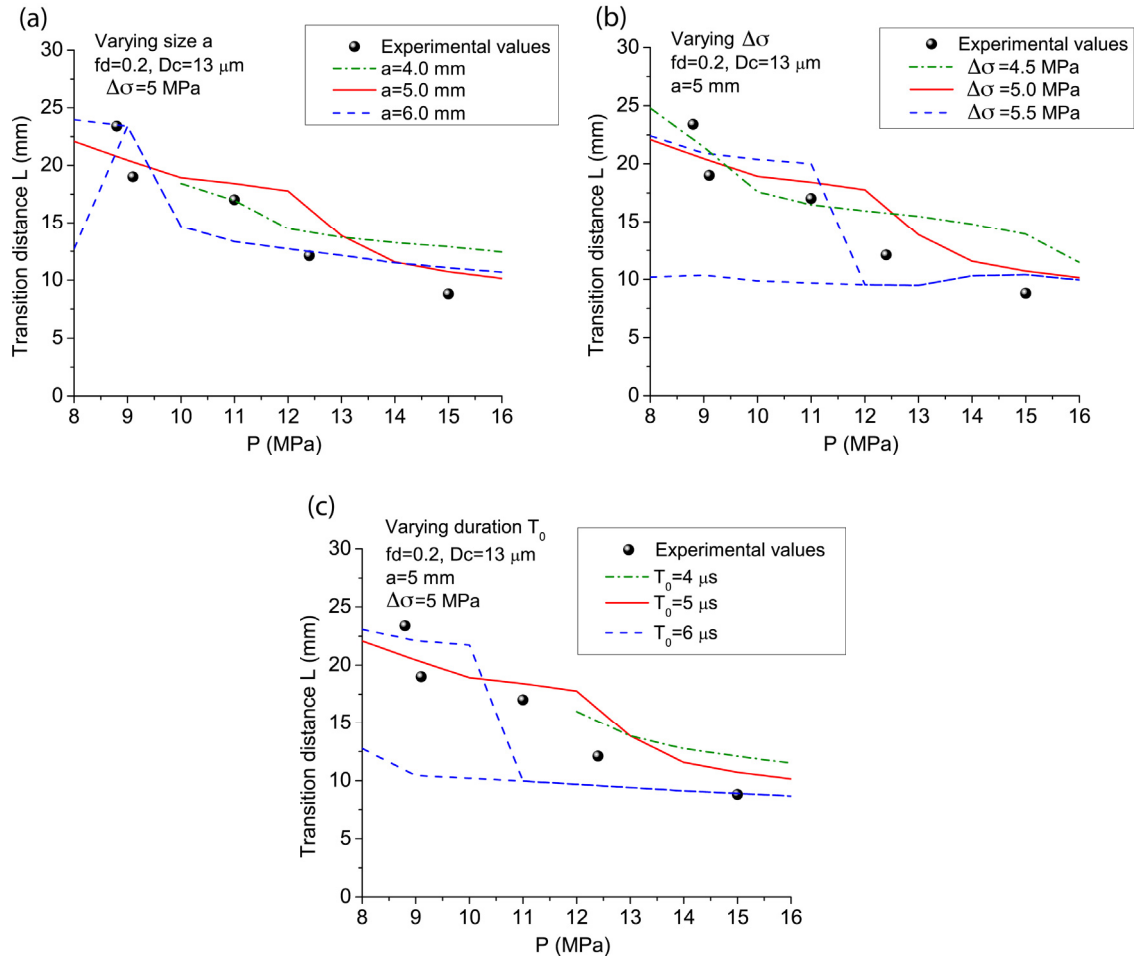


Figure 2.5: Dependence of transition distances on the parameters of the initiation procedure for the case of $f_d = 0.2$ and pressure-independent $D_c = 13 \mu\text{m}$. The reference set of the rupture initiation parameters is that of Fig. 2.4a, $a = 5 \text{ mm}$, $\Delta\sigma = 5 \text{ MPa}$, and $T_0 = 5 \mu\text{s}$. In each panel, one of these parameters is varied and the results are shown for simulations with different values of: (a) the half size a of the rupture initiation procedure, (b) normal stress reduction $\Delta\sigma$, and (c) duration T_0 . In each panel, the blue dashed line gives transition distances for the largest value of the parameter studied, and that line has two branches for lower values of P . The two branches correspond to a failed attempt to transition and then to the actual sustained transition to supershear speeds, as illustrated in Fig. 2.6.

The results shown in Fig.2.5 indicate that, for this parameter regime of direct transition at the rupture tip with relatively small transition distances L/L_c , the transition distances cannot be made much larger than what we see in Fig.2.5. If we use a weaker initiation procedure, with smaller values of a , $\Delta\sigma$, or T_o , then the rupture would fail to initiate for some values of P ; we already see that effect, for smaller values of P , in Fig.2.5a for $a = 4$ mm and in Fig.2.5c for $T_o = 4$ μ s. That is why, after establishing that the transition distances are too short for the case of $D_c = 10$ μ m in sections 2.3.1 and 2.3.2, we could not increase those transition distances simply by varying parameters of the initiation procedure. As a side note, the transition distance L is larger than a by definition, as the location of the crack tip starts as $x = a$ and L is defined as the distance between the middle of the initiation zone ($x = 0$) and the rupture tip when the rupture first acquires supershear speeds. Hence the values of transition distances cannot be smaller than a .

Some parameters of the initiation procedure lead to ruptures that experience two transitions to supershear speeds. This is illustrated in Fig.2.6. The first transition, with the rupture tip at about 10 mm, occurs right when the rupture initiation procedure stops (Fig.2.6a). It takes some time for the rupture front to receive that information through radiated waves, and the resulting slow-down of the rupture makes the rupture transition back to sub-Rayleigh speeds. The rupture recovers and transitions to sustained supershear speeds later, at the location of about 22 mm. In the corresponding plots of the transition distances vs. P , we plot both of the transition attempts, which results in two

branches for dashed blue curves (Fig.2.6b and Fig.2.5). The example of Fig.2.6a is marked in Fig.2.6b by a blue solid circle (for a failed transition attempt) and a blue solid square (for the sustained supershear transition). This behavior helps explain some of the non-monotonic response of the transition distances with the rupture initiation parameters evident in Fig.2.5.

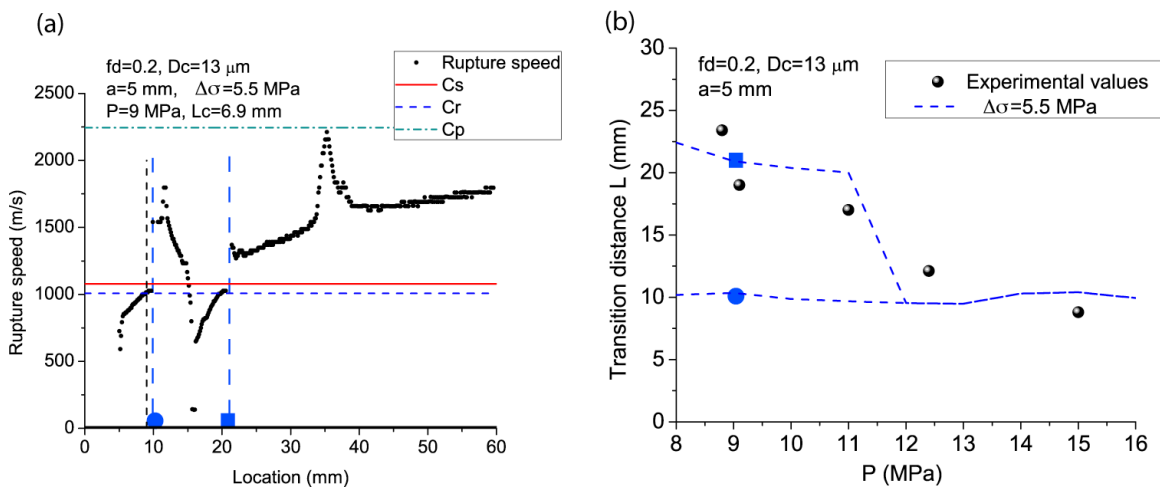


Figure 2.6: A representative case with two supershear transition stages, for $f_d = 0.2$, $D_c = 13 \mu\text{m}$, $a = 5 \text{ mm}$, $\Delta\sigma = 5.5 \text{ MPa}$, and $T_o = 5 \mu\text{s}$. **(a)** Rupture speed vs. the location of the rupture tip for $P = 9 \text{ MPa}$. The failed and successful attempt of supershear transition are marked by a solid blue circle and square, respectively, and blue dotted lines. **(b)** The dependence of transition distances on P . Plotting both the failed and the successful attempt results in two branches for lower values of P .

2.3.5 Dominance of the direct supershear transition for the seismic ratio $s = 0.5$ ($f_d = 0.2$)

In all the cases presented in sections 2.3.1-2.3.4, the transition occurs directly at the rupture front, as discussed in section 2.3.2, before the mother-daughter crack mechanism has a chance to act. We discuss the possible reasons for this dominance in section 2.5, where we compare these cases to the ones of section 2.4. This direct transition mechanism is likely caused by waves radiated from the relatively abrupt initiation procedure. The stress field carried by the waves allows the rupture front to meet the static friction threshold with supershear speeds, causing the direct transition. (In fact, as mentioned in Liu and Lapusta (2008), if the initiation procedure is sufficiently strong, the crack can start with supershear speeds right away.) That is why it is not surprising that the timing and location of the supershear transition for this mechanism are very sensitive to the parameters of the rupture initiation procedure, resulting in non-trivial dependencies discussed in section 2.3.4. For this transition mechanism, the transition distances L/L_c should always be relatively short, in the range of 1 to 3 as observed in sections 2.3.1-2.3.4. This is because the stressing field of the initiation procedure would pass the rupture tip soon after the rupture initiation, when the rupture is still relatively short, and it is at that point that the stress field can influence the rupture tip to transition (or not) to supershear speeds.

If the parameter regime considered in this section is indeed the relevant one for experiments, then a possibility arises that the transition in experiments also happened as the direct transition at the rupture front, and not through the mother-daughter crack mechanism.

This is further discussed in sections 2.5 and 2.6. Note that the experimental measurements have up and down variations with P . One interpretation is that such variations represent experimental variability, hugging what should be a smooth curve similar to the results of Andrews (1976). However, as Figs. 2.2 and 2.4 demonstrate, the dependence of transition distances on P , for this direct mode of supershear transition, is very sensitive to the details of the rupture initiation procedure and values of D_c , resulting in complex segmented plots of L vs. P . Hence it is possible that the variation in experimental results at least partially reflects such complexities.

2.4 Simulations of supershear transition for the seismic ratio $s = 1.0$ ($f_d = 0.34$)

In section 2.3, the dynamic friction coefficient $f_d = 0.2$ is chosen, following Xia *et al.* (2004), which results in the seismic ratio $s = 0.5$ and small nondimensional transition distances. To match the experimental results, values of D_c of about $13 \mu\text{m}$ are required. For that parameter regime, the results indicate that the dynamic rupture initiation procedure has a large impact on the supershear transition, not only significantly shortening transition distances but also resulting in the different transition mechanism, experiencing direct supershear transition of the rupture front.

In this section we explore a different parameter regime that results in the seismic ratio $s = 1.0$ and much larger nondimensional transition distances $L/L_c = 21.5$ based on eq.

(2.2). To obtain $s = 1.0$ in eq. (2.3), we choose $f_d = 0.34$. To match the experimental transition distances, which vary from 10 to 20 mm, we need to have critical crack half sizes of the order of 1 mm, which means that the relevant values of D_c are significantly smaller than in section 2.3.

2.4.1 Good agreement between experimental and simulated transition distances for pressure-independent $D_c = 1 \mu\text{m}$.

The red solid line in Fig. 2.7a shows the transition distances from our simulations in this parameter regime, with pressure-independent $D_c = 1 \mu\text{m}$ and rupture initiation parameters $a = 0.8 \text{ mm}$ and $\Delta\sigma = 3 \text{ MPa}$. Note the good match between the experimental and simulated transition distances. Similarly to section 2.3.1, a is chosen so that a/L_c varies from 0.46 to 0.92, as P varies from 8 to 16 MPa and L_c varies from 1.74 mm to 0.87 mm. The transition distances simulated in our model are 30% to 50% smaller the predictions (2) of Xia *et al.* (2004) based on pressure-independent D_c (and hence $L \sim P^{-1}$). This indicates that the dynamic rupture initiation mechanism acts to shorten the transition distances in this parameter regime as well. However, the ratio of the numerically simulated L to L_c is still quite large, about 12 on average.

The simulated rupture evolution in terms of its rupture speed is shown in Fig. 2.7b-d for three values of P . In all three cases, the rupture accelerates and approaches the Rayleigh

wave speed c_R during the normal-stress reduction in the nucleation region. Unlike in the cases of section 2.3, the rupture speed disruption due to the end of normal-stress reduction is minimal, since, at that point, the rupture is well-developed, with the length of about $3L_c$ to $4L_c$ for different values of P , and the region of normal stress variation constitutes only a small part of the sliding interface. For all three values of P , the rupture propagates with speeds close to c_R for a while before transitioning to supershear speeds. The transition occurs by the Burridge-Andrews (mother-daughter crack) mechanism, as demonstrated in section 2.4.2.

The simulated values of the transition distance L decrease faster with P than the predictions (2.2) of Xia *et al.* (2004) with $L \sim P^{-1}$, which is why the simulated results match the experimental measurements so well, even in this case of pressure-independent D_c . We attribute this faster decrease to the fact that larger values of P correspond to smaller critical crack half sizes L_c and hence larger ratios of a/L_c . This means that larger P are more affected by the rupture initiation procedure. As discussed in section 2.1, that feature was not present in the numerical simulations of Andrews (1976) where the initiation procedure scaled with L_c , and hence it did not enter the subsequent analysis by Xia *et al.* (2004).

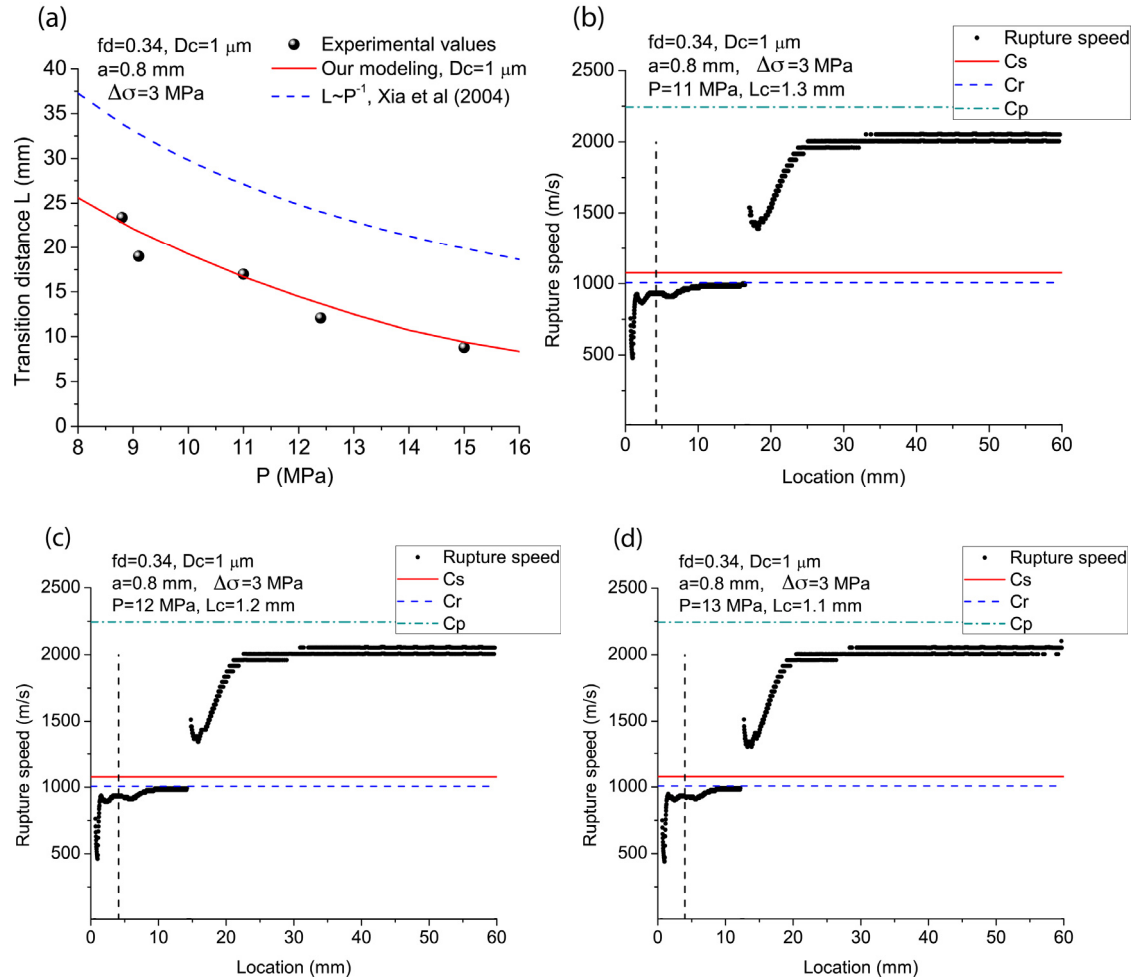


Figure 2.7: Simulation results for $f_d = 0.34$, pressure-independent $D_c = 1 \mu\text{m}$, $\Delta\sigma = 3 \text{ MPa}$, $a = 0.8 \text{ mm}$, and $T_o = 5 \mu\text{s}$. **(a)** The dependence of supershear transition distances L on the compression P in our simulations (the solid red curve). The simulations fit the experimental results (shown as dots) quite well. The transition distances based on the work of Andrews (1976) and the subsequent analysis of Xia et al. (2004) with the pressure-independent $D_c = 1 \mu\text{m}$ (and hence $L \sim P^{-1}$) are 30%-50% larger (dashed blue curve). Note that the vertical axis has a different range compared to Fig. 2.2a, 2.4a. **(b)**-**(d)** Rupture speed vs. the location of the rupture tip for the cases of $P = 11 \text{ MPa}$, 12 MPa ,

and 13 MPa. Vertical dashed lines correspond to the rupture tip position at end of the initiation process, when $t = T_o = 5 \mu\text{s}$. We see that the effect of the end of the nucleation process on the rupture speed is similar for all P and much smaller than for the cases of section 2.3, and that the rupture propagates with speeds close to c_R for a while before transitioning to supershear speeds.

2.4.2 Supershear transition by the Burridge-Andrews (daughter-crack) mechanism

To determine how the supershear transition takes place, we plot, in Fig. 2.8, two snapshots of the slip velocity and shear stress distribution, one right after the transition and one at a later time, for the case of $P = 11 \text{ MPa}$. As in Fig. 2.3, the values of shear stress normalized by the normal stress σ_o are shown, with 0.6 corresponding to the static friction coefficient. At the time $t = 17 \mu\text{s}$ (Fig. 2.8a), the tip of the main rupture is at the location of $x = 15.7 \text{ mm}$ and the region $0 \leq x \leq 15.7 \text{ mm}$ represents half of the current extent of the rupture. The normalized shear stress value at the location of the rupture tip is 0.6. As in Fig. 2.3, there is a shear stress peak in front of the main rupture, at about $x = 18 \text{ mm}$, but, unlike in Fig. 2.3, the shear stress peak is also at 0.6. This has caused the nucleation of a daughter crack at the shear stress peak, which appears on the profile of sliding velocity as a small bump in front of the main rupture. The main rupture and the daughter crack are well-separated at this point in time. At $t = 22 \mu\text{s}$ (Fig. 2.8b), the

daughter crack has grown; it is clearly propagating with supershear speeds, as it has overtaken the shear wave front shown by the red dashed line.

Hence we find that supershear transition in this parameter regime occurs by the classical Burridge-Andrews (mother-daughter crack) mechanism. To show that this is the case for all values of P , we plot, in Fig. 2.8c, the transition distance and the location of the shear stress peak at the time of the transition. As we can see, they almost coincide for all P , indicating that supershear transition occurs at the shear stress peak, and hence by the mother-daughter crack mechanism.

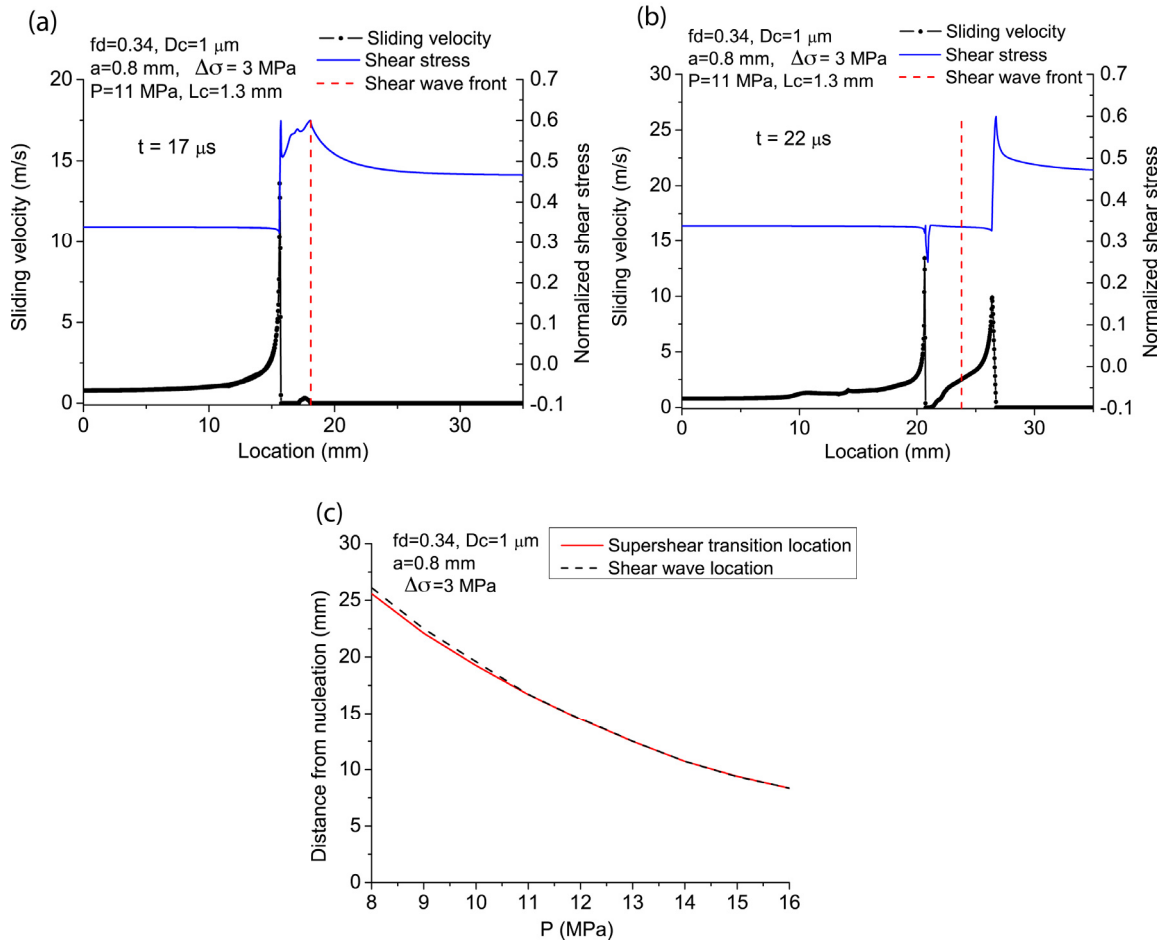


Figure 2.8: Supershear transition by the Burridge-Andrews mechanism. **(a) and (b)** Snapshots of sliding velocity and normalized shear stress right after supershear transition and at a later time for the simulation of Fig. 2.7b. The shear stress peak traveling with the shear wave speed in front of the main rupture has reached the nondimensional static friction strength of 0.6 and a daughter crack is initiated (panel a). The daughter crack has supershear speeds and overtakes the shear wave front (panel b). **(c)** Locations of the shear wave front and rupture tip when supershear transition occurs, for the case of Fig.2.7a. We see that, for all P , the location of supershear transition and the shear stress

peak at the shear wave front coincide, indicating transition by the Burridge-Andrews (mother-daughter crack) mechanism in all cases.

2.4.3 Simulations with pressure-dependent D_c

The effect of using pressure-dependent $D_c \propto P^{-1/2}$ with $D_c = 1 \text{ } \mu\text{m}$ for $P = 9 \text{ MPa}$, is shown in Fig. 2.9. In Fig. 2.9a, the dashed blue line gives transition distances for the pressure-dependent D_c . We see that the transition distances are too short, falling down rapidly for larger values of P . This is because L_c decreases more rapidly with P in this case, so that a/L_c varies from 0.4 to 1.2 as P varies from 8 to 16 MPa. In fact, the very small transition distances for $P \geq 13 \text{ MPa}$ correspond to the rupture transitioning to supershear speeds directly at its tip right after its initiation, with L/L_c of about 1.5 (this phenomenon is discussed further in section 2.4.4). Hence, for this set of parameters, the pressure-dependent D_c does not give a good match to experiments. However, the dynamic friction coefficient and rupture initiation parameters can be slightly adjusted to result in a good fit. For example, selecting $f_d = 0.345$ and $a = 0.55 \text{ mm}$ results in a good match between the experimental results and simulations with pressure-dependent D_c (Fig. 2.9b, blue dashed curve). Hence the experimental results can be matched well with both pressure-independent and pressure-dependent D_c , with small variations in other parameters.

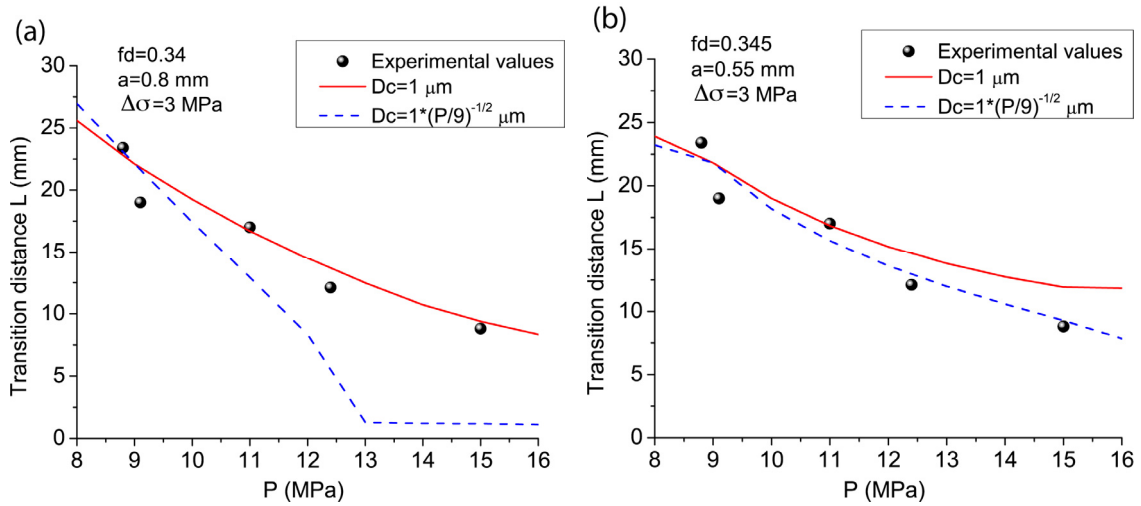


Figure 2.9: Comparison of supershear transition distances L in simulations with pressure-independent $D_c = 1 \mu\text{m}$ (solid red curves) and pressure-dependent $D_c \propto P^{-1/2}$ with $D_c = 1 \mu\text{m}$ for $P = 9 \text{ MPa}$ (dashed blue curves). **(a)** Results for parameters of Fig.2.7a, $f_d = 0.34$, $\Delta\sigma = 3 \text{ MPa}$, $a = 0.8 \text{ mm}$, and $T_o = 5 \mu\text{s}$. Pressure-independent D_c fits the experimental measurements well in this case, while pressure-dependent D_c does not. **(b)** Results for slightly modified parameters $f_d = 0.345$, $\Delta\sigma = 3 \text{ MPa}$, $a = 0.55 \text{ mm}$, and $T_o = 5 \mu\text{s}$. In this case, pressure-dependent D_c results in a good match.

2.4.4 Dependence of supershear transition on parameters of the rupture initiation procedure and cases with the direct supershear transition

In sections 2.4.1, 2.4.2, and part of 2.4.3, we used the following parameters of the rupture initiation procedure: $a = 0.8$ mm (with a/L_c varying from 0.46 to 0.92 for the range of P considered), $\Delta\sigma = 3$ MPa, and $T_o = 5$ μ s. Fig. 2.10 shows how supershear transition distances are affected when these parameters are varied. As in section 2.3.4, the overall behavior is not a simple translational change, although, in this case of larger L/L_c , there is less complexity than in the case of much smaller L/L_c of section 2.3.4. In fact, the response of the transition distances L to variations in the duration T_o (Fig. 2.10c) is what one would intuitively expect, with larger values of T_o corresponding to smaller values of L .

For some values of a and $\Delta\sigma$, the transition distances can be much smaller, as the ones we compute for $a = 0.9$ mm and $P \geq 13$ MPa (Fig. 2.10a), and for $\Delta\sigma = 3.5$ MPa and $P \geq 13$ MPa (Fig. 2.10b). The origin of such much smaller transition distances is the change in the transition mechanism from the Burridge-Andrews mechanism to the direct transition at the rupture tip. This is illustrated in Fig. 2.10a, which shows that the supershear transition for $P = 9$ MPa occurs through the classical mother-daughter crack mechanism, while the supershear transition for $P = 15$ MPa occurs directly at the rupture front. In the latter case, we see that the rupture history is such that no shear stress peak has developed in front of the rupture at the time of the transition. The normalized transition distances for the direct transition mechanism are small, e.g., $L/L_c = 1.7$ for $P = 15$ MPa, consistently with our discussion in section 2.3.5.

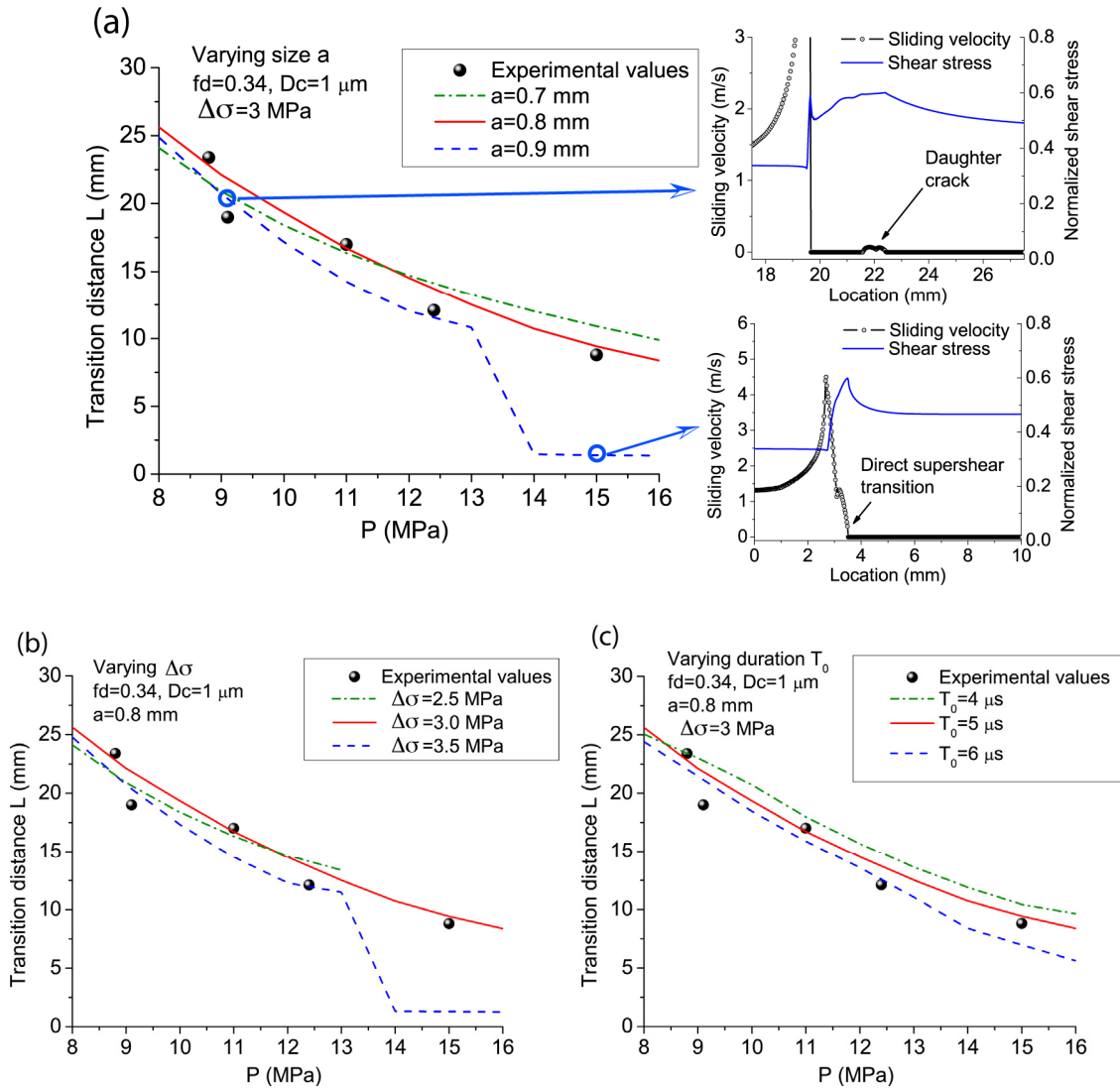


Figure 2.10: Dependence of transition distances on the parameters of the initiation procedure for the case of $f_d = 0.34$ and pressure-independent $D_c = 1 \mu\text{m}$. The reference set of parameters is that of Fig. 2.7a, $a = 0.8 \text{ mm}$, $\Delta\sigma = 3 \text{ MPa}$, $T_0 = 5 \mu\text{s}$. In each panel, one of these parameters is varied and the results are shown for simulations with different values of: (a) the half size a of the rupture initiation procedure, (b) normal stress reduction $\Delta\sigma$, and (c) duration T_0 . In panel (a), the snapshots of sliding velocity and shear stress for two values of P show that, for $a = 0.9 \text{ mm}$, supershear transition occurs by the Burridge-

Andrews mechanism for smaller P and by the direct transition at the rupture tip for larger P .

2.5 Discussion of the two regimes in parameter space

Our simulations with the rupture initiation procedure that mimics the effects of the wire explosion show that the rupture can transition to supershear speeds by two mechanisms: the direct transition at the rupture tip (sections 2.3.2 and 2.3.5), and the Burridge-Andrews (or mother-daughter crack) mechanism (section 2.4.2). Our goal has been to identify parameter combinations which would match all experimentally determined transition distances. After considering cases with two different values of the seismic ratio, $s = 0.5$ (section 2.3) and $s = 1.0$ (section 2.4), we have found that, in all scenarios with $s = 0.5$ that match experimentally observed values, the transition occurs directly at the crack tip, while in the regime of $s = 1.0$, one can find parameters of the initiation procedure and critical slip D_c that lead to a good match with experimental values for the Burridge-Andrews mechanism.

As discussed in section 2.3.5, the direct transition mechanism is likely caused by the relatively abrupt radiation of waves from the rupture initiation procedure. That stress field, when passing by the rupture tip, can enable the tip to meet the static friction threshold with supershear speeds. Note that the nature of typical elastodynamic stress fields is such that stress increases propagate with speeds between the shear wave speed and the dilata-

tional wave speed, and with speeds below the Rayleigh wave speed, while stress decreases propagate with speeds between the Rayleigh wave speed and the shear wave speed. That is why rupture speeds, driven by the elastodynamic stress fields of the problem, are either sub-Rayleigh or supershear. If the relatively abrupt stress field radiated by the rupture initiation passes by the rupture tip without causing the direct transition, then the crack remains sub-Rayleigh until, for sufficiently small seismic ratios s , it develops a large enough shear stress peak in front and transitions to supershear speeds by the mother-daughter crack mechanism.

The parameter regime of section 2.3 may favor the direct supershear transition for several reasons. It has a lower seismic ratio $s = 0.5$ that promotes supershear transition. It has a higher stress drop, $(\tau_0 - \tau_d) / \sigma_0 = f_0 - f_d$. Another difference between the two parameter regimes is the values of the parameter $c_R T_o / L_c$ which estimates how long (or developed) the rupture is at the end of the initiation procedure. If the rupture is relatively short at that time, with $c_R T_o / L_c$ of about 1 or 2, then the initiation region is still a large fraction of the overall rupture length and the rupture has to be vigorous enough to survive the slow-down in the initiation region. That requires a stronger initiation procedure which would also promote the direct supershear transition. That is exactly what happens for the cases in sections 2.3.1-2.3.4 where, depending on the rupture initiation parameters, the rupture either arrests shortly after the end of the initiation procedure or survives but then experiences the direct transition to supershear speeds at the rupture tip. In sections 2.4.1-2.4.3, $c_R T_o / L_c$ is much larger, more than 3, which means that the crack is well developed at the end of the initiation procedure, and the end of the initiation procedure does not

have a significant effect. That allows us to use a more gentle initiation procedure in sections 2.4.1-2.4.2 (with $\Delta\sigma = 3.0$ MPa and not 5 MPa as in section 3), which leads to sustained rupture propagation but not the direct supershear transition.

Can we distinguish between the two transition mechanisms in the experiments? In Xia *et al.* (2004), the rupture progression was captured by photoelastic images taken every $2 \mu\text{s}$ which, for the rupture propagating close to the Rayleigh wave speed, translates into spatial resolution of the crack tip position of 2 mm. However, the supershear rupture is clearly identifiable on the images only after it generates visible Mach cones, i.e., some time after the transition. Hence it is not easy to distinguish between the daughter crack which nucleates 1-3 mm in front of the crack tip and a supershear surge of the main crack tip itself.

A more promising approach is to compare slip velocity histories from simulations and from experiments. These experimental measurements can be done using laser velocimeters (Lykotrafitis *et al.* 2006; Lu *at al.* 2007; Rosakis *et al.* 2007). In particular, Lu *at al.* (2007) recently reported experimental observations of both pulse-like and crack-like ruptures, some of which transitioned to supershear speeds in the time window of the observations. The experimental set-up was the same as in Xia *et al.* (2004) with the addition of laser velocimetry. The experimental conditions such as surface preparation, capacitor discharge etc. were slightly different, potentially resulting in a slightly different static friction coefficient, intensity of the wire explosion etc. Fig. 2.11a shows one of the experimental slip velocity profiles, measured at the distance of 40 mm from the explosion

site, for the inclination angle $\alpha = 30^\circ$ and $P = 14$ MPa. The dashed line shows the shear wave arrival at the location. Since the rupture has arrived before the shear waves, we know that the rupture is supershear as it arrives at this location. There is a prominent peak right behind the shear wave arrival. Note the oscillations with the period of about $5 \mu\text{s}$ present in the slip velocity profile; this is likely the 3D effect of the thickness of the plate (which is 10 mm) perhaps combined with the effect of the finite duration of the wire explosion.

How does this profile compare with the ones in our simulations? Fig. 2.11b shows the slip velocity profile for a case from section 2.3, with $f_d = 0.2$, $s = 0.5$, $D_c = 13 \mu\text{m}$, which results in the direct supershear transition at the rupture tip. The overall shape is similar between Fig. 2.11a and 2.11b, but the slip velocity values are higher in Fig. 2.11b. Although the rupture tip itself has transitioned to supershear speeds, there is still a decrease and increase of slip velocities behind the supershear rupture tip which is the signature of shear and Rayleigh waves that are left behind. Fig. 2.11c shows the slip velocity profile for a case from section 2.4, with $f_d = 0.34$, $s = 1.0$, $D_c = 1 \mu\text{m}$, which results in the mother-daughter crack transition mechanism. Again, the overall shape is similar between Fig. 2.11a and 2.11c. The experimental measurements are done on the surface of the sample and at a small distance away from the interface, plus Homalite may exhibit some nonlinear elastic or inelastic behavior at the rupture tips. All these factors would prevent the experiments from recording high slip velocities right at the crack front, or sharp short-lived drops of slip velocity to zero, that are seen in simulations. Other than that, even the level of slip velocities matches in this case, and the simulated profile of

Fig. 2.11c has a more pronounced peak behind the shear wave front than that in Fig. 2.11b, consistently with the experimental measurement in Fig. 2.11a.

Hence both transition mechanisms result in slip velocity profiles that qualitatively match the experimental results. The case with the mother-daughter crack transition does a somewhat better job, although this comparison is necessarily qualitative, since there are a lot of adjustable parameters. However, such comparisons should yield valuable insights when more aspects of the experiments are quantified (most importantly, the parameters of the initiation procedure).

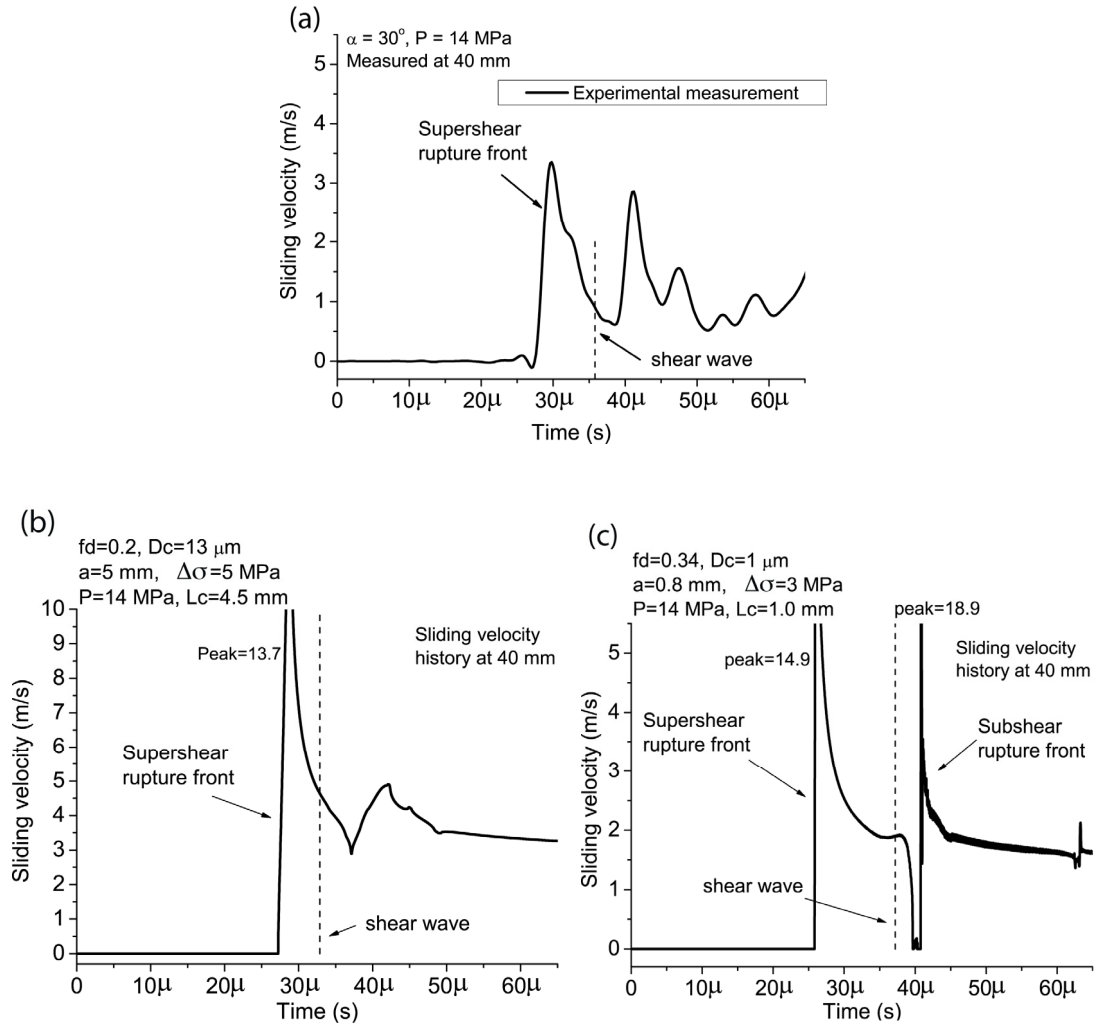


Figure 2.11: Slip velocity histories at the location of 40 mm along the interface for (a) an experimental measurement of Lu *et al.* (2007), (b) a simulation with the direct supershear transition at the rupture tip, and (c) a simulation with the Burridge-Andrews transition mechanism. In all cases, the supershear transition has already occurred, since the rupture tip arrives at this location faster than the shear wave front indicated by the dashed vertical line. Overall, the shape of the slip-velocity profile is similar for all three cases.

2.6 Conclusions

Motivated by the experiments of supershear transition by Xia *et al.* (2004), we have investigated the effect of a dynamic rupture initiation procedure and fault friction on supershear transition in a plane-stress model with an interface governed by linear slip-weakening friction. To mimic the effects of the wire explosion, our initiation procedure reduces normal stress over a part of the interface for a given time. The values of the static friction coefficient, fault prestress, and bulk material properties are well-known for the experimental setup of Xia *et al.* (2004), and we have assumed the corresponding values in this work. However, the dynamic friction properties of the experimental interface and the parameters of the wire explosion are not precisely known, and we have considered several plausible possibilities. While that introduces several adjustable parameters, the requirement that simulations match experimentally observed transition distances for a range of experimental conditions relates parameters to each other and restricts their values.

We find that the dynamic rupture initiation procedure can significantly affect the supershear transition observed in the experiments. First of all, it introduces the possibility of the direct supershear transition at the rupture tip, in which the rupture tip abruptly changes its speed from the values approaching the Rayleigh wave speed to supershear speeds. This direct transition is likely caused by the stressing wave field radiated by the relatively abrupt initiation of sliding over a part of the interface, and hence it is dominated by the parameters of the initiation procedure. The transition distances for the direct

transition are relatively small, 1.5 to 3 L/L_c in the cases we have studied, so that the direct transition occurs soon after the rupture initiation, with no obvious dependence on the value of the seismic ratio s (which determines transition distances in the study of Andrews, 1976 and Xia *et al.*, 2004, through the mother-daughter crack mechanism). Since the transition distances L in the experiments of Xia *et al.* (2004) varied from 10 to 24 mm for different far-field compressions P , the direct transition mechanism can only be relevant to experiments if the values of the critical crack sizes are 3 to 8 mm (assuming $L/L_c = 3$ and equal for all P) or larger (assuming $L/L_c < 3$). To initiate spontaneous rupture, the half size a of the region affected by the wire explosion has to be a significant fraction of L_c . Hence a has to be several mm in this case (in section 2.3, the half size $a = 5$ mm gives a relatively good fit to experimental data). Such values of a require a 0.1-mm wire to significantly affect a much larger region of 10 mm or so.

The Burridge-Andrews mechanism of a supershear daughter crack can still occur for some parameter combinations, although the dynamic initiation procedure significantly shortens, by about 30% to 50% in the cases we studied, the nondimensional transition distances L/L_c compared to the study of Andrews (1976) and the calculations of Xia *et al.* (2004) and Rosakis *et al.* (2007), which assumed an initiation procedure representative of a gradually accelerating rupture. This is because the dynamic rupture initiation promotes the development of the shear stress peak in front of the main rupture, which then reaches the static friction threshold for shorter propagation distances in comparison to the above-mentioned studies. Still, the daughter-crack mechanism, even in the presence of the dynamic rupture initiation procedure, can produce much larger values of

L/L_c than the direct-transition mechanism, for suitably chosen seismic ratios s . This allows our simulations to match the experimental observations for smaller values of L_c . For example, in sections 2.4.1-2.4.2, we find a good match for $2L_c$ of the order of 2 mm. This would require that a much smaller extent of the interface affected by the explosion, 2 mm or less (we use the half-size $a = 0.8$ mm in sections 2.4.1-2.4.2), compared with 10 mm for the direct transition ($a = 5$ mm in section 2.3).

As mentioned in section 2.2, post-experimental surfaces contain a thin layer of metallic debris around the explosion site, which shows how much the material of the wire spread after the explosion. The spatial extent of the layer is typically 4-10 mm along the interface, which would indicate that the half-size a is 2 to 5 mm. This estimate is broadly consistent with the values of a we have used in sections 3 and 4. However, it does provide a firm constraint. On the one hand, one can argue that this estimate may be more of an upper bound, since, in our modeling, $2a$ presents the size of the region that is significantly affected by the explosion, in terms of the resulting normal stress decrease, while the edges of the region covered by the metallic debris may have had only small or negligible normal stress change. This argument would favor smaller values of a , pointing to the parameter regime with the Burridge-Andrews transition mechanism. On the other hand, the size of the particle-covered region may in fact give the value of a more directly, or even underestimate it, which would favor larger values of a as we used in the cases of the direct transition.

In sections 2.3 and 2.4, we have found reasonable parameter regimes that match experimental transition values with both direct supershear transition at the rupture tip and the Burridge-Andrews mechanism, using both pressure-independent and pressure-dependent critical slip D_c . Hence our study shows, in part, that the experimental results do not necessarily imply the pressure dependence of D_c , once the effect of the rupture initiation procedure is taken into account.

This work underscores the importance of further quantifying experimental parameters for proper interpretation of the experiments and for designing new ones. In particular, the time- and space-dependent effects of the wire explosion need to be determined, and such study is our first priority. It is possible that the wire explosion temporarily opens a part of the interface, a factor not considered in this study. It is also possible and even likely, based on the study of Lu *et al.* (2007), that the interface friction is better described by a rate- and state-dependent law with significant rate-dependence at high slip rates rather than a linear slip-weakening law used in this work. We plan to incorporate these effects into our future modeling.

Chapter 3

Rupture Modes in Laboratory Earthquakes: Effect of Fault Prestress and Nucleation Conditions

3.1 Introduction

In this Chapter, we adopt and further develop the experimental setup of Xia et al. (2004), and then use it to study pulse-like and crack-like rupture modes. The issue of rupture modes has important implications for fault constitutive laws, stress conditions on faults, energy partition and heat generation during earthquakes, scaling laws, and spatio-temporal complexity of fault slip. Early theoretical models treated earthquakes as crack-like ruptures, but seismic inversions indicate that earthquake ruptures may propagate in a self-healing pulse-like mode. A number of explanations for the existence of slip pulses have been proposed and continue to be vigorously debated. This Chapter presents first experimental observations of spontaneous pulse-like ruptures in a homogeneous linear-elastic setting that mimics crustal earthquakes, reveals how different rupture modes are selected based on the level of fault prestress, demonstrates that both rupture modes can

transition to supershear speeds, and advocates, based on comparison with theoretical studies, importance of velocity-weakening friction for earthquake dynamics.

This Chapter is based on Lu, Lapusta, and Rosakis (PNAS, 2007) and Lu, Rosakis, and Lapusta (JGR, manuscript in preparation).

3.2 Experimental design

3.2.1 Configuration that mimics crustal earthquakes

Our experimental setup mimics a fault in the Earth's crust that is prestressed both in compression and in shear (Xia et al., 2004). A square Homalite plate (Figure 3.1a), with the dimensions $150 \text{ mm} \times 150 \text{ mm} \times 10 \text{ mm}$, is cut into two identical quadrilaterals, introducing a fault plane with an inclination angle α with respect to one set of the plate edges. Unidirectional compression P is applied to the edges. The fault surfaces are treated to create the same texture and hence the same friction properties in all specimens, as described in section 3.2.3. Experimental parameters P and α determine the resolved shear traction $\tau_0 = P \sin \alpha \cos \alpha$ and normal traction $\sigma_0 = P \cos^2 \alpha$ on the fault. The non-dimensional shear prestress $f_0 = \tau_0 / \sigma_0 = \tan \alpha$ indicates how close the interface is to failure according to the Coulomb criterion. Because the static friction coefficient of the interface is about 0.6, the inclination angle α is chosen to be 30 degrees or smaller to

ensure that sliding does not occur during the static preloading stage. By varying α , we can consider the effect of different levels of nondimensional fault prestress on rupture dynamics. Varying P allows us to study the effect of the absolute prestress level.

Dynamic rupture is initiated in the middle of the plate and captured using high-resolution dynamic photoelasticity and laser velocimetry (section 3.2.4). The rupture is triggered simultaneously across the entire thickness of the plate using an explosion of a thin wire as described in section 3.2.2. As the result, the rupture is dominated by 2D in-plane slip, similarly to large strike-slip earthquakes that saturate the entire seismogenic depth. The bilaterally spreading rupture is observed only until reflected waves return from the edges of the plate, to enable comparisons with models of dynamic rupture in infinite elastic media. A typical observation window is 65 μs .

Elastic properties of the bulk material, Homalite, are well documented (Dally and Riley, 1991): Young's modulus $E = 3.86$ GPa, shear modulus $\mu = 1.43$ GPa, Poisson's ratio $\nu = 0.35$, density $\rho = 1200$ kg/m³, shear wave speed $C_s = 1249$ m/s, longitudinal wave speed $C_p = 2187$ m/s, and Rayleigh wave speed $C_R = 1155$ m/s. Homalite has about 20 times smaller shear modulus than typical rock materials. Since critical crack sizes and nucleation sizes are proportional to shear modulus, smaller shear modulus for Homalite translates into smaller critical length scales, assuming similar friction properties for rocks and Homalite. This enables us to reproduce rupture phenomena in smaller samples than would be needed for rocks.

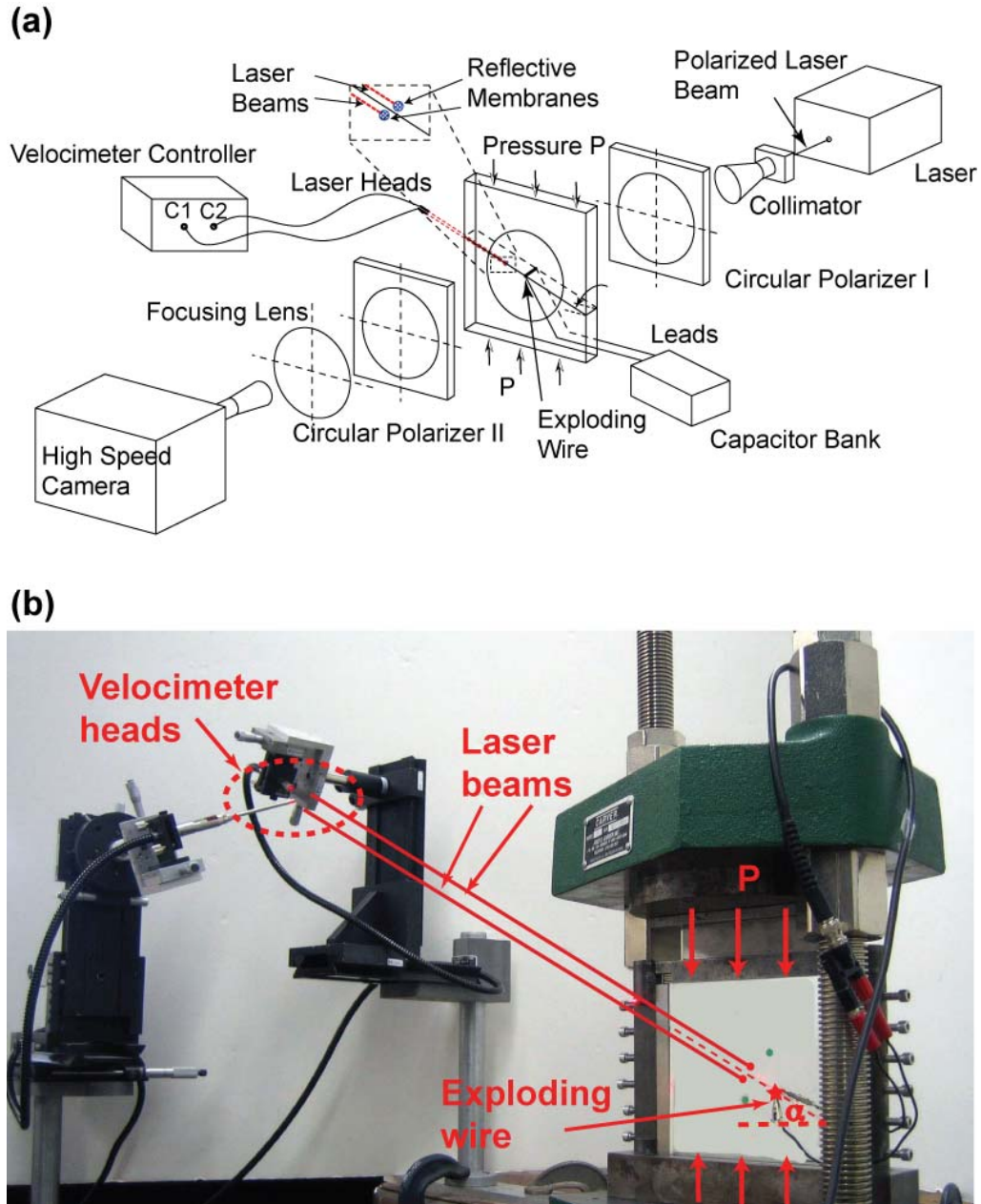


Figure 3.1: (a) Schematic illustration of the experimental configuration. Homalite samples are cut with an inclination angle α and compressed with the far-field load P . Dynamic photoelasticity and laser velocimetry are used to capture the full field information of rupture propagation as well as local sliding velocity of the interface. Rupture nucleation is achieved by a local pressure release due to an explosion of a thin wire. (b) A photograph of the experimental setup.

3.2.2 Mechanism of rupture nucleation

Initiation of dynamic rupture is achieved by an explosion of a thin wire. A nickel wire with a diameter of 0.08 mm is embedded within a 0.1-mm hole across the entire plate thickness. The ends of the wire are connected to a charged capacitor. By abrupt discharge, the stored electric energy is released and the surge of the current turns the wire into plasma. The explosion relieves fault-normal compression locally, decreasing friction and allowing shear rupture to start under the action of the resolved shear stress in a region around the explosion site. Afterwards, dynamic rupture propagates spontaneously outside the nucleation region, since (i) rupture concentrates shear stress at its tips, matching static friction outside the area affected by the explosion and spreading farther, and (2) fault locations behind the rupture front experience dynamic reduction in friction strength, as would be expected from either slip-weakening or velocity-weakening friction.

The nucleation mechanism of the wire explosion has a number of experimental advantages. The electric signal that causes the explosion enables synchronization of multiple diagnostic instruments. Rupture initiation is achieved with known and adjustable stress conditions outside of the nucleation region. The initiation procedure is repeatable, allowing us to reproduce the same experimental conditions multiple times while taking different diagnostic measurements, such as velocimeter measurements at different locations.

At the same time, the initiation procedure introduces additional complexity. It is different from the process of gradually accelerating slip occurring under slow stress increase due to tectonic loading obtained in a number of earthquakes models (e.g., Lapusta et al., 2000). However, it is conceptually representative of earthquake nucleation by rapid stress changes due to seismic waves. Numerical simulations of dynamic rupture have shown that details of rupture initiation can significantly affect the subsequent rupture propagation (Festa and Vilotte, 2006; Shi and Ben-Zion, 2006; Liu and Lapusta, 2007; Shi and Ben-Zion, 2007; Lu et al., 2008). Hence it is important to understand the effect of the initiation procedure on dynamic rupture in our experiments. To that end, we conduct experiments with explosions of different strength and perform fault-normal velocity measurements outside the nucleation region, as discussed in section 3.3.6.

3.2.3 Surface preparation for specimens

For meaningful comparison between different experiments and for experimental repeatability, it is critical for all specimens to have the same surface preparation and hence the same friction properties. We have developed a controlled surface preparation procedure. As shown in Figure 3.2a, the original surface obtained from machining has periodic cutting scratches. By polishing it with a diluted solution of Miromet polishing compound, we are able to remove the scratches and make the surface transparent (Figure 3.2b). The next step is to use a bead blaster to roughen the polished surface. Fine glass beads of 44

μm to $88 \mu\text{m}$ in diameter are driven by compressed air out of the nozzle and strike the polished surface, creating the same surface texture in all samples (Figure 3.2c). Three-dimensional scanning by a surface profiler (Figure 3.2d) gives the average roughness of $R_a = 4.5 \mu\text{m}$. The average roughness is defined as the average height of the surface profile.

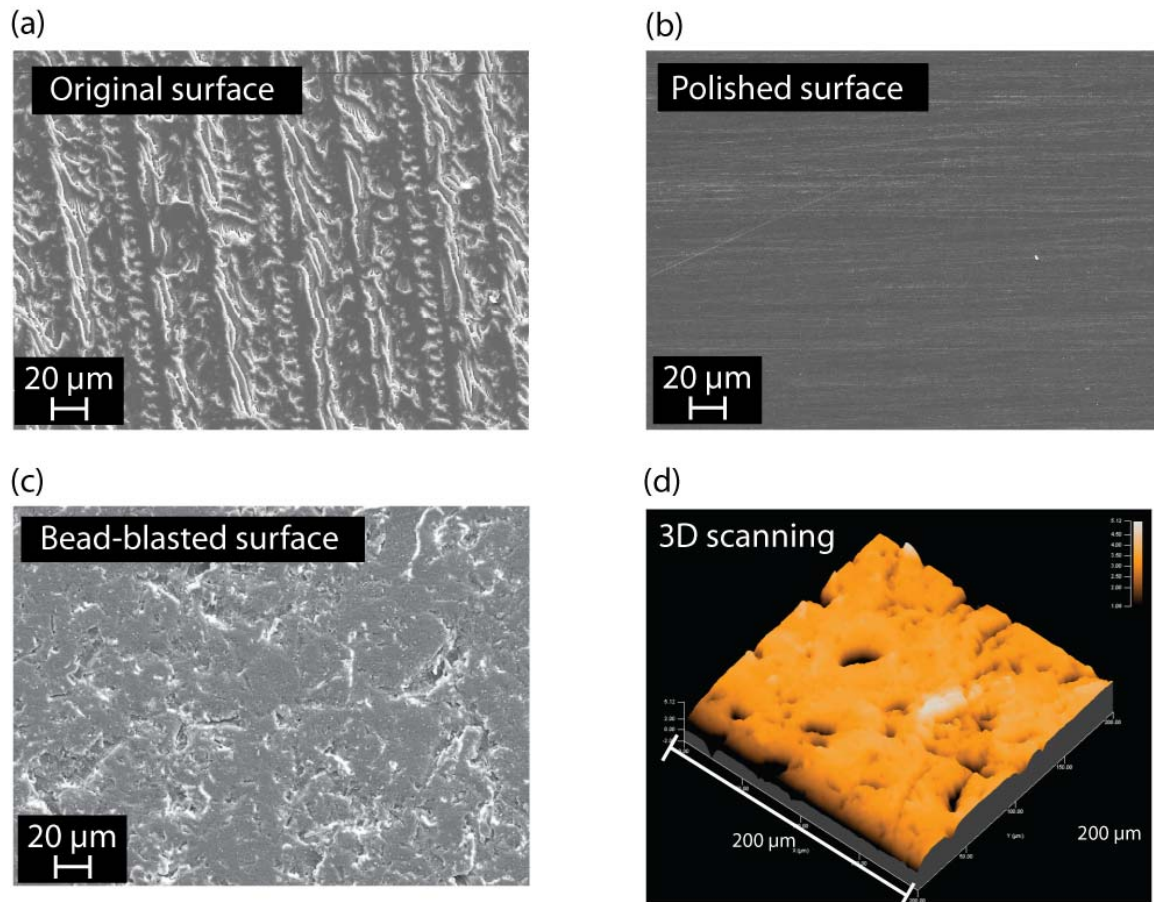


Figure 3.2: Surface preparation of specimens. (a) SEM (Scanning Electron Microscopy) image of the specimen surface after cutting, showing periodic scratches. (b) SEM image

of the polished surface of the specimen. (c) SEM image of the surface roughened by bead-blasting. (d) 3D scanning image of the final sliding surface by a surface profiler.

3.2.4 High-resolution diagnostics: dynamic photoelasticity and laser velocimetry

As shear rupture grows bilaterally away from the nucleation region, high-speed photography, in conjunction with dynamic photoelasticity, is used to capture full-field images of the transient dynamic event. As shown in Figure 3.1a, collimated laser beams are used to illuminate the transparent specimen. A pair of circular polarizers, one in front of and one behind the Homalite specimen, creates a fringe pattern that represents contours of maximum shear stress. The shear stress in each fringe is given by the stress optical law, $2\tau_{\max} = \sigma_1 - \sigma_2 = NF_{\sigma} / h$, where F_{σ} is the material's stress optical coefficient, h is the specimen thickness, σ_1 and σ_2 are the principal stresses, and $N = n + 1/2$ (with $n = 0, 1, 2, \dots$) is the isochromatic fringe order. A digital high-speed camera is positioned at the end of the optical axis to record a series of 16 photoelastic images with the programmable inter-frame time that can vary from 2 to 4 μs .

In addition to the full-field photoelastic images, we use two velocimeters based on laser interferometry to measure particle velocity histories of two points, one above and one below the fault interface (Figure 3.1b). Two reflective membranes are glued at the points of

interest, and two separate laser beams are focused on the sides of the two membranes to record either the fault-parallel or fault-normal particle velocity. The size of the each laser beams is $66\ \mu\text{m}$ and the distance between the two measurements is about $500\ \mu\text{m}$. The difference between the two measured fault-parallel particle velocities represents the interface sliding velocity plus elastic deformation between the two measurement points. As discussed in section 3.3.2, the elastic deformation is taken into account when the onset and healing of the interfacial sliding is determined. The maximum frequency response of the velocimeters is $1.5\ \text{MHz}$, which is fast enough to track rapid particle velocity changes during dynamic rupture. The velocimeters can measure particle velocity of up to $10\ \text{m/s}$, enabling us to record high slip velocity at rupture fronts.

3.3 Experimental measurements and their interpretation

3.3.1 Measurements of particle velocity and full-field photoelastic snapshots

Let us use representative experimental results to illustrate the two diagnostic methods (Figure 3.3). In these experiments, the inclination angle is $\alpha = 30^\circ$ and the externally applied compression is $P = 14\ \text{MPa}$. Particle velocity measurements at the location of $20\ \text{mm}$ from the hypocenter are shown in Figure 3.3a. Individual channels marked as “upper” and “lower” correspond to particle velocity histories of points above and below the interface, respectively; the plotted measurements are shifted by $-3\ \text{m/s}$ for clarity. The

particle velocities are approximately anti-symmetric, as would be expected for shear rupture. The oscillatory nature of the traces and deviations from anti-symmetry are discussed in section 3.3.3. The points on the two sides of the interface start to move shortly after $10 \mu\text{s}$ when the P-wave arrives. They move together initially and then, at $13.2 \mu\text{s}$, they exhibit relative motion. The relative motion is the sum of the elastic deformation between the two points and relative sliding, or slip, on the interface. Relative velocity between the two measurement points is computed by subtracting the velocity history of the point below the interface from that above the interface. The green dot indicates our estimate of rupture arrival time or the initiation of relative sliding. Criteria for determining rupture arrival and interface locking are discussed in the next section. The relative velocity reaches the maximum of 7 m/s and it is of the order of 1 m/s throughout the observation window. This means that the interface does not lock during the observation window, indicating what we define to be a crack-like mode. The timing of the shear wave arrival, indicated by a vertical dashed line on the relative velocity trace, provides us with a conclusive way of judging whether rupture is supershear or not. In Figure 3.3a, it is apparent that the rupture is supershear, as it arrives sooner than the shear wave.

To get the slip velocity profile farther along the interface, at the location of 40 mm , another experiment is done under the same experimental conditions (Figure 3.3c). In this case, the P-wave arrival induces a smaller symmetric motion of the points above and below the interface, consistently with the decaying amplitude of the P-wave farther from the hypocenter. The initiation of sliding occurs at $27.8 \mu\text{s}$ and continues throughout the observation window, indicating that the rupture remains crack-like. The rupture front is far-

ther ahead with respect to the shear wave arrival than in Figure 3.3a, confirming supershear propagation.

In order to further analyze the experiment, the relative velocity record is superimposed on the photoelastic fringe map (Figures 3.3b and 3.3d). This superposition, done for visualization purposes, illustrates stress concentrations at rupture tips and converts time-dependent rupture history at one location into an approximation of the space-dependent rupture profile at the time of the photoelastic snapshot. Converting the time history of the sliding velocity into spatial variation along the fault is based on the assumption of a constant rupture speed. Since rupture is equi-bilateral, a mirrored profile (with respect to the nucleation site) is added for visualization purposes. The hypocenter is marked by a star. The circular P-wave and shear wave fronts are marked with dashed lines. Figures 3.3b and 3.3d give the superposition of photoelastic fringe patterns and relative sliding velocity for the times of 16 μs and 40 μs , respectively, illustrating the progression of the rupture along the interface. At the time of 40 μs , the supershear rupture is well developed and two Mach lines are emitted from the supershear rupture tip (Figure 3.3d). The set of 16 photoelastic images allows us to compute the evolution of rupture speed as the rupture propagates along the interface as discussed in section 3.7.1. The combined diagnostics of laser velocimetry and dynamic photoelasticity enables us to conclusively determine both the rupture mode and the rupture speed.

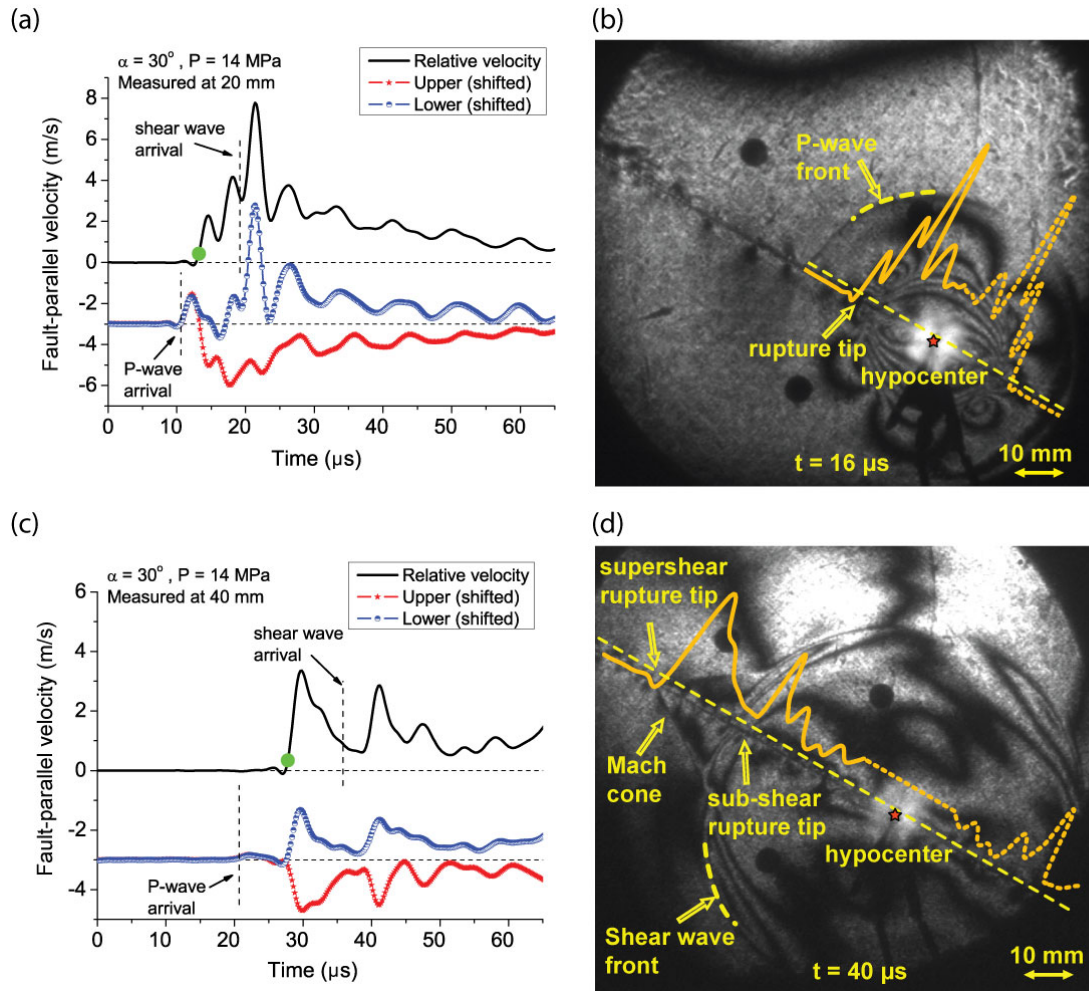


Figure 3.3: Illustration of the experimental diagnostics for an experiment with the inclination angle $\alpha = 30^\circ$ and compressive load $P = 14$ MPa. (a) and (c) Fault-parallel velocity histories measured 20 mm and 40 mm from the rupture nucleation site, respectively. The velocities of the upper and lower measurement points are shifted by 3 m/s. P-wave and shear wave arrivals are indicated by dashed lines. The estimated rupture initiation time is marked by a green dot. Once initiated, the sliding continues throughout the observation window, corresponding to the crack-like rupture mode. The rupture is supershear, since rupture initiation occurs earlier than the shear wave arrival time. (b) and (d) Dynamic photoelastic images captured 16 μ s and 40 μ s after the rupture nucleation, re-

spectively. Fringes represent contours of maximum shear stress. The relative velocity profiles from (a) and (c) are superimposed on the photoelastic images.

3.3.2 Criteria for determining rupture initiation and locking times

In order to consistently identify the timing of both interfacial sliding initiation and interfacial locking (or healing), and thus to determine the rupture duration, criteria are established which account for the elastodynamic shear deformation between the measurement points. Interfacial sliding starts if and only if shear stress τ on the interface is equal to the static friction strength of the interface which, in turn, is equal to normal stress σ times the static friction coefficient f_s . As discussed in section 3.6.1, normal stress σ at the measurement locations is approximately equal to the initial normal stress σ_0 . The difference between the static friction resistance $f_s\sigma_0$ and initial shear stress τ_0 at a point along the interface is overcome by the dynamic shear stress increase arriving with either the rupture tip or the shear wave front. Assuming uniform shear stress between the two measurement points, this difference in shear stress can be converted into a critical relative displacement δ_c that can be sustained between the two measurement points before interfacial sliding initiates. If μ is the shear modulus of Homalite-100 and D is the distance between the two measurement location, the critical displacement is given by:

$$\delta_c = D \frac{(f_s \sigma_0 - \tau_0)}{\mu} = D \frac{P \cos^2 \alpha (f_s - f_0)}{\mu}, \quad (3.1)$$

The time of rupture initiation can be established by integrating the relative velocity records and determining the time at which displacement equal to δ_c is accumulated; this time is marked by green filled dots in Figure 3.3. This time also corresponds to a particular value $\dot{\delta}_c$ of the relative velocity which we call the elastic cut-off velocity. For the experimental conditions of Figure 3.3, the critical displacement δ_c is calculated to be 0.08 μm and the elastic cut-off velocity is $\dot{\delta}_c = 0.43$ m/s. That value of relative velocity is plotted as the yellow dotted interface-parallel line in Figures 3.3b and 3.3d.

To determine when the sliding stops, we employ two criteria. According to the first criterion, sliding stops when the relative velocity becomes smaller than the elastic cut-off value $\dot{\delta}_c$. If the relative velocity decreases below $\dot{\delta}_c$ several times, we take the last time as the time of interface locking. Those times are marked by half-filled red dots in Figure 3.3 and other Figures. The second, more conservative, criterion is to insist that the relative velocity drops to zero and that the integral of relative velocity from that time until the end of observation time is a small fraction (less than 5%) of the total accumulated relative displacement. The corresponding times are marked by fully filled red dots in later Figures. The two different locking criteria produce the same qualitative results with respect to rupture duration and hence rupture mode identification, as discussed in the following sections. In Figure 3.3, the interface at the measurement locations slips throughout the observation window and neither one of the locking criteria are met.

3.3.3 Three-dimensional (3D) effect of the plate thickness

It is important to understand whether the experimental setup is well-described by a 2D plane-stress model, as assumed in the analysis of Xia et al. (2004) and Lu et al. (2008). The plate dimensions, 150 mm by 150 mm, are much larger than the plate thickness of 10 mm, implying that 2D plane-stress approximation should be valid. In addition, the rupture initiation mechanism acts simultaneously through the thickness of the plate (section 3.2.2), further promoting the 2D nature of the resulting stress and strain fields. At the same time, the fact that the stress and strain fields are non-uniform through the thickness of the plate may influence the experimental results; in the following, we refer to such potential influence as “the 3D effect”. In particular, initial stages of rupture propagation over distances of the order of the plate thickness may be influenced by the locally 3D geometry, and that influence may persist at later times through wave-mediated stress transfers and interaction of those waves with the rupture propagation.

To study the 3D effect, we consider dynamic rupture in specimens of different plate thickness. Figure 3.4 compares two representative experiments conducted under the same experimental conditions but with plates of different thickness: 10 mm in Figure 3.4a and 5 mm in Figure 3.4b. Overall, the two experiments result in similar dynamic ruptures. In both cases, the peak slip velocity is around 8 m/s, there is no rupture arrest within the time window of observation, and the rupture is in the process of transitioning to supershear speeds. One notable difference is in periods of velocity oscillations that are superimposed on the overall rupture profile. These periods are about twice smaller for

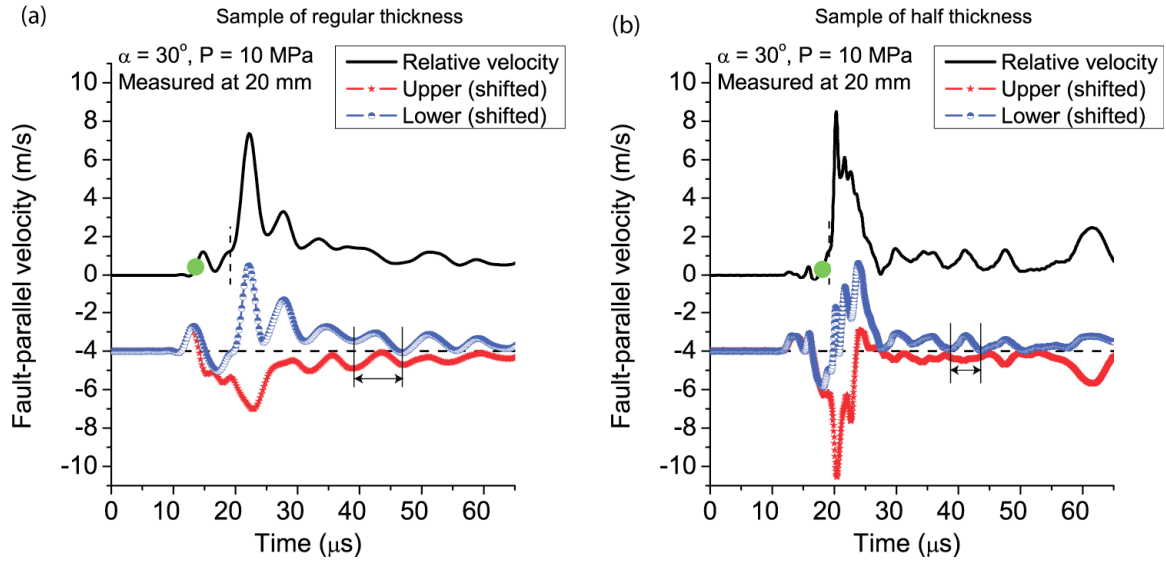


Figure 3.4: Comparison of fault-parallel velocity measurements between (a) a regular sample and (b) a twice thinner sample. For both cases, the inclination angle is $\alpha = 20^\circ$, the compressive load is $P = 10$ MPa, and the measurement location is 20 mm. The wavelengths of oscillations in the slip velocity profile becomes twice smaller for the twice thinner samples, indicating that the oscillations are at least partially due to the 3D effect.

the twice thinner specimen, as illustrated in Figure 3.4 by marking one period of the oscillations in the tail of the rupture profile. Note that the period of oscillations changes with time, being shorter at the rupture front and decreasing further along the rupture profile.

Hence the 3D effect does not change the main characteristics of dynamic ruptures but it does cause at least some of the observed oscillations in the measured particle velocity.

This is likely due to waves bouncing between the lateral free surfaces. One consequence of this finding is that the 3D effect needs to be removed from the measured velocity profiles before the profiles can be quantitatively compared with results of 2D modeling. Note that the contribution of the 3D effect to the upper and lower measurements is not exactly symmetric, as the computed relative velocity retains some oscillations. The lack of symmetry for the 3D effect is likely due to the combination of the following factors: (i) the wire is embedded in a semi-circular hole in the lower half of the plate, potentially creating some asymmetry in the radiated wave fields, (ii) in most experiments, a small tensile crack is created in the lower half of the plate after the explosion, and (iii) the measurements are sensitive to small differences in the alignment of the laser beams of the two velocimeters and in the position of the laser beams with respect to the interface.

The 3D effect could be partially responsible for deviations from anti-symmetric sliding observed in our experiments. In 2D in-plane shear problems, the fault-parallel particle velocities are expected to be anti-symmetric. Our experiments exhibit deviations from anti-symmetry for locations close to the nucleation region. Figure 3.5 shows velocity measurements at 20 mm and 40 mm from the hypocenter. The measurements were made during two experiments with the same experimental conditions. At the distance of 20 mm (Figure 3.5a), the lower and upper traces have opposite signs for most of the time but they are not exactly anti-symmetric; for example, the lower measurement (blue line) has higher peak velocity than the upper measurement. When each of the two measurements

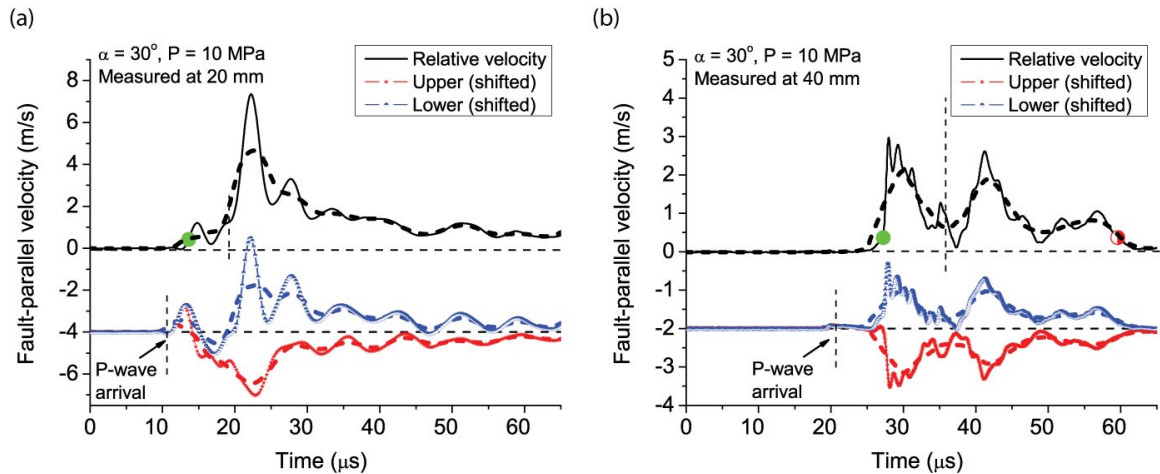


Figure 3.5: Evaluation of deviations from anti-symmetry of the fault-parallel velocity on the two sides of the interface measured at (a) 20 mm and (b) 40 mm from the nucleation region. For both measurements, $\alpha = 30^\circ$ and $P = 10$ MPa. Dashed lines are smoothed velocity profiles that are constructed by averaging the measurement within the window of $5 \mu\text{s}$, in an attempt to approximately remove the 3D effect. Deviations from asymmetry in the upper and lower measurements are present at 20 mm but virtually disappear at 40 mm. Smoothing the velocity profiles decreases the asymmetry, indicating that it is partially due to the 3D effect.

is averaged using a $5 \mu\text{s}$ time window, to partially remove the effect of the oscillations, the deviation from anti-symmetry becomes less pronounced (dashed lines in Figure 3.5a), indicating that oscillations due to the 3D effect are at least a contributing factor. Another factor that could contribute to breaking the anti-symmetry is the wire explosion and, in particular, the potential Mode I component that it could create at the measurement location. Our measurements of fault-normal particle velocities (section 3.6.1) show that rela-

tive fault-normal motion is rather small and within the measurement error. Note that deviations from anti-symmetry virtually disappear for the measurements farther along the interface, at 40 mm from the hypocenter (Figure 3.5b), as would be consistent with the decaying influence of either the 3D nature of the initial rupture propagation or the nucleation procedure away from the hypocenter.

3.4 Experimental observations of systematic variation from pulse-like to crack-like rupture modes

We use the experimental methodology described in Sections 3.2-3.3 to study the effect of prestress on rupture mode. A series of experiments has been conducted with the inclination angle α ranging from 20° to 30° and the compressive load P varying from 10 MPa to 30 MPa. Larger values of inclination angle α result in higher levels of nondimensional shear prestress $f_0 = \tau_0 / \sigma_0 = \tan \alpha$. Larger values of far-field compression P result in higher absolute levels of stress.

3.4.1 Variation of rupture mode with nondimensional shear prestress

We find that rupture mode varies from pulse-like to crack-like as the inclination angle α and hence the nondimensional shear prestress $f_0 = \tau_0 / \sigma_0 = \tan \alpha$ are increased. This

systematic variation is shown in Figure 3.6 using relative fault-parallel velocity measurements for three inclination angles of 20° , 25° , and 30° . Panels (a)-(c) correspond to the compressive load $P = 14$ MPa. The results for $P = 10$ MPa are reproduced in panels (d)-(f) for comparison. Relative fault-parallel displacements for both compressive loads, obtained by numerical integration of the velocity profiles, are given in panels (g)-(i). In all panels, rupture initiation and interface locking are marked by green and red dots, respectively, using the criteria described in section 3.3.2.

For both values of P and for smaller inclination angles $\alpha = 20^\circ$ and $\alpha = 25^\circ$, the resulting ruptures experience interface locking within the observation window. We call such ruptures pulse-like. The rupture duration, or the pulse width, increases with the inclination angle, being about $15 \mu\text{s}$ in the cases with $\alpha = 20^\circ$ (Figures 3.6a, 3.6d) and about $35 \mu\text{s}$ (for the more conservative locking criterion) in the cases with $\alpha = 25^\circ$ (Figures 3.6b, 3.6e). The inclination angle of $\alpha = 30^\circ$ results in crack-like ruptures, in the sense that there is no interface locking within the time of observation (Figures 3.6c, 3.6f). The difference between rupture durations, or rise times, for the three inclination angles can be further visualized through the plots of the relative fault-parallel displacement (Figures 3.6g-3.6i). The plots also show that crack-like modes lead to larger relative displacements; note that the vertical scale is different in Figures 3.6g-3.6i.

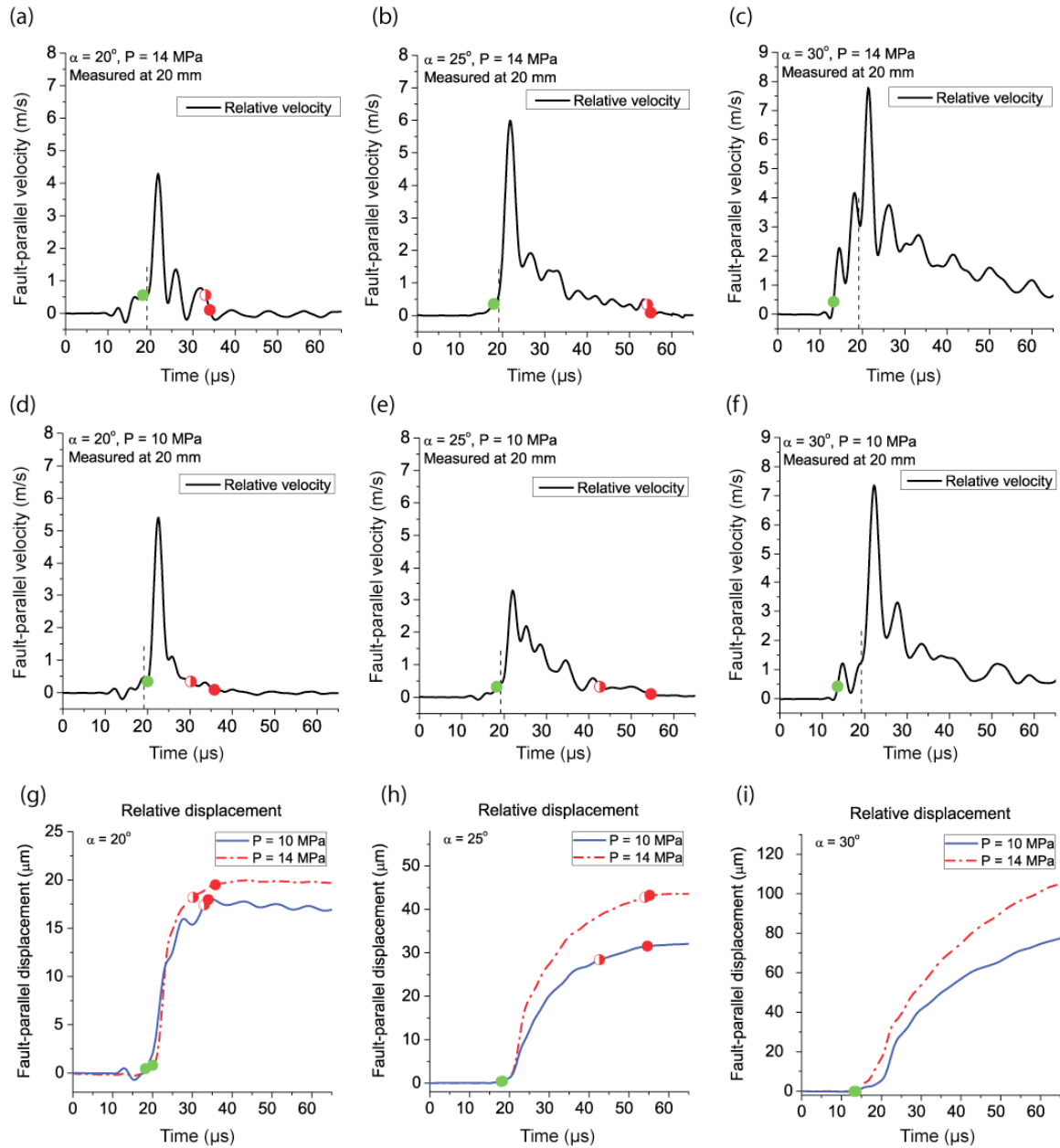


Figure 3.6: Variation of rupture mode with the inclination angle α and hence with the nondimensional shear prestress, illustrated using $\alpha = 20^\circ$ (left column), $\alpha = 25^\circ$ (middle column), and $\alpha = 30^\circ$ (right column) for two values of the compressive load, $P = 14$ MPa (top row) and $P = 10$ MPa (middle row). Panels in the bottom row show the relative displacement profiles for two compressive loads. As α increases from 20° , to 25° , and then to 30° , the rupture mode varies from a narrower pulse-like, to a wider pulse-

like, and then to a fully crack-like mode. Green and red dots indicate rupture initiation and locking times (section 3.3.2).

3.4.2 Variation of rupture mode with the compressive load

The experimentally observed variation of rupture mode with nondimensional shear prestress described in section 3.4.1 is qualitatively consistent with theoretical predictions of rupture modes on velocity-weakening interfaces (section 3.5). Another prediction of those theories is that the rupture mode would depend on the compressive load P , with larger values of P leading to more crack-like ruptures (section 3.5). A hint of such dependence is already present in the results for $P = 10$ MPa and $P = 14$ MPa presented in section 3.4.1, as ruptures for the larger compression of 14 MPa have slightly longer durations. However, the differences are within experimental variability and cannot be conclusively attributed to larger values of P .

By considering a wider range of compressive loads P , we indeed find that the rupture mode systematically varies from pulse-like to crack-like with increasing P . Note that the experiments with the larger values of P have been conducted specifically to verify the suggestion of Lu et al. (2007) that such dependence might exist, which they made based on their comparison of the initial set of experiments with the analysis of Zheng and Rice (1998). Figure 3.7 illustrates the dependence of the rupture mode on P for two values of

the inclination angle, $\alpha = 25^\circ$ (top row, $f_0 = 0.47$) and $\alpha = 27.5^\circ$ (bottom row, $f_0 = 0.52$). For both angles, the rupture varies from a narrower pulse, to a wider pulse, to the crack-like mode, as the value of P is increased from 10 MPa to 30 MPa (top row) and from 22 MPa to 30 MPa (bottom row). The measurements presented in Figure 3.7 are done at the distance of 40 mm from the hypocenter. Figure 3.7 also shows that five out of the six presented cases have supershear speeds at this location, as evidenced by the rupture front arriving earlier than the shear wave front marked by the vertical dashed line. The supershear transition and propagation are discussed in sections 3.7 and 3.8.

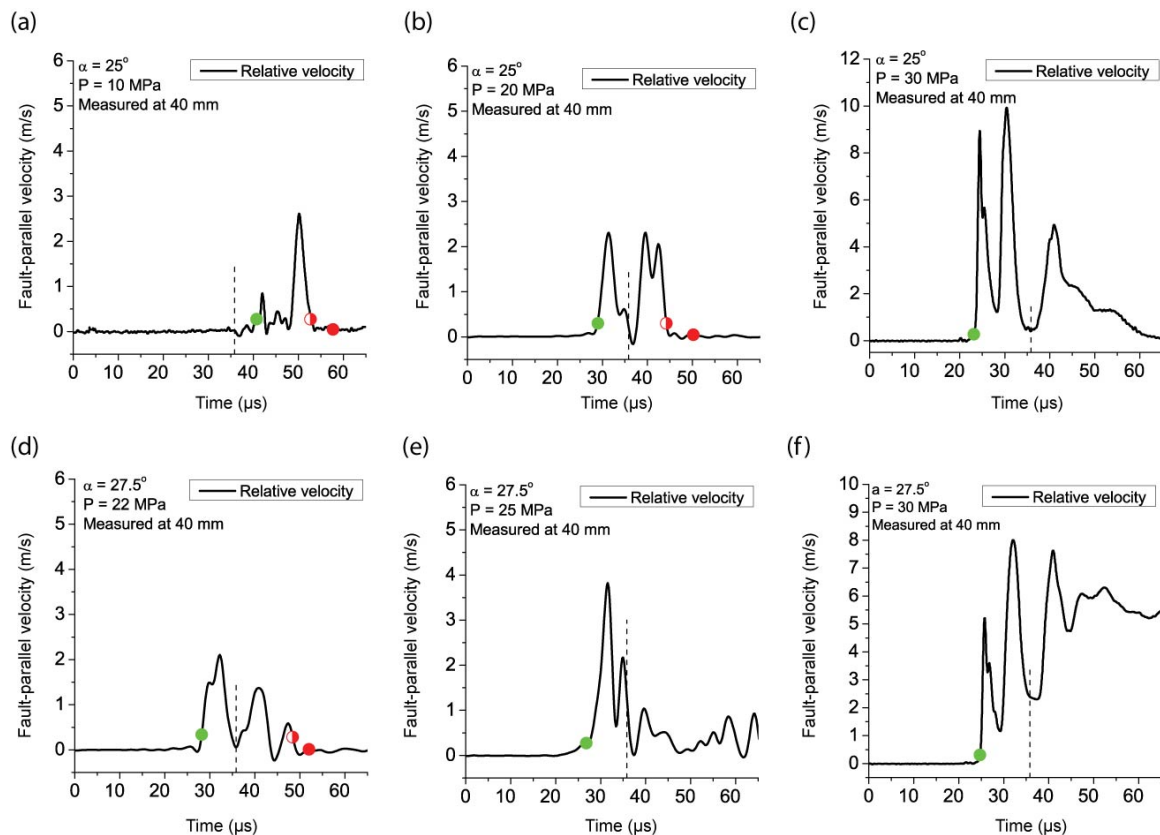


Figure 3.7: Variation of rupture mode with the compressive load P for $\alpha = 25^\circ$ (top row) and $\alpha = 27.5^\circ$ (bottom row). Velocity histories are measured at the distance of 40 mm

from the nucleation site. For both inclination angles, the rupture changes from pulse-like to crack-like as P is increased.

3.4.3 Collective analysis of rupture duration

The experimentally observed rupture durations for a number of experiments with different inclination angles α and compressive loads P are summarized in Figure 3.8. In the Figure, rupture duration for each experiment is normalized by the maximum potential sliding time, which is equal to the time window of observation minus the arrival time of the rupture front at the measurement location. This normalized rupture duration ranges from 0 (no sliding at the measurement location) to 1 (continuing sliding from the rupture arrival to the end of the observation). Crack-like ruptures correspond to the normalized rupture duration of 1, with smaller values indicating pulse-like ruptures of progressively shorter duration. For each experiment, the ends of the interval correspond to two estimates of the rupture duration, with a filled dot giving the average value. Figures 3.8a and 3.8b show rupture durations measured at 20 mm and 40 mm from the hypocenter, respectively. Angles below $\alpha = 20^\circ$ were not studied, but those experiments would have likely produced dying pulses or no sliding at the measurement location. For angles larger than $\alpha = 30^\circ$, prestress f_0 would exceed the static friction coefficient of 0.6, which would cause the sliding to occur over the entire interface at once.

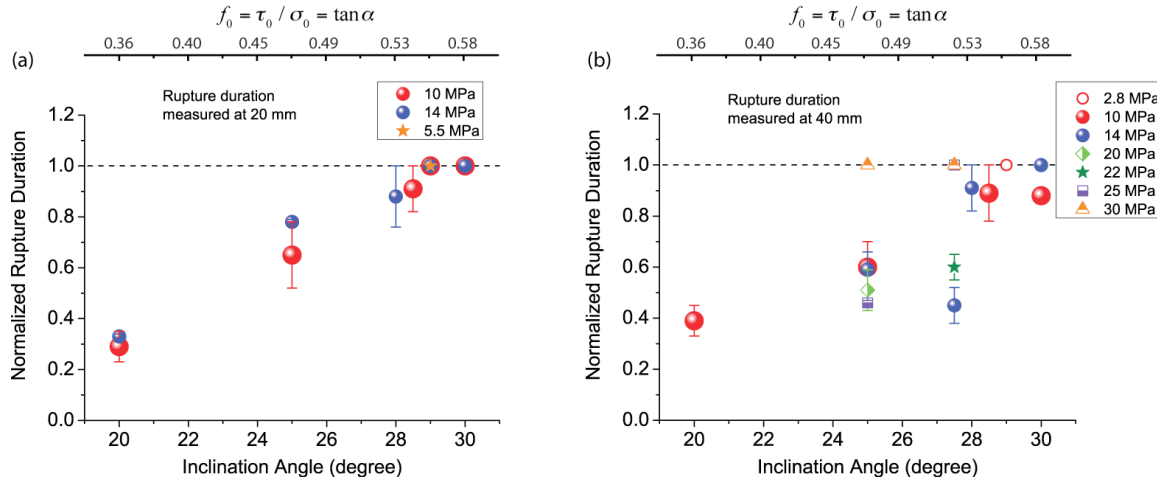


Figure 3.8: Collective analysis of rupture duration for different inclination angles and compressive loads measured at the distance of (a) 20 mm and (b) 40 mm. Rupture duration is normalized by the total possible sliding time at the location, which is equal to the time window of observation minus the rupture arrival time. The normalized duration of 1 corresponds to crack-like ruptures and smaller values correspond to progressively narrower pulse-like ruptures.

The collection of measurements in Figure 3.8 clearly shows that the inclination angle α , and hence the nondimensional shear prestress $f_0 = \tau_0 / \sigma_0 = \tan \alpha$, is the dominant factor in determining the rupture duration and hence rupture mode, with smaller angles and hence lower nondimensional shear prestress favoring pulse-like ruptures of shorter duration. Note that for the inclination angle of $\alpha = 28^\circ$, the more conservative estimate of rupture duration gives the normalized rupture duration of 1, indicating that those ruptures may be fully crack-like. For angles $\alpha = 29^\circ$ and $\alpha = 30^\circ$, the ruptures are clearly crack-

like. Lower angles produce pulse-like ruptures for most values of P . For the wider range of compressive loads P explored at some angles (e.g., $\alpha = 25^\circ$ in Figure 3.8b), the dependence of rupture duration and hence rupture mode on P is also clearly visible.

3.5 Qualitative agreement between the experimentally observed rupture modes and theoretical predictions based on velocity-weakening friction

The systematic variation of rupture modes from pulse-like to crack-like presented in section 3.4 is qualitatively consistent with the theoretical study of velocity-weakening interfaces by Zheng and Rice (1998). The study developed a way of predicting whether the rupture would propagate in a pulse-like or crack-like mode on an interface which is governed by velocity-weakening friction $\tau_{ss}(V)$ and prestressed with shear stress τ_0 . Consider 2D elastodynamic equations expressed as an integral relationship between the shear stress $\tau(x, t)$ and slip on the interface, in the form (Perrin et al., 1995; Zheng and Rice, 1998):

$$\tau(x, t) = \tau_0 + \varphi(x, t) - \frac{\mu}{2c_s} V(x, t), \quad (3.2)$$

where $\varphi(x, t)$ is the functional of slip history on the interface and $V(x, t)$ is the sliding velocity. For uniform sliding along the entire interface, $\varphi = 0$. Following Zheng and Rice (1998), let us define τ_{pulse} as the maximum value of prestress τ_0 that satisfies $\tau_0 - \mu V / (2c_s) \leq \tau_{ss}(V)$ for all $V \geq 0$. Zheng and Rice (1998) proved that no crack-like

solutions exists if $\tau_0 < \tau_{pulse}$, and hence such values of τ_0 have to correspond to either pulse-like solutions or no rupture. For larger values of τ_0 , their study defined parameter T that can be used to predict the rupture mode. Let us denote by V_{dyna} the larger of the two possible solutions of the equation $\tau_0 - \mu V / (2c_s) = \tau_{ss}(V)$. Then

$$T = \frac{d\tau_{ss}/dV}{d\tau_{el}/dV} \Big|_{V=V_{dyna}}, \quad (3.3)$$

where $\tau_{el} = \tau_0 - \mu V / (2c_s)$. That is, parameter T is the ratio of the slopes of the steady-state friction curve τ_{ss} and the elastodynamic stress τ_{el} evaluated at their intersection $V = V_{dyna}$. When T exists, it is a non-dimensional scalar between zero and one. If T is close to zero, the rupture mode is crack-like. If T is close to one, the rupture mode is pulse-like. If T does not exist (which occurs for $\tau_0 < \tau_{pulse}$), the rupture mode is either pulse-like or there is no rupture propagation.

To apply the analysis of Zheng and Rice (1998) to our experiments, let us describe the frictional properties of the interface by Dieterich-Ruina rate-and-state friction law enhanced with additional velocity weakening at high slip velocities, as appropriate for flash heating. For steady-state sliding, the friction law reduces to

$$\tau_{ss}(V) = \sigma \left(f_w + \frac{f_* + (a-b) \ln(V/V_*) - f_w}{1 + V/V_w} \right), \quad (3.4)$$

where f_* and V_* are the reference friction coefficient and slip velocity, respectively, a and b are rate-and-state friction coefficients, V_w is the characteristic slip velocity for flash heating, and f_w is the residual friction coefficient at high sliding rates. Based on pre-

liminary low-velocity friction measurements for Homalite interfaces (collaboration with B. Kilgore, N. Beeler, and C. Marone), we use the following values: $f_* = 0.6$, $V_* = 1 \times 10^{-6}$ m/s, and $b - a = 0.005$. Since there are no high-velocity friction measurements for Homalite, the values of f_w and V_w have to be selected based on indirect inferences from previous studies and the flash-heating theory (Rice, 2006). Lu et al. (2008) showed, through numerical simulations of dynamic ruptures on slip-weakening interfaces, that supershear transition distances experimentally determined by Xia et al. (2004) can be matched by models with a range of dynamic friction coefficients, if suitable modifications in other parameters are assumed. Lu et al. (2008) used dynamic friction coefficients 0.2 and 0.34 as examples. Based on the values of other parameters needed to fit the transition distances, Lu et al. (2008) argued that 0.2 and 0.34 may represent lower and upper bound of the actual dynamic friction coefficient. The residual friction coefficient f_w in the velocity-dependent friction description used in this study is analogous to the dynamic friction coefficient of linear slip-weakening friction used in Lu et al. (2008), and so we consider values of $f_w = 0.2$ and $f_w = 0.34$ here. The application of the flash-heating theory of Rice (2006) to Homalite results in the range of 0.2 m/s to 2 m/s for the characteristic flash-heating velocity V_w , assuming plausible ranges for inputs. We use the following two sets of parameters to illustrate the predictions of Zheng-Rice theory: $f_w = 0.2$, $V_w = 1.4$ m/s (Figure 3.9a, Table 3.1a) and $f_w = 0.34$, $V_w = 0.5$ m/s (Figure 9b, Table 3.1b). We continue to assume that normal stress σ is approximately equal to the initial normal stress σ_0 at the location where we interpret the rupture mode. The basis for this assumption is discussed in section 3.6.1.

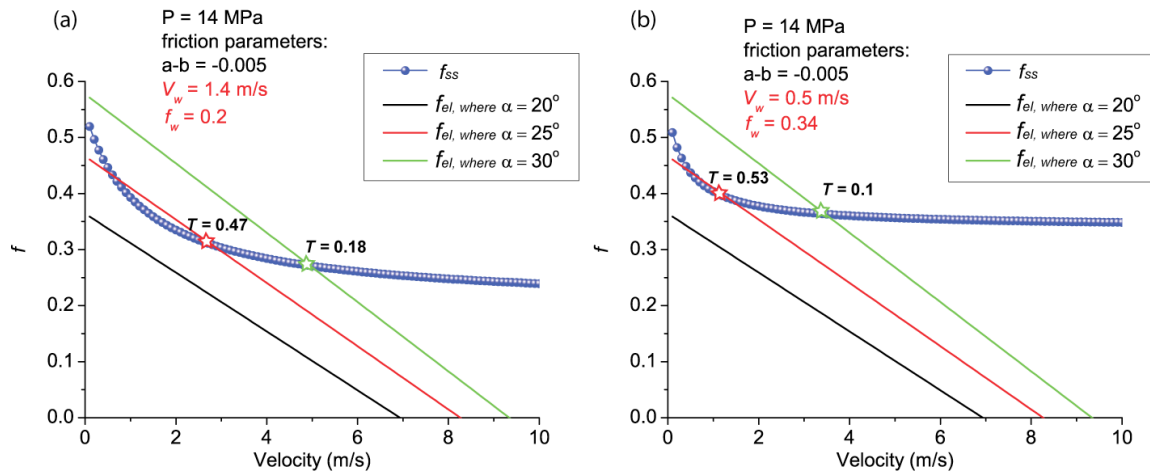


Figure 3.9: Illustration of the definition of theoretical parameters τ_{pulse} and T used to predict rupture mode in our analysis, based on the study of Zheng and Rice (1998), for two sets of velocity-weakening parameters: (a) $f_w = 0.2$, $V_w = 1.4$ m/s and (b) $f_w = 0.34$ and $V_w = 0.5$ m/s. The dependence of the steady-state friction coefficient on sliding velocity is shown as a dotted blue line. The (straight) lines of the normalized elastodynamic stress $f_{el}(V) = \tau_{el}(V) / \sigma$ are also plotted, for three different inclination angles. $\alpha = 20^\circ$ corresponds to the shear prestress level lower than τ_{pulse} and parameter T is not defined in that case. Higher angles of 25° and 30° result in the lines of elastodynamic stress intersecting the lines of steady-state friction, with the corresponding values of parameter T given in the Figure.

Figure 9 illustrates the elastodynamic stress $\tau_{el} = \tau_0 - \mu V / (2c_s)$ and the steady-state friction dependence $\tau_{ss}(V)$, the comparison of which is used to define the mode-predicting parameters τ_{pulse} and T as described above. The normalized steady-state friction

$$f_{ss}(V) = \tau_{ss}(V) / \sigma = f_w + \frac{f_* + (a-b) \ln(V/V_*) - f_w}{1 + V/V_w} \quad (3.4)$$

and the normalized elastodynamic stress

$$f_{el}(V) = \tau_{el}(V) / \sigma = \tan \alpha - \frac{\mu}{2c_s} \frac{V}{P \cos^2 \alpha} \quad (3.5)$$

are plotted. From the last expression, we see that both experimental parameters, α and P , affect $f_{el}(V)$ and hence the values of τ_{pulse} and T . In both panels of Figure 3.9, $P = 14$ MPa and three representative case with the inclination angles of 20° , 25° , and 30° are considered. $f_w = 0.2$, $V_w = 1.4$ m/s and $f_w = 0.34$, $V_w = 0.5$ m/s are adopted in Figures 3.9a and 3.9b, respectively. Both panels illustrate the same qualitative features. For $\alpha = 20^\circ$, the elastodynamic stress (black line) is below the steady-state friction (blue dotted line) for all $V \geq 0$ and no intersection exists between the two curves. According to the analysis of Zheng and Rice (1998), in this case the rupture would either proceed in a pulse-like mode or not at all, i.e. the rupture would arrest. This is consistent with our experimental results that indicate pulse-like ruptures for all cases with $\alpha = 20^\circ$ that have been studied (Figure 3.6). As the inclination angle increases, the nondimensional prestress grows, and the elastodynamic stress lines move up; their intersection with the friction curve defines the nondimensional parameter T which varies from $T = 1$ when the two lines touch to values approaching zero for intersections at higher values of V . The trend

indicates that rupture mode should become crack-like for larger inclination angles, as observed in our experiments.

(a)

P \ α	20°	21°	22°	23°	24°	25°	26°	27°	28°	29°	30°
30 MPa		0.63	0.38	0.28	0.22	0.18	0.15	0.13	0.11	0.10	0.09
26 MPa			0.49	0.34	0.26	0.21	0.18	0.15	0.13	0.12	0.10
22 MPa			0.81	0.45	0.33	0.26	0.21	0.18	0.16	0.14	0.12
18 MPa				0.7	0.44	0.33	0.27	0.22	0.19	0.17	0.15
14 MPa					0.76	0.47	0.36	0.29	0.25	0.21	0.18
10 MPa							0.58	0.43	0.35	0.29	0.25
6 MPa									0.60	0.46	0.38
2 MPa										0.84	0.50

Color	Predicted mode
	Pulse-like or no rupture
	Crack-like

Friction parameters:
 $(a - b) = -0.005$
 $f_* = 0.6, f_w = 0.2, V_w = 1.4 \text{ m/s}$

(b)

P \ α	20°	21°	22°	23°	24°	25°	26°	27°	28°	29°	30°
30 MPa					0.29	0.18	0.12	0.09	0.07	0.06	0.05
26 MPa					0.37	0.21	0.14	0.1	0.08	0.07	0.05
22 MPa					0.5	0.26	0.17	0.13	0.09	0.08	0.06
18 MPa						0.34	0.22	0.16	0.12	0.09	0.08
14 MPa						0.53	0.3	0.2	0.15	0.12	0.1
10 MPa							0.48	0.3	0.22	0.17	0.14
6 MPa								0.62	0.38	0.28	0.22
2 MPa										0.68	0.45

Color	Predicted mode
	Pulse-like or no rupture
	Crack-like

Friction parameters:
 $(a - b) = -0.005$
 $f_* = 0.6, f_w = 0.34, V_w = 0.5 \text{ m/s}$

Table 3.1: Values of the mode-predicting parameter T for the ranges of inclination angles and compressive loads explored in our experiments, computed using (a) $f_w = 0.2$, $V_w = 1.4$ m/s and (b) $f_w = 0.34$ and $V_w = 0.5$ m/s. Other friction parameters are specified in the text. Values of T close to 0 predict crack-like modes, while values close to 1 predict pulse-like modes. Empty cells correspond to experimental conditions for which parameter T is not defined, predicting either a pulse-like rupture or no rupture. The region $T < 0.3$ is shown in orange, to qualitatively indicate the experimental parameter space that is predicted to correspond to crack-like ruptures. The critical value of 0.3 is chosen based on simulations of Zheng and Rice (1998).

To compare the predictions of Zheng and Rice (1998) with the results of our experiments for all experimental parameters, we compute the values of parameter T for P from 2 MPa to 30 MPa and for α from 20° to 30° (Tables 3.1a and 3.1b). For a fixed value of P , e.g. $P = 14$ MPa, parameter T decreases from values close to 1 to values close to zero as the inclination angle α increases, predicting variation from pulse-like to crack-like rupture modes; empty cells of the table correspond to parameter regimes in which parameter T does not exist, which predicts that the rupture is either a pulse or there is no rupture. This is consistent with experimentally observed variation of rupture mode with the inclination angle α (section 3.4.1). For a fixed value of α , e.g. $\alpha = 25^\circ$, parameter T again decreases from values close to 1 to values close to zero as the compressive load P increases, predicting variation from pulse-like to crack-like modes. This is consistent with the experimentally observed variation of rupture mode with the compressive load P .

Overall, higher values of either α or P favor crack-like rupture in experiments as well as in the theoretical prediction; the corresponding cells of the table are marked with orange, using $T = 0.3$ as the cut-off value based on the numerical study of Zheng and Rice (1998). Hence we find that the systematic variation of rupture modes observed in the experiments is qualitatively consistent with theories based on velocity-weakening friction.

3.6 Effect of nucleation procedure

The comparison between experimental results and velocity-weakening theories in section 5 assumes that fault-normal stress is not altered outside the nucleation region. The rupture initiation procedure reduces normal stress locally in the nucleation region, and that effect can propagate along the interface, creating lower friction resistance and potentially providing an alternative explanation for the variation in rupture modes. In this section, we study this and other potential effects of the nucleation procedure.

3.6.1 Measurements of fault-normal motion

To assess whether there are notable changes in fault-normal stress σ outside the nucleation region, we have conducted several experiments in which the fault-normal particle velocity histories above and below the interface were measured at the same location (20 mm) and with a similar setup as for the fault-parallel velocity measurements. The con-

figuration of the measurements is illustrated in Figure 3.10. Two reflective membranes are positioned 20 mm away from the hypocenter. Laser velocimeters are focused on two membrane edges separated by the distance of 0.5 mm. The difference between the two fault-normal measurements would indicate changes in the fault-normal stress. Negative values of relative velocity would indicate that the two measurement locations are moving closer together and hence correspond to increase in fault-normal compressive stress σ ; positive values would correspond to decrease of the fault-normal compression. Because the experiments are designed to induce in-plane shear rupture, fault-normal measurements are expected to be much smaller than the fault-parallel ones. This reality requires much higher accuracy of the alignment of the laser beams. Other factors may affect the measurement, such as potential slight non-planarity of membrane surfaces and its effect due to relative sliding motion of the two measurement locations.

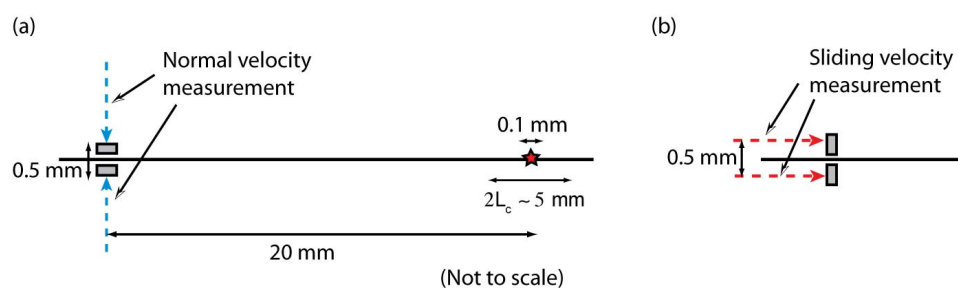


Figure 3.10: Schematic illustration of the experimental setup for fault-normal velocity measurements. Two measurement locations are separated by 500 μm . Note that the exploding wire is 100 μm in diameter and the distance between the wire and the measurements location is 20 mm. Any wave radiated from the nucleation site will continuously decay as it propagates.

We present fault-normal measurements for two experiments conducted with the inclination angles of 20° and 30° (Figure 3.11), which are the lowest and highest inclination angles used in experiments. The individual velocity measurements above and below the interface generally coincide (Figures 3.11a, 3.11b), showing that the two points move together for the entire duration of the experiment. This suggests that there are no significant changes in the fault-normal stress. To quantify the small differences between fault-normal velocities above and below the interface, we compute the relative fault-normal velocity (Figures 3.11c, 3.11d) as well as the relative fault-normal displacement (Figures 3.11e, 3.11f). The relative normal measurements are about two orders of magnitude smaller than the fault-parallel measurements (Figures 3.6, 3.7), as expected. To emphasize this discrepancy, the ranges of the y-axes in Figure 3.11 are comparable to the ranges of the fault-parallel measurements. The insets in panels (c)-(f) show the relative normal velocities and displacements in more detail, for the time period that starts with the approximate P-wave arrival time of $10 \mu\text{s}$ and includes the period of the most active sliding between $20 \mu\text{s}$ and $30 \mu\text{s}$. We see that, for both angles, the two measurement points get closer between $10 \mu\text{s}$ and $30 \mu\text{s}$, by about $0.1 \mu\text{m}$ for $\alpha = 20^\circ$ and $0.3 \mu\text{m}$ for $\alpha = 30^\circ$. This indicates an increase of compression across the interface.

Hence the fault-normal measurements reveal no reduction of normal stress during sliding; on the contrary, they point to larger compression. This means that the observed ruptures are not driven by normal stress reduction propagating along the interface from the nucleation region. In the case of $\alpha = 20^\circ$, the sliding stops at about 30 to $35 \mu\text{s}$ (Figure 3.6a);

the relative normal velocity and displacement histories show nothing special occurring during those times; in fact, the variations in fault-normal quantities are minimal in that time interval. Hence the arrest of sliding for $\alpha = 20^\circ$ is likely caused by variations of the friction coefficient due to velocity-weakening friction, as advocated in section 3.5, and not by normal stress changes.

We caution that these conclusions would require further verification, as the fault-normal relative displacements of 0.1 to 0.3 μs are quite small and may be testing the limits of our resolution. While relative fault-normal velocity measurements are largest during the time interval of most active slip, from 20 μs to 30 μs , they do not exhibit a coherent change for that time period but rather have an oscillatory nature. One would expect the largest measurement errors to come when the membranes, which serve as focusing locations for the laser beams, are moving. The motion may affect the accuracy of the velocimeters, and it may lead to the measurement reflecting the roughness of the membrane surfaces rather than any fault-normal motion. However, the consistent increase of compression that we observe in the presented measurements and in several other experiments suggests that decrease in the fault-normal compression during sliding is unlikely.

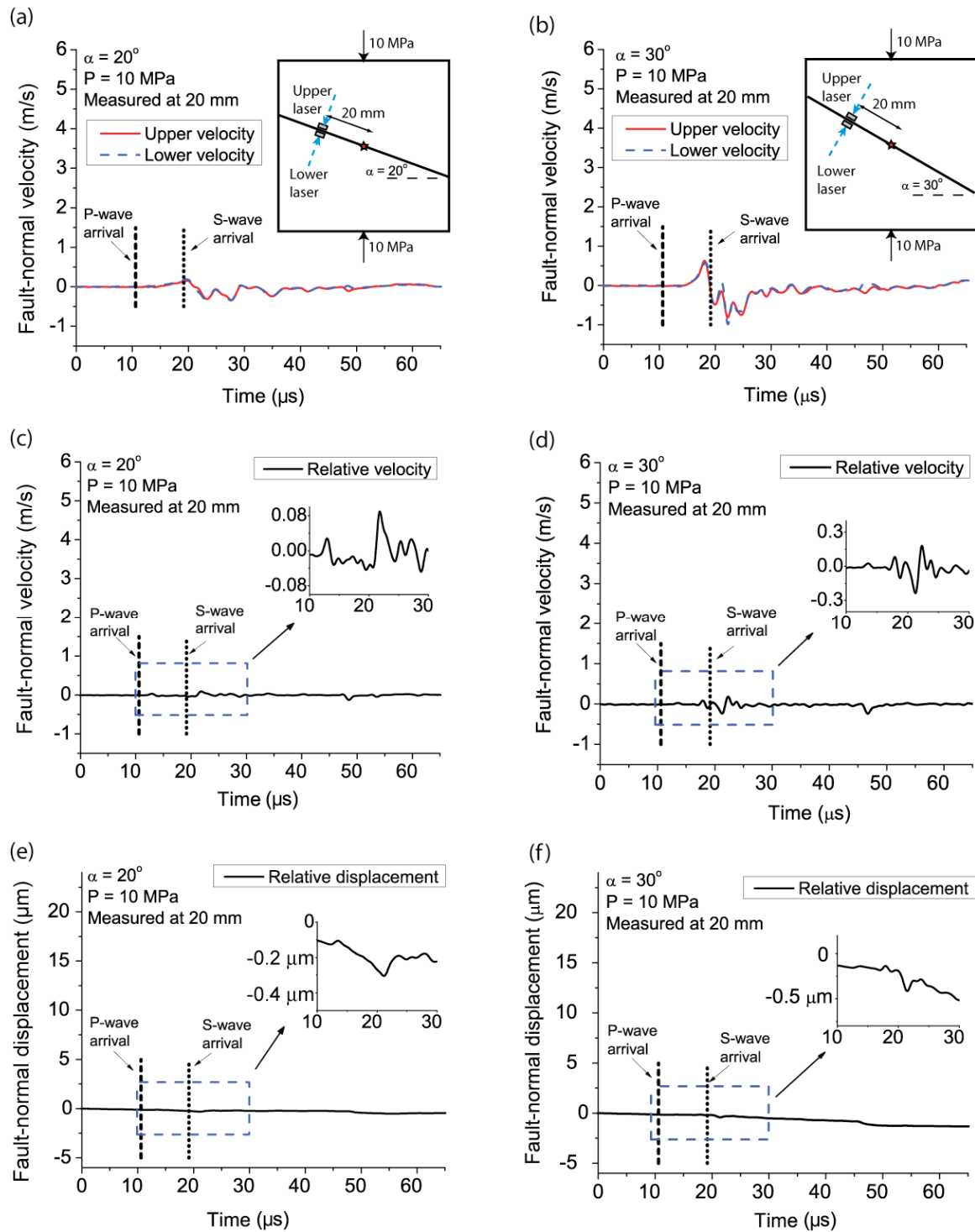


Figure 3.11: Fault-normal measurements at the distance of 20 mm for the experiments with $\alpha = 20^\circ$ (left column) and $\alpha = 30^\circ$ (right column). The compressive load is $P = 10$ MPa for both cases. (a)-(b) Fault parallel velocity measurements above and be-

low the interface. (c)-(d) The relative fault-normal velocity profile. The inset gives the detailed view for the time window between 10 μs and 30 μs , during which the P-wave arrives and largest fault-parallel velocities are recorded. (e)-(f) The relative fault-normal displacement between two measurement points. Negative values correspond to more compression.

3.6.2 Influence of nucleation strength

While in section 3.6.1 we argue that normal stress reduction due to the explosion is not observed at the measurement locations, the nucleation procedure can still affect rupture propagation through other means (Festa and Violte, 2006; Shi and Ben-Zion, 2006; Liu and Lapusta, 2007; Shi and Ben-Zion, 2007; Lu et al, 2008). For example, different explosions could create different history of sliding in the initiation region, releasing a different shear wave field and starting a domino effect that may significantly alter the rupture development.

As a first step towards understanding those dependencies, here we study the effect of the explosion intensity. The results of two experiments with different charging voltage for the explosion are shown in Figure 3.12. We see that the rupture duration in the two cases is similar, and the resulting rupture is pulse-like. At the same time, the peak relative velocity is higher for the higher voltage. A possible explanation is that the stronger explo-

sion creates larger sliding velocities and hence larger fault-parallel relative displacements in the nucleation region, and the radiated waves carry this information, affecting the peak sliding velocities further along the interface. Based on these and similar experiments, we could conclude that, as long as the nucleation procedure is strong enough to trigger the rupture, the mode of the rupture would be independent of the explosion strength.

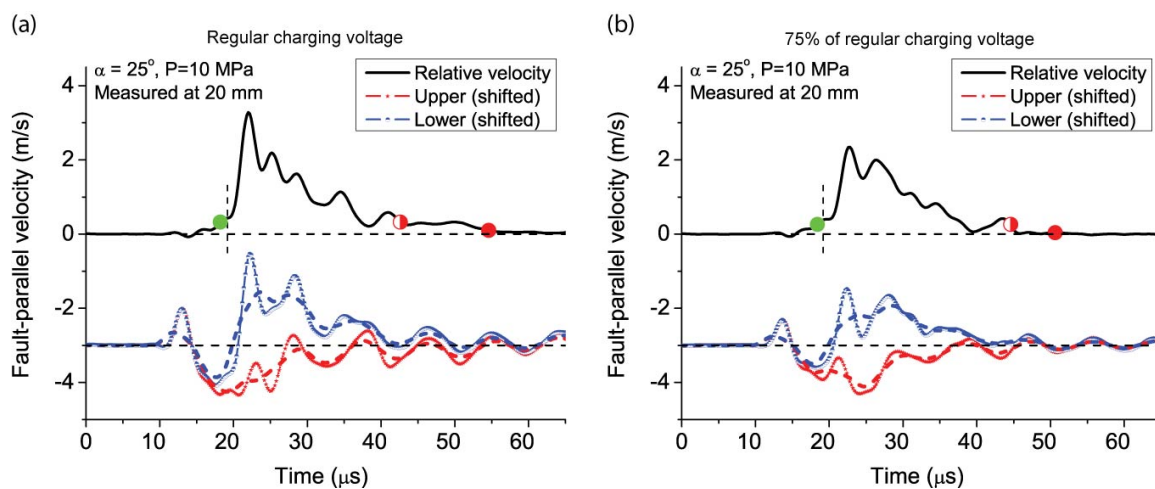


Figure 3.12: Comparison of fault-parallel velocity histories obtained with different explosion intensity, for $\alpha = 25^\circ$ and $P = 10$ MPa. (a) The capacitor bank used for the wire explosion is charged with the regular voltage of 1600 V. (b) The charging voltage is reduced to 75% of the regular value. The peak slip velocity in (b) is slightly reduced but the rupture duration is similar.

3.7 Rupture speeds of pulse-like and crack-like modes

3.7.1 Observations of supershear pulses and cracks

The experimental measurements of relative fault-parallel velocity presented in section 3.4 provide a number of examples of both supershear crack-like ruptures (Figures 3.6c, 3.6f, 3.7c, 3.7e, 3.7f) and pulse-like ruptures (Figures 3.6a, 3.7b, 3.7d). The speeds are clearly supershear in those cases as rupture arrival times (indicated by green dots) at the measurement locations are smaller than arrival times of the shear wave (indicated by vertical dashed lines). Ruptures typically transition to supershear speeds after a period of sub-Rayleigh propagation, and the distance between the location of the crack initiation and the location of supershear transition is called the transition distance (Andrews, 1976; Xia et al., 2004). The cases that result in supershear ruptures in Figures 3.6 and 3.7 have transition distances smaller than 20 mm and 40 mm, respectively, as those Figures present velocity measurements at the corresponding locations. Note that transition distances in our experiments tend to be larger than the ones reported in Xia et al. (2004). The difference can be attributed to a different surface preparation and hence different friction properties.

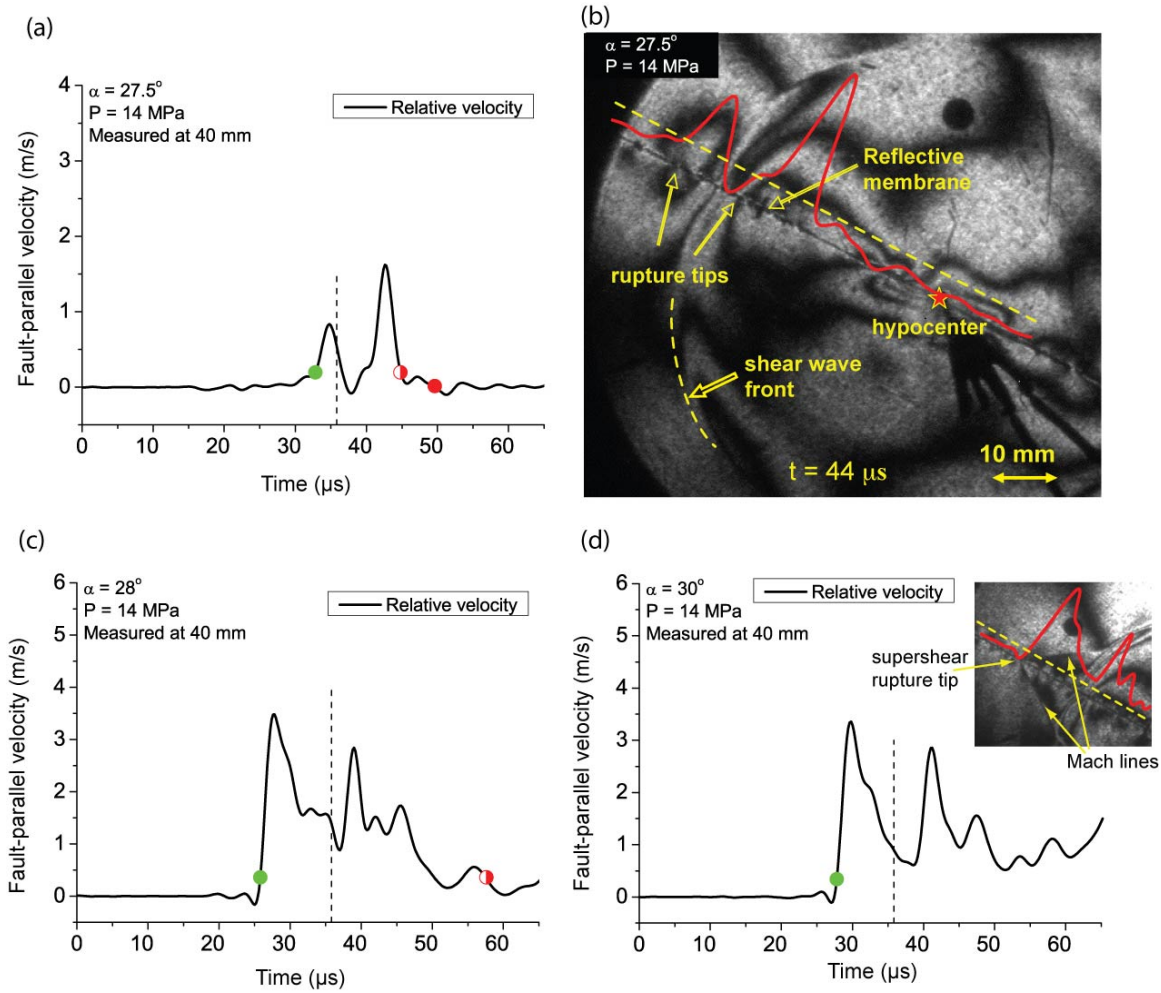


Figure 3.13: Representative cases of supershear pulse-like and crack-like ruptures. Fault-parallel relative velocity histories shown are measured at 40 mm in experiments with $P = 14 \text{ MPa}$. (a) $\alpha = 27.5^\circ$ results in a supershear pulse-like rupture. (b) Superposition of the photoelastic image captured at $44 \mu\text{s}$ and the velocity measurement from panel (a). The rupture front is clearly ahead of the circular shear wave front, a part of which is marked with a curved yellow line. (c) $\alpha = 28^\circ$ results in a crack-like rupture that has almost arrested at the end of the observation window. (d) $\alpha = 30^\circ$ produces a supershear rupture that is clearly crack-like. The inset shows a part of the corresponding photoelastic image with the resulting Mach lines.

Representative cases of supershear pulse-like and crack-like ruptures are presented in Figure 3.13 for $P = 14$ MPa and three inclination angles α of 27.5, 28, and 30 degrees. For $\alpha = 27.5^\circ$, the rupture is clearly pulse-like, with the sliding stopping within the observation window (Figure 3.13a). The slip history shown in Figure 3.13a consists of two pulses, a supershear pulse followed by a subshear pulse. Such a sliding history could be indicative of the mother-daughter transition mechanism (Burridge, 1973; Andrews, 1976), in which a supershear “daughter” rupture nucleates in front of the main sub-Rayleigh “mother” rupture. In numerical simulations of that mechanism (e.g., Lu et al., 2008), the daughter and mother rupture become connected later and propagate as a single rupture. The profile in Figure 3.13a could be interpreted as evidence for the mother-daughter transition mechanism. However, ruptures can transition to supershear speeds by direct change of speeds at the rupture tip (Liu and Lapusta, 2007; Lu et al., 2008). Numerical simulations show (Liu and Lapusta, 2007; Lu et al., 2008) that, in the case of the direct transition with no daughter crack, the supershear portion of the rupture may still look partially or fully disconnected from the rest of the rupture, similarly to the profile in Figure 3.13a. This is due to the stress changes, and hence sliding velocity changes, caused by the combination of shear waves and Rayleigh waves that are left behind the supershear rupture tip. Hence further study is needed to conclusively determine the transition mechanism in our experiments, as discussed in Lu et al. (2008).

Figure 3.13b shows the superposition of the photoelastic fringe pattern at the time of $t = 44 \mu\text{s}$ and the slip velocity measurements from Figure 3.13a reinterpreted with re-

spect to the interface locations as explained in section 3.3.1. The image contains a clear circular shear-wave front and a ring-like fringe structure with a stress concentration tip on the interface ahead of the shear wave. That stress concentration corresponds to the supershear rupture tip, as indicated by the superposition with the velocity measurements. An interesting observation is the absence of Mach lines emitted from the supershear rupture tip; such Mach lines are a common feature of supershear ruptures (Rosakis, 2002; Xia et al., 2004). The Mach lines are not formed at the special supershear rupture speed equal to $\sqrt{2}c_s$ (Rosakis, 2002). Hence the evidence for supershear propagation from the slip velocity history in Figure 3.13a and the absence of Mach lines in the photoelastic image can be reconciled if the rupture speed is $\sqrt{2}c_s$. In section 3.7.2, we show that the rupture speed in this case is indeed close to $\sqrt{2}c_s$.

According to the results in sections 3.4 and 3.5, one can obtain crack-like ruptures by increasing the inclination angle. At the same time, the ruptures would remain supershear, as larger inclination angles translate into larger nondimensional prestress which favors supershear transition (Andrews, 1976; section 3.8). This is demonstrated in Figures 3.13c and 3.13d. When the inclination angle is increased to 28 degrees, the rupture remains supershear but the sliding zone widens, producing either a wider pulse according to the locking criterion based on slip velocity or even a crack-like rupture according to the more conservative criterion based on residual slip (Figure 3.13c). The supershear rupture tip is well ahead of the shear wave, indicating that the transition distance is shorter in this case than in the case of Figure 3.13a, and/or that the rupture speed may be higher. Figure 3.13d shows the case of $\alpha = 30^\circ$, an angle which results in a supershear crack-like rupture

as judged by measurements at the location of 20 mm from the hypocenter (Figure 3.6c). At 40 mm, the rupture is still crack-like, in the sense that sliding does not arrest in the time window of observation, and the rupture speed is clearly supershear. The insert gives a photoelastic image with two clear Mach lines.

3.7.2 Evolution of rupture speeds for supershear pulses and cracks

To further analyze the supershear transition and propagation of different rupture modes, we infer the rupture speed evolution of the pulse-like and crack-like ruptures discussed in section 3.7.1. The rupture speed history is determined using the sequence of photoelastic images obtained by the high-speed camera. The tip of the rupture is identified in each image and the rupture speed is computed as the ratio of the rupture tip advance and inter-image time. The rupture speed is then averaged for three neighboring images. The location of the jump from sub-Rayleigh to supershear speeds is confirmed by the appearance of two concentration of fringes in photoelastic images, one for the supershear crack tip and the other for the remnant of the subshear crack tip. For the images that have well-developed Mach lines, the inferred supershear values of the rupture speed are corroborated by measuring the angle β that the Mach lines make with the interface and computing the rupture speed by the equation $V_r = c_s / \sin \beta$.

We find that the pulse-like rupture has a larger transition distance and smaller supershear speeds than the crack-like rupture (Figure 3.14). Both ruptures have subshear speeds initially, and then rupture speeds abruptly change to supershear speeds. The pulse-like rupture, obtained under the experimental conditions $P = 14$ MPa and $\alpha = 27.5^\circ$, has the transition distance of about 30 mm and supershear speeds close to $\sqrt{2}c_s$. The crack-like rupture, obtained under the experimental conditions $P = 14$ MPa and $\alpha = 30^\circ$, has the transition distance between 18 mm and 23 mm and supershear speeds within the interval between $\sqrt{2}c_s$ and c_p . The inferred transition distances and rupture speeds are consistent with the rupture arrival times at the location of 40 mm (Figures 3.13a, 3.13d). The pulse-like rupture arrives later at this location than the crack-like rupture, which is consistent with lower rupture speeds for the pulse-like rupture.

The inferred supershear rupture speeds are in qualitative agreement with the theoretical analysis of supershear rupture propagation on interfaces governed by velocity-weakening friction by Samudrala et al. (2002). Their asymptotic analysis determined that the interval of rupture speeds between $\sqrt{2}c_s$ and c_p corresponds to stable rupture growth and that higher interface prestress corresponds to higher rupture speeds. This is exactly what we observe in our experiments. First, both pulse-like and crack-like ruptures develop supershear speeds in the interval between $\sqrt{2}c_s$ and c_p . Second, the pulse-like rupture, which corresponds to a lower inclination angle and hence lower nondimensional shear prestress, has lower supershear rupture speeds.

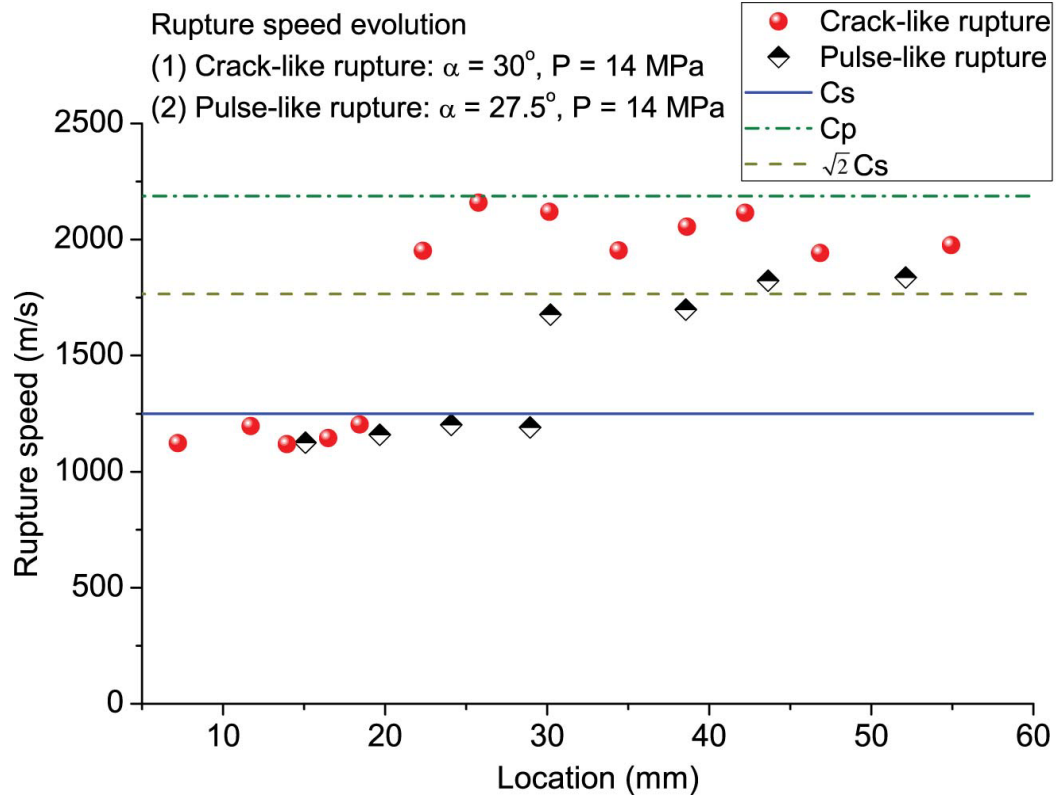


Figure 3.14: Evolution of rupture speed for a pulse-like rupture (diamonds) and a crack-like rupture (circular dots). Both ruptures have supershear speeds within the open interval between $\sqrt{2}c_s$ to c_p . The pulse-like rupture has lower supershear speeds than those of the crack-like rupture. Both observations are consistent with theories based on velocity-weakening interfaces.

3.8 Map of rupture modes and speeds under a range of experimental conditions

To summarize our findings in terms of both rupture modes and rupture speeds, we create a diagram (Figure 3.15) that indicates, for each set of experimental conditions, whether the rupture is crack-like or pulse-like, and whether its eventual propagation speed is sub-Rayleigh or supershear. For the determination of rupture mode, we use fault-parallel velocity measurements at the location of 40 mm if they are available; otherwise, we use the measurements at 20 mm. The rupture is marked as supershear if it transitions to supershear speeds within the observation domain, which extends 60 mm from the nucleation location (or 120 mm if the interface on both sides of the hypocenter is considered). Otherwise, the ruptures are marked sub-Rayleigh. This classification results in four rupture categories: supershear crack, sub-Rayleigh crack, supershear pulse, and sub-Rayleigh pulse. They are labeled by different symbols in Figure 3.15.

The diagram clearly indicates variation from pulse-like to crack-like rupture modes as the inclination angle (and hence the nondimensional shear prestress) and the compressive load are increased. The domains of pulse-like and crack-like behavior are separated by an orange dashed line. The diagram can be directly compared to Table 3.1 of theoretical predictions based on Zheng and Rice (1998) and our analysis in section 3.4. The map of the experimental results and the table of theoretical predictions are in qualitative agreement, as the upper right corner of both corresponds to crack-like ruptures, with the rest of experimental conditions corresponding to pulse-like ruptures or no rupture. The qualitative agreement between the experiments and theoretical predictions points to the importance of velocity-weakening friction, as discussed in section 3.5. Note that the boundary between the two regions has a different shape in the map of experimental results and in

the theoretically constructed table. This could be partially due to the general nature of the theoretical analysis, which ignores the influence of the initiation procedure and assumes a friction law that is plausible but not yet verified for Homalite, and partially due to viscoelastic effects in Homalite, which would create additional damping of energy and may turn what would be a crack-like mode in a purely elastic material into a pulse-like one. Some of the cases studied exhibit hints of such viscoelastic behavior. For example, in the case of $\alpha = 28^\circ$ and $P = 14$ MPa, the rupture is clearly crack-like at the location of 20 mm. However, the measurements at 40 mm (Figure 3.13c) have lower sliding velocity behind the rupture tip. Indeed, the locking criterion based on sliding velocity (section 3.3.2) indicates that interface healing occurs before the end of the observation time window. We mark this case as crack-like in Figure 3.15, as the more conservative locking criterion, the one based on residual slip, has not been met at 40 mm. The decreased vigor of the rupture between 20 and 40 mm may be due to viscoelastic effects.

Figure 3.15 shows that the majority of experiments produced supershear ruptures. We see that higher inclination angles and higher compressive loads promote supershear transition. This is consistent with prior theoretical and numerical studies (Andrews, 1976; Xia et al, 2004; Lu et al., 2008). The black dashed line that separates the supershear and sub-Rayleigh regions is generated based on the analysis of the supershear transition by Andrews (1976) and Lu et al. (2007). Andrews (1976) considered an in-plane 2D shear rupture on an interface governed by linear slip-weakening friction, in which the shear strength of the interface decreases linearly from its static value τ_s to its dynamic values τ_d over the critical slip D_c , and then remains at τ_d during subsequent sliding. Using this

model, he demonstrated that the transition distance depends only on the critical crack half length L_c and on the seismic ratio s as follows:

$$L = F(s)L_c, \quad L_c = \frac{\mu(\tau_s - \tau_d)D_c}{\pi(1-\nu)(\tau_0 - \tau_d)^2}, \quad s = \frac{\tau_s - \tau_0}{\tau_0 - \tau_d}. \quad (3.6)$$

$F(s)$ is a numerically determined function that can be approximated by $F(s) = 9.8(1.77 - s)^{-3}$ as discussed by Rosakis et al. (2007). The parameters μ and ν are the shear modulus and Poisson's ratio of the elastic solid and τ_0 is the initial shear stress acting on the interface. For the geometry of our experiment, the transition distance can be expressed as (Rosakis et al., 2007):

$$L = F(s) \frac{\mu(f_s - f_d)D_c}{\pi(1-\nu)(\sin \alpha - f_d \cos \alpha)^2 P}, \quad s = \frac{f_s - \tan \alpha}{\tan \alpha - f_d}. \quad (3.7)$$

where $f_s = \tau_s / \sigma_0$ and $f_d = \tau_d / \sigma_0$ are the static and dynamic friction coefficients, respectively. The numerical studies of Lu et al. (2007) demonstrate that the dynamic nature of the rupture initiation procedure reduces the transition distances by 30% to 40%. To plot the theoretical prediction of the separation between sub-Rayleigh and supershear ruptures in our experiments (black dashed line in Figure 3.15), we (i) use values $f_s = 0.6$, $f_d = 0.2$, and $D_c = 13 \mu\text{m}$, as these values enabled the numerical simulations of Lu et al. (2008) to match the experimentally determined transition distances of Xia et al. (2004), (ii) calculate the values of the transition distance L using the above formula for ranges of experimental parameters represented in Figure 3.15, (iii) apply the reduction factor of 33% motivated by the study of Lu et al. (2007), (iv) plot the line corresponding to transition distances of 60 mm. The size of our observation window is 60 mm in radius; and if supershear transition happens within the field of view, we consider it as supershear rup-

ture. As we can see, the resulting boundary is consistent with the experimental results. While the location of the line is not well-constrained experimentally on the sub-Rayleigh side, the line is quite successful in putting experimentally observed supershear ruptures into the same region. It also predicts the extent of the sub-Rayleigh region, which can be more fully explored in future studies.

3.9 Conclusions

By varying the inclination angle and the compressive load, we have experimentally observed pulse-like and crack-like rupture modes, and a systematic transition between them, in an experimental configuration that contains an interface prestressed both in compression and in shear, similarly to faults in the Earth's crust. Our results indicate that pulse-like ruptures can exist on such interfaces in the absence of a bimaterial effect or local heterogeneities. To the best of our knowledge, these are the first experimental observations of spontaneous pulse-like ruptures under such conditions. The systematic transition of rupture modes from pulse-like to crack-like presented in this work is qualitatively consistent with the theoretical study of velocity-weakening interfaces by Zheng and Rice (1998).

We also establish experimentally, for the first time, that both pulse-like and crack-like rupture modes can transition to supershear speeds. Indeed, we observe variation from supershear pulse-like ruptures to supershear crack-like ruptures as the inclination angle is

increased. The resulting supershear rupture speeds for the two modes are consistent with the analytical predictions of the velocity-weakening model of Samudrala et al. (2002).

The agreement between our experimental observations and models of velocity-weakening faults suggests that velocity-weakening friction plays an important role in dynamic behavior of ruptures and implies that expressing dynamic weakening of friction solely in terms of slip may not be a sufficiently general description. In the next Chapter, we confirm that linear slip-weakening friction, which is often used in single-rupture earthquake studies, fails to produce pulse-like modes in a numerical model that represents our experiments. Velocity-weakening friction, on the other hand, is capable of producing pulse-like ruptures in that model, although the particular form considered in Chapter 4 has difficulties in reproducing the full range of experimental observations.

To ensure that the sliding is not driven by fault-normal stress decrease (and the corresponding decrease in frictional resistance) propagating along the interface due to the wire explosion, we have conducted fault-normal velocity measurements. The measurements are very challenging because of the minute relative displacements involved, which are almost two orders of magnitude smaller than the fault-parallel displacements. Our results indicate that there is no fault-normal stress reduction at the measurement location. Hence the variation in rupture modes and rupture speeds that we observe cannot be caused by the nucleation-induced normal stress decrease and velocity-weakening friction remains the most viable explanation.

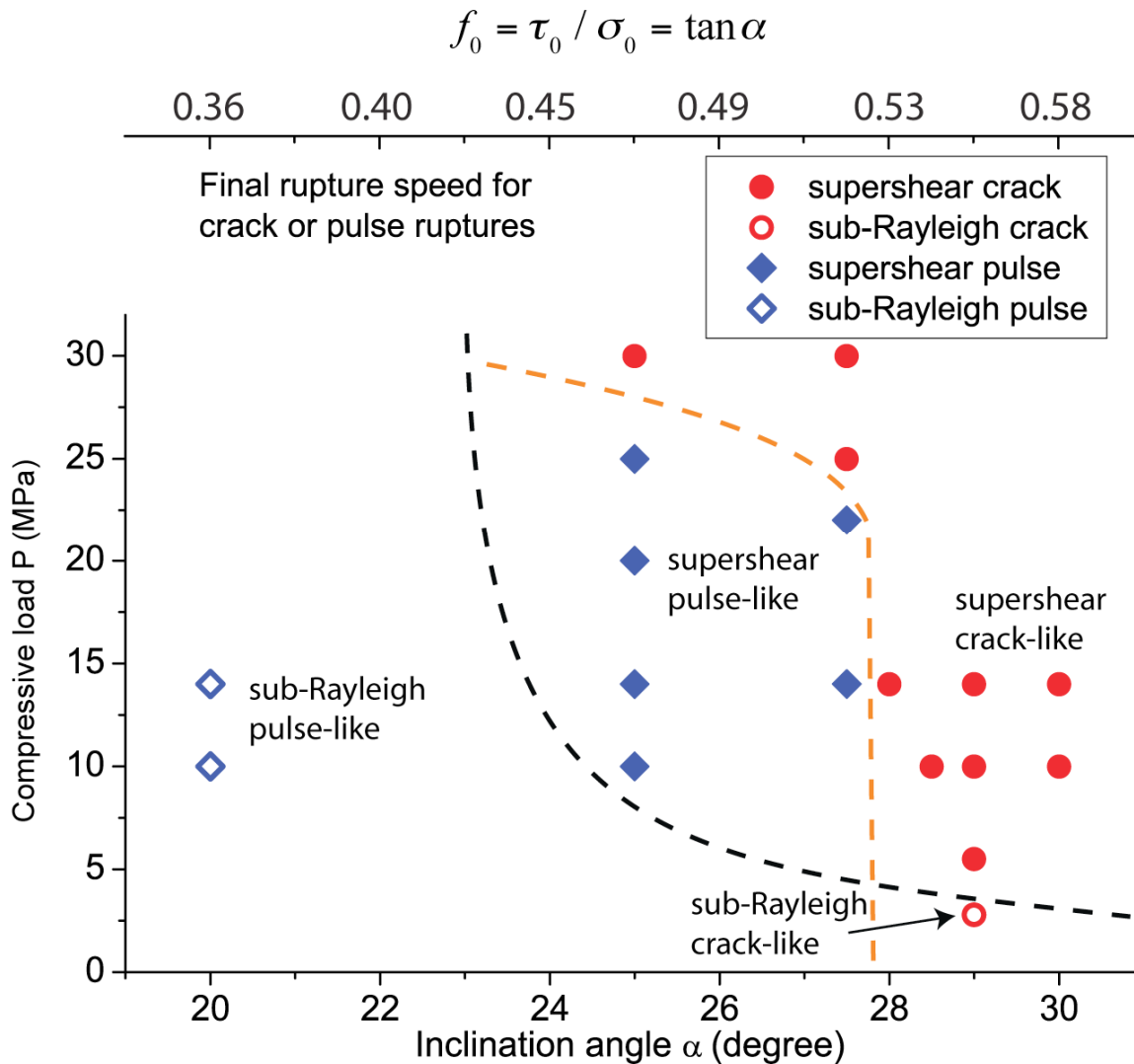


Figure 3.15: Map of pulse-like (diamonds) vs. crack-like (circular dots) modes and sub-Rayleigh (open symbols) vs. supershear (filled symbols) rupture propagation observed in our experiments. The boundary between pulse-like and crack-like modes (orange dashed line) is drawn based on the experimental results to qualitatively separate the two regimes. The boundary between ruptures that do and do not have supershear propagation (black dashed line) is drawn based on the theoretical analysis as discussed in the text.

Chapter 4

Numerical Analysis of Rupture Mode Variation with Slip-weakening Friction and Rate-and-state Friction

4.1 Introduction

In this Chapter, the numerical model of Chapter 2 is used with both slip-weakening and velocity-weakening friction formulations in an effort to reproduce the experimentally observed pulse-like and crack-like rupture modes presented in Chapter 3. As discussed in Chapter 1, we find that linear slip-weakening friction cannot produce pulse-like modes, even in the presence of the dynamic nucleation procedure used in experiments, while velocity-weakening friction can indeed reproduce both pulse-like and crack-like modes, as expected from our analysis in Chapter 3. However, the particular form of velocity-weakening friction considered in this Chapter has difficulties in reproducing the full range of experimental observations due to several uncertainties, such as the choice of

friction parameters and detailed description of nucleation procedure. In addition, we notice that the theory of Zheng and Rice (1998) on rupture mode prediction does not take into account the effect of nucleation mechanism and several friction parameters, which may have considerable impact on the establishment of rupture mode as shown by our simulations.

4.2 Difficulty of simulating pulse-like ruptures using slip-weakening friction

Adopting the same numerical model as in Chapter 2, we start by simulating experiments on rupture modes with linear slip-weakening friction. As discussed in Chapter 2, there are two parameter regimes which can match experimental results of supershear transition: (1) $f_s = 0.6, f_d = 0.2, D_c = 13 \mu\text{m}$, and (2) $f_s = 0.6, f_d = 0.34, D_c = 1 \mu\text{m}$. We aim to use these parameters to match the experimental results of Chapter 3 (Fig. 3.15). we concentrate on inclination angles from 20 to 30 degrees and two levels of compressive load, $P = 10 \text{ MPa}$ and 14 MPa . In this regime, experimental results show the rupture mode variation from pulse-like to crack-like, and we use this general trend for comparison with our simulations.

First of all, friction parameters (1), $f_s = 0.6, f_d = 0.2, D_c = 13 \mu\text{m}$, are implemented. The resulting rupture modes are illustrated in Fig. 4.1. The rupture initiation mechanism is the same dynamic normal stress reduction of $5 \mu\text{s}$ in duration as introduced in Chapter 2

with $a = 5$ mm and $\Delta\sigma = 5$ MPa. There are only two distinctive cases in this simulated map of rupture modes: supershear crack-like rupture and no rupture. A dashed line separating the two regimes indicates an abrupt transition between these two modes, without the presence of either sub-Rayleigh pulse, supershear pulse, or sub-Rayleigh crack. This is clearly inconsistent with experimental results.

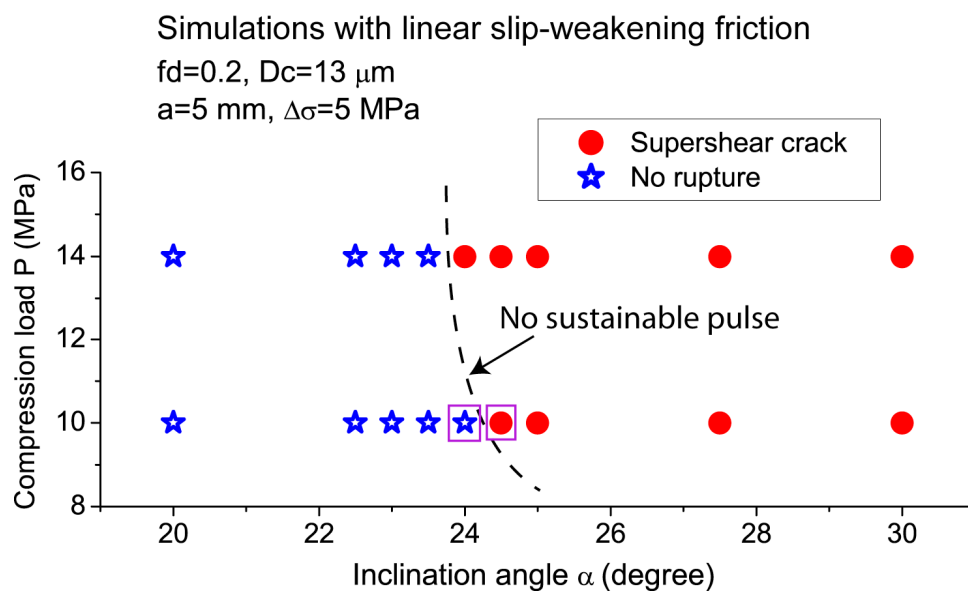


Figure 4.1: Numerical simulations with linear slip-weakening friction with the parameters $f_s = 0.6$, $f_d = 0.2$, and $D_c = 13$ μm . Only supershear ruptures or no ruptures occurs for the experimental parameters studied. There are no pulse-like ruptures. Two representative cases separated by 0.5 degree in the inclination angle and marked by the small rectangles are illustrated in Fig. 4.2.

In order to illustrate the abrupt rupture mode change, two representative cases are selected on two sides of the dashed line as marked by small rectangles in Fig.4.1. The inclination angles are 24 and 24.5 degrees, and the equivalent prestress levels are 0.45 and 0.46 respectively. Fig.4.2 draws the snapshots of the spatial distribution of sliding velocity every 8 μs starting from 4 μs for the two cases. From Fig.4.2 (a)(b), we can see that the initiation procedure nucleates two crack-like ruptures in the center of the interface, with almost identical sliding profiles. This is reasonable because the trivial difference in prestress is not sufficient to compete with stress change due to the nucleation procedure. The initial profile is mainly determined by the induced normal stress drop. At a later time of 12 μs , the rupture quickly dies out for 24-degree case (Fig.4.2c), but the rupture still exists for 24.5-degree case (Fig.4.2d). The distinction is even more profound at 20 μs : a completely healed interface versus a crack-like rupture on the verge of transitioning into supershear speeds, as shown in Fig.4.2e&f. Accumulated slip distributions for the two cases are plotted in Fig.4.2 g&h for every 2 μs . They clearly show an arresting rupture in the 24-degree case and an expanding crack in the 24.5-degree case. Two red stars mark the locations where supershear speed transition happens for the 24.5-degree case.

The difficulty of producing pulse-like rupture in a model with slip-weakening friction is corroborated by the additional simulations with the friction parameters (2), $f_s = 0.6$, $f_d = 0.34$, $D_c = 1 \mu\text{m}$. Two cases with the inclination angles 22.5 degrees and 23 degrees are presented to show the accumulated slip distributions for every 5 μs . The lower-angle case (Fig.4.3.a) does not produce a sustained rupture. However, if we add 0.5 degrees to the inclination angle, rupture propagates with the crack-like mode (Fig.4.3b).

The map of rupture modes for this parameter regime, which is not shown here, exhibits similar features as in Fig.4.1: transition between supershear crack-like modes and no rupture, without any pulse-like rupture in between.

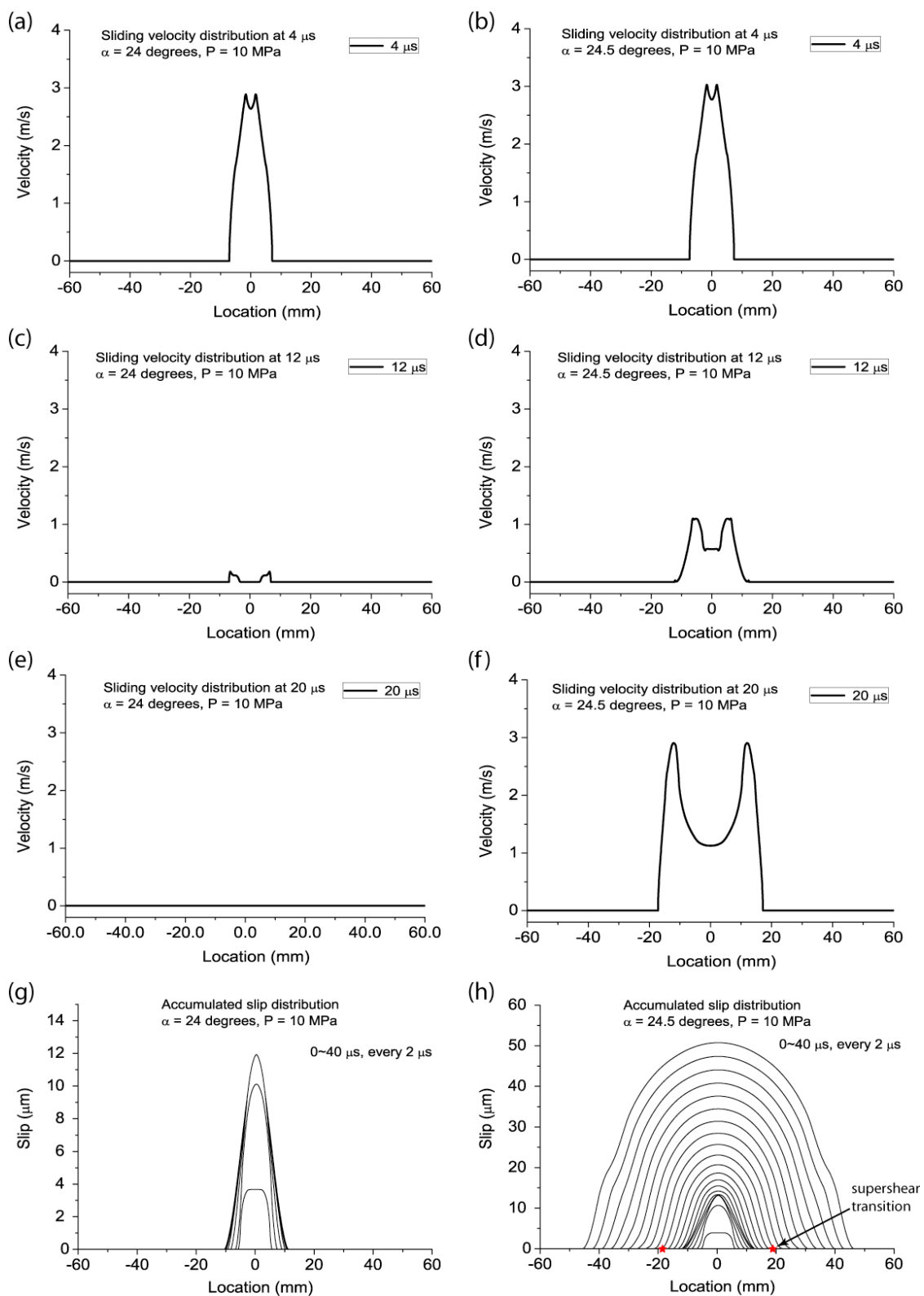


Figure 4.2: Snapshots of sliding velocity and accumulated slip distributions for two representative simulations with a 0.5 degree difference in the inclination angle. The left column displays the 24-degree case which is an arresting rupture after the nucleation. The right column corresponds to a conventional crack-like rupture which transitions to super-shear speeds at the location of 19.2 mm.

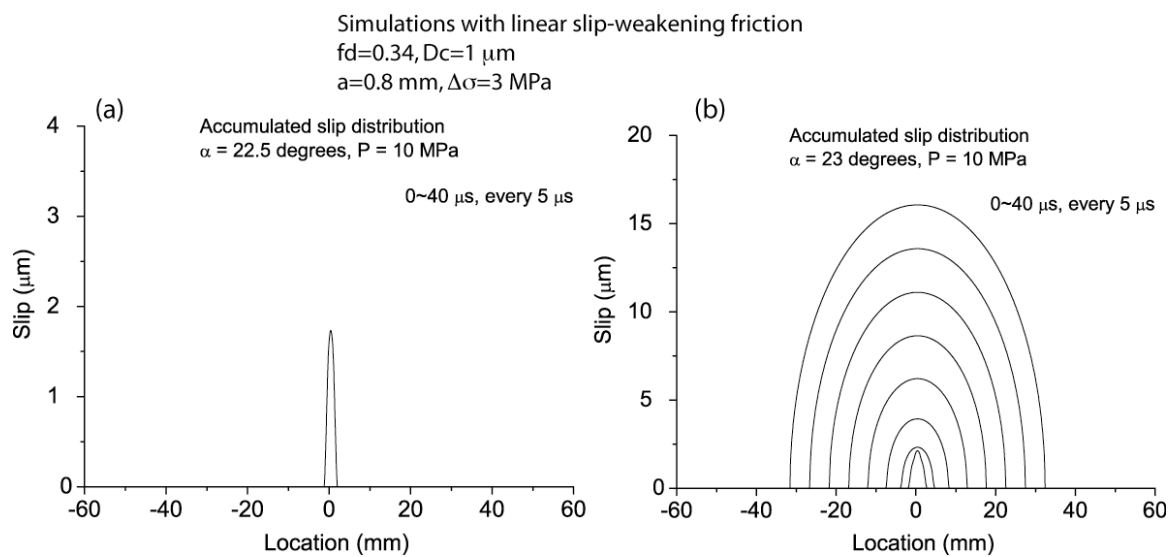


Figure 4.3: Simulations with linear slip-weakening friction with parameters $f_s = 0.6$, $f_d = 0.34$, and $D_c = 1 \mu\text{m}$. In this case, the same conclusion could be drawn that no pulse-like rupture is likely to exist. (a) and (b) are two representative cases with half degree difference in the inclination angle.

Hence we see that, simulations with linear slip-weakening friction and the dynamic rupture nucleation mechanism cannot match the experimentally observed pulse-like modes.

Instead of rupture mode transition from pulse-like to crack-like as observed in experiments, simulations present a direct change from no rupture to crack-like rupture with a small increase in prestress. This is consistent with prior theoretical studies (Heaton, 1990; Perrin et al., 1995; Zheng and Rice, 1998) that predict that slip-weakening friction is not sufficient to maintain pulse-like sliding, as the healing edge of the pulse needs velocity-weakening feature to arrest the sliding and stationary re-strengthening to maintain the locking status. Obviously none of these requirements can be satisfied by linear slip-weakening friction. What we have demonstrated is that even in the presence of dynamic rupture nucleation procedure, slip-weakening friction cannot produce pulses. Note that the nature of short duration time of the current nucleation procedure is in fact favorable for pulse-like rupture. When normal stress goes back to the original level at the end of the nucleation procedure, typically after 5 μs , the sliding velocity in the nucleation region is substantially decreased or even zero. This creates a bilateral pulse-like shape. For example, for 24-degree case, the unloading phase completely stops the sliding of the central region and two small dying pulses are left over at 12 μs (Fig.4.2c). We find that, even if we feed a pulse-like rupture into the fault system governed by slip-weakening friction, this pulse cannot be sustained and quickly dies out or develop into a crack depending on the prestress conditions and other factors.

4.3 Simulating rupture mode variation with enhanced rate-and-state friction

In this section, we study whether the rate-and-state friction enhanced with flash heating would be able to match our experimental results. Even if a qualitative match is obtained in Chapter 3, it is still necessary to do the actual simulations for two reasons. First, we need to investigate how the nucleation mechanism would affect the rupture mode under different experimental conditions. Second, in the steady-state analysis, some friction parameters do not enter the equation and the transient evolution of friction towards steady-state is ignored. As a result, the table of predicted rupture mode in Chapter 3 may need to be corrected accordingly. Some friction parameters inferred in Chapter 3 may not be the best choice given the complicated transient process of rupture nucleation and propagation.

4.3.1 Experimental measurements of rate-and-state friction parameters on Homalite interfaces

The laboratory-derived rate-and-state friction (Dieterich 1979; Ruina 1983) has been established to study the rock friction at relatively low sliding velocity of the order of 10^{-6} m/s. To reflect features observed in experiments, it stresses the velocity dependence of the friction, either velocity-weakening or velocity-strengthening. For Homalite material, it is velocity weakening (evidence will be shown later) which means steady-state friction becomes lower with higher sliding velocity. For pure velocity-weakening friction, the sliding is an ill-posed problem because the self-serving cycle of weakening will lead to the infinity of velocity. A direct effect serves the role of regularization by imposing an

increase in friction when sliding velocity is subject to a sudden increase. In addition, a state variable θ is introduced to represent the average contact lifetime of the mating interface. Under this general framework, rate-and-state friction has several different formulations. The one we adopt in our simulation is the Dieterich-Ruina law, or aging law, enhanced with flash heating. For constant normal stress σ , the friction coefficient $f = \tau / \sigma$ can be expressed as:

$$\left\{ \begin{array}{l} f = f_w + \frac{\boxed{f_* + a \ln \frac{V}{V_*} + b \ln \frac{V_* \theta}{L}} - f_w}{1 + \frac{L}{\theta V_w}} \\ \frac{d\theta}{dt} = 1 - \frac{V\theta}{L} \end{array} \right. \quad (4.1)$$

regular rate-and-state friction part
↓

where f_* , V_* are reference friction and sliding velocity, a , b are rate-and-state parameters, L is the characteristic slip ($\theta = L/V$ in steady state), V_w is the flash heating parameter where friction will experience rapid weakening for $V > V_w$, f_w is the residual friction or dynamic friction when interface slides at high slip rate. During the steady-state sliding ($d\theta/dt = 0$), friction coefficient can be written as:

$$f_{ss}(V) = f_w + \frac{f_* + (a-b) \ln(V/V_*) - f_w}{1 + V/V_w}. \quad (4.2)$$

As we can see, at low slip rates $V \ll V_w$, this friction obeys the standard form of rate-and-state friction as $f_{ss}(V) \approx f_* + (a-b) \ln(V/V_*)$, with $(a-b) < 0$ for velocity weakening

and vice versa. For high slip rates $V \gg V_w$, $V \sim V_{dyn}$, $f_{ss}(V) \approx f_w + \frac{\hat{f}}{V/V_w}$, where

$\hat{f} = f_* - f_w + (a-b)\ln(V_{dyn}/V_*)$. The weakening term V/V_w in the denominator has the dominant effect, and friction quickly approaches f_w as interface weakens. This friction law seamlessly combines the low sliding velocity and high sliding velocity regimes, which could describe the friction response during the rapid velocity change around rupture tip.

In order to quantify the rate-and-state friction parameters, we collaborate with Brian Kilgore and Nick Beeler (USGS) and Chris Marone (PennState) to perform rate-and-state friction tests on Homalite interface. These tests are conducted with the double shearing configuration which is shown in Fig.4.4. In the schematic drawing of the setup, two pairs of Homalite plates are compressed by the side steel blocks to apply the normal confinement. Each pair of Homalite consists of a shorter plate and a longer plate; and the longer one is glued to the central steel block. Frictional sliding is enforced by the push-down movement of the central block and the slip and stress are recorded by the sensors. Fig.4.4b gives a close-up look at the actual specimens. Note that the same surface preparation procedure has been applied here to ensure the friction property measurement is relevant. In addition, the straightness of the interface is well controlled to maintain the uniform sliding. Different from our dynamic rupture experiment, the sliding speed of such double shearing test is typically of the order of 1 $\mu\text{m/s}$. Therefore, only the regular rate-and-state friction properties in low slip rate regime, such as a , b , L , can be estimated by this test.

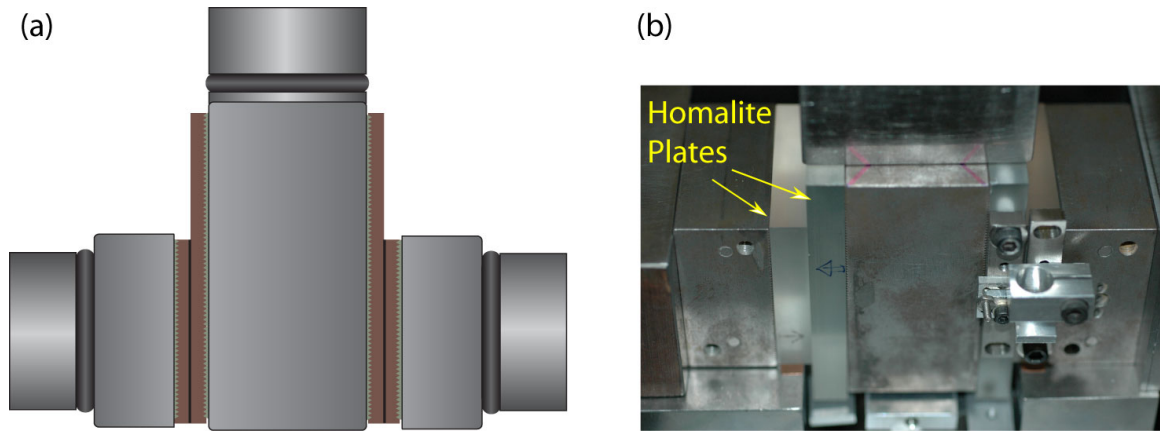


Figure 4.4: Experimental setup of the double shearing tests to measure rate-and-state friction properties. (a) Schematic drawing of the configuration. Two pairs of Homalite plates are confined by the side blocks to form double frictional mating interface. Sliding is enforced by the movement of central block upside down. (b) Real Homalite specimens during the test. The short plate has the size of $50 \text{ mm} \times 50 \text{ mm}$, while the longer plate is $80 \text{ mm} \times 50 \text{ mm}$ (work in progress in collaboration with Brian Kilgore and Nick Beeler, USGS).

The typical rate-and-state friction measurement is done with the velocity stepping test as illustrated in Fig.4.5. Assuming interface is sliding at a reference velocity V_* and the corresponding steady-state friction is f_* , the friction would increase instantaneously by amount of $a \ln(V/V_*)$ when subjected to a velocity jump from V_* to $V(=V_* + \Delta V)$. With velocity-weakening in place, i.e. $(a-b) < 0$, the friction will evolve through slip of the order of L and eventually resettle at a new level of steady-state friction which is

$(b-a)\ln(V/V_*)$ lower than the original one. The reverse change can also happen by decreasing the sliding velocity by ΔV abruptly. The direct effect will act to drag down the friction even further instantaneously but recovery will occur as slip increases. It is notable that although the amplitude of the direct effect is the same for both jump-up and jump-down tests, the evolution of friction towards steady-state is not symmetric, because of the importance of contact time specified in Dieterich-Ruina law.

The actual velocity stepping tests are presented in Fig.4.6 with three cycles to ensure the repeatability of the result. Two sliding velocities $V_1 = 0.1 \mu\text{m/s}$ and $V_2 = 0.01 \mu\text{m/s}$ are used and the steady-state friction levels are marked by two dashed lines respectively. The peaks of the direct effect are labeled with letters A-F. First of all, the average friction coefficient for $0.1 \mu\text{m/s}$ sliding is 0.592 and for $0.01 \mu\text{m/s}$ is 0.604. We take the difference of 0.012 in steady-state friction and use the equation $(a-b)\ln(V_2/V_1)$ to obtain $(a-b) = -0.005$. Then we calculate the average drop in friction at the spikes of A-C to be -0.026. Hence $a = 0.011$ can be computed from the direct effect equation $a\ln(V_2/V_1)$. We could also calculate $f_* = 0.58$ for the reference sliding velocity $V_* = 1 \mu\text{m/s}$.

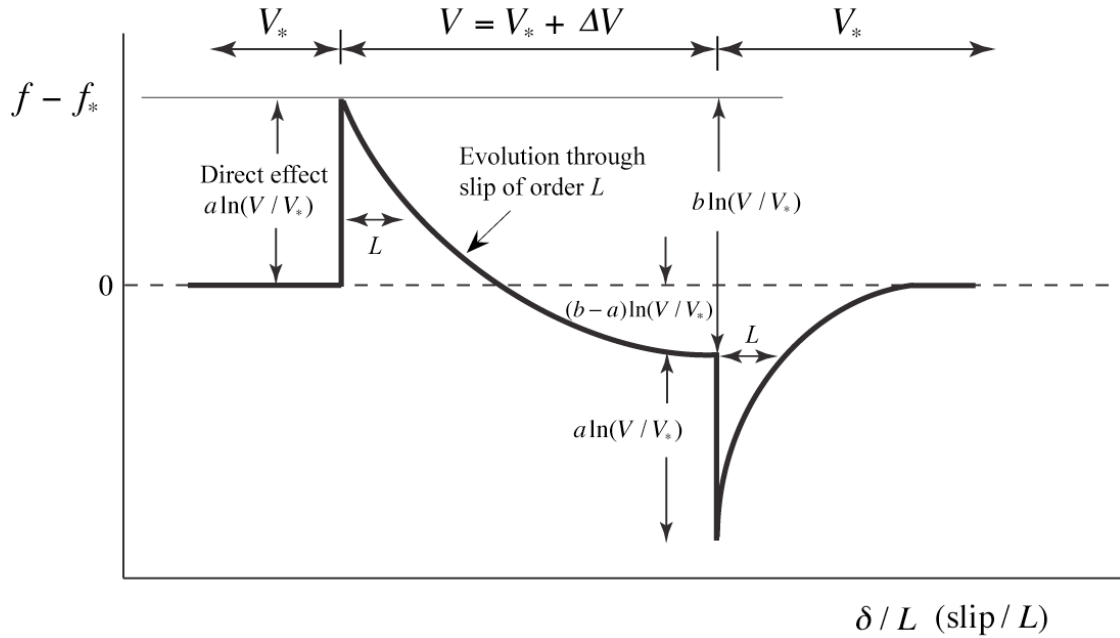


Figure 4.5: Schematic illustration of rate-and-state friction response to velocity stepping tests. The normalized friction is plotted against slip. When a positive velocity change occurs, direct effect will drive friction to a higher level instantaneously. Then depending on whether the friction is velocity-weakening or velocity-strengthening, friction gradually evolves into a steady state level for the new slip rate. Opposite change occurs when we impose a negative velocity change. It is notable that for the Dieterich-Ruina rate-and-state friction implemented in our model, the evolution profiles of velocity increase and decrease are not symmetric.

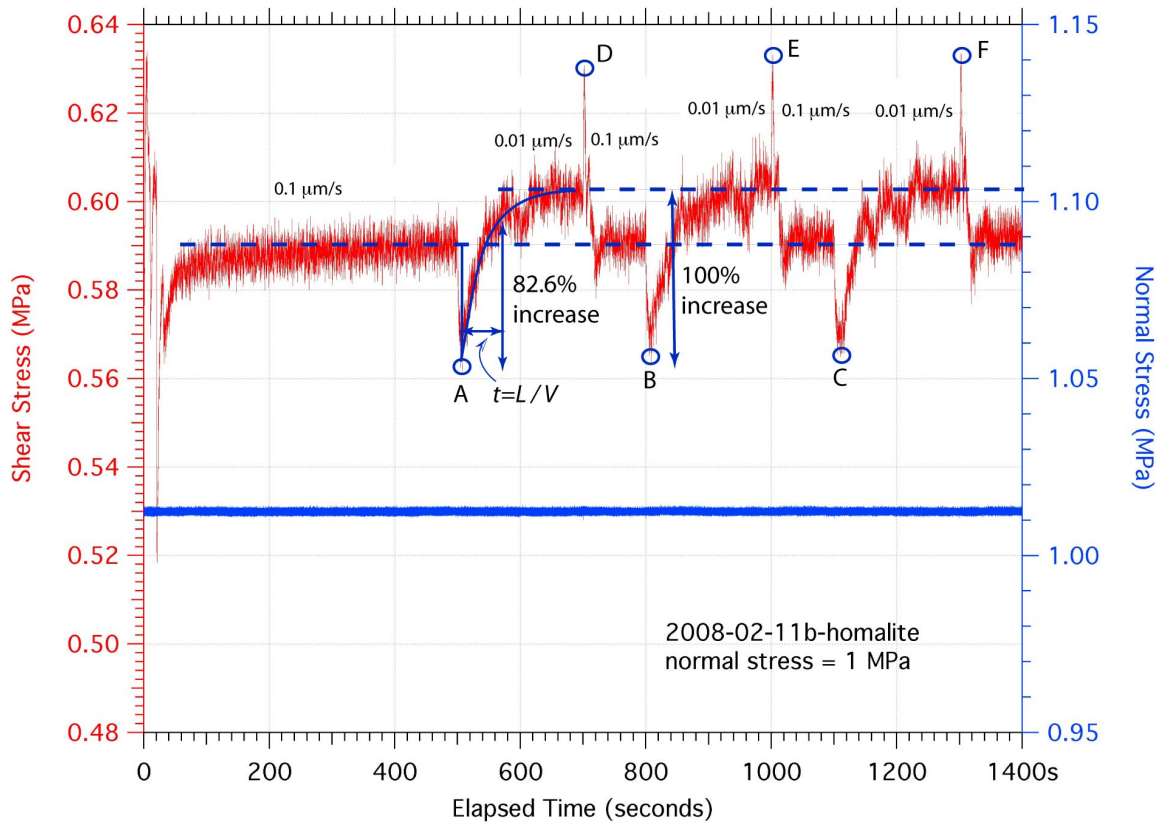


Figure 4.6: Laboratory measured rate-and-state friction of Homalite through velocity stepping tests. Velocity jumps are between $0.1 \mu\text{m/s}$ and $0.01 \mu\text{m/s}$. Three cycles of tests are conducted for both jump-up and jump-down cases. The spikes in friction which correspond to peaks of direct effect are labeled with letters A-F, in which parameter a can be inferred. In addition, two steady-state sliding levels are marked with dash lines to obtain parameter $(a - b)$. The characteristic slip L is determined when evolution of friction has completed 82.6% of the entire change for the jump-down test in this measurement (work in progress in collaboration with Brian Kilgore and Nick Beeler, USGS).

In order to measure the characteristic slip L , we first consider a more general problem and apply the results to the Fig.4.6 later. In a velocity stepping test without specifying the sign of change in velocity, we have:

$$\begin{cases} V = V_1 & \text{for } t < 0 \\ V = V_2 & \text{for } t \geq 0 \end{cases} \quad (4.3)$$

Hence for $t < 0$, the steady state sliding yields the friction and state variable as follows:

$$f = f_* + a \ln(V_1 / V_*) + b \ln(V_* \theta_1 / L) = f_* + (a - b) \ln(V_1 / V_*), \quad \theta = \theta_1 = L / V_1. \quad (4.4)$$

At $t = 0$, when velocity change $V_1 \rightarrow V_2$ happens, friction is changed instantaneously by the direct effect, while state variable is still remained the same as before:

$$f = f_* + a \ln(V_2 / V_*) + b \ln(V_* \theta_0 / L), \quad \theta_0 = \theta_1 = L / V_1, \quad d\theta/dt = 1 - V_2 \theta / L \quad (4.5)$$

We can solve the ODE equation of state variable with the initial condition and get the evolution function of θ as:

$$\theta = \frac{L}{V_2} \left[1 - \left(1 - \frac{V_2}{V_1} \right) e^{-\frac{V_2 t}{L}} \right] \quad (4.6)$$

Therefore, if we substitute the state variable function back to eq.(4.5), we can get expression of friction as:

$$f = f_* + a \ln(V_2 / V_*) + b \ln \frac{V_*}{V_2} \left[1 - \left(1 - \frac{V_2}{V_1} \right) e^{-\frac{V_2 t}{L}} \right] \quad (4.7)$$

Hence the friction prior to and after the stepping test can be concluded as follows:

$$\begin{aligned} f(t < 0) &= f_* + (a - b) \ln(V_1 / V_*) \\ f(t = 0) &= f_* + a \ln(V_2 / V_*) + b \ln V_* / V_1 \\ f(t > 0) &= f_* + a \ln(V_2 / V_*) + b \ln \frac{V_*}{V_2} \left[1 - \left(1 - \frac{V_2}{V_1} \right) e^{-\frac{V_2 t}{L}} \right] \end{aligned} \quad (4.8)$$

At the time of $t = L/V_2$, the accumulated slip is the characteristic slip L , and the friction

at that time can be written as $f = f_* + a \ln(V_2/V_*) + b \ln \frac{V_*}{V_2} \left[1 - \left(1 - \frac{V_2}{V_1}\right) e^{-1} \right]$.

The amount of friction change from the peak of the direct effect up to $t = L/V_2$ is

$$\Delta f = f(t=0) - f(t=L/V_2) = b \ln \frac{(V_2/V_1)}{1 - (1 - V_2/V_1)e^{-1}} \quad (4.9)$$

If velocity jumps up ten times larger $V_2/V_1 = 10$, change of friction is $\Delta f = 0.84b$. The complete change in friction from the peak of the direct effect to the new steady state friction is $b \ln(V_2/V_1) = 2.3b$, and the percentage of the friction change completed by the characteristic slip L is 36.5%. Similarly, if velocity jumps down ten times smaller $V_2/V_1 = 1/10$, change of friction is $\Delta f = -1.9b$. The complete change in friction from the peak of the direct effect to the new steady state friction is $b \ln(V_2/V_1) = -2.3b$, and the percentage of the friction change completed by the characteristic slip L is 82.6%.

In Fig.4.6, if we apply the results discussed above to the first velocity jump-down cycle, we can pinpoint the location where 82.6% of the friction change occurs and find the corresponding time t . If we multiply the time by the velocity 0.01 $\mu\text{m/s}$, we find that the value of L varies from 0.3~0.4 μm in these tests. This would result in a 6~8 μm effective break-down slip in the linear slip-weakening law, which is actually consistent with our estimation in Chapter 2.

Apart from the friction properties at low slip rates, the high-speed friction, especially at the velocity of the order of 1 m/s, is very important for our modeling. As we can see in

experimental results in Chapter 3, the average velocity of the rupture front is typically several meters per second. The weakening process near the rupture front is critical to determine the mode of the rupture as well as the rupture speed. Flash heating at frictional asperity contact has been considered in recent earthquake studies as a mechanism for strong weakening of the fault interface during sliding (Rice 1999; Tullis and Goldsby 2003; Parakash 2004; Hirose and Shimamoto, 2005; Prakash and Yuan 2004; Beeler and Tullis 2003; Rice 2006). The main idea is that during rapid sliding, the accumulated heat generated by friction increases the local temperature of asperity contacts. This temperature change would significantly reduce the strength of the contacts and hence the frictional resistance of the interface. If slip rate is of the order of the threshold velocity V_w , flash heating is activated and friction reduces as shown in eq.4.2. This critical velocity can be defined as (Rice 2006):

$$V_w = \left(\frac{\pi\alpha}{D} \right) \cdot \left[\frac{\rho c (T_w - T_f)}{\tau_c} \right]^2, \quad (4.10)$$

where $\alpha = 3.61337 \times 10^{-8} \text{ [m}^2/\text{s]}$ is the thermal diffusivity, D is the asperity size of contact, τ_c is the shear strength of individual contacts, $T_w - T_f$ is the temperature rise during the flash heating process, $\rho c = 1.39 \times 10^6 \text{ [J/m}^3\text{K]}$ is the heat capacity per unit volume. D is comparable to the characteristic slip L in rate-and-state friction, hence a reasonable guess is $D = 0.4 \mu\text{m}$ as suggested by the previous sections. Typically shear strength is one tenth of the elastic shear modulus of the bulk material, therefore $\tau_c = 0.1\mu = 142.96 \text{ MPa}$. Temperature change that leads to weakening could be as high as several hundred degrees, $T_w - T_f = n \times 10^2 \text{ K}$. As a result, V_w is estimated as:

$$V_w = \left(\frac{3.14 \times 3.61 \times 10^{-8}}{0.4 \times 10^{-6}} \right) \cdot \left[\frac{1230 \times 1.13 \times 10^3 \times n \times 100}{142.96 \times 10^6} \right]^2 = 0.27 \times n^2. \quad (4.11)$$

Since Homalite is a polymer material, a reasonable guess for $(T_w - T_f)$ is of the order of its glass transition temperature, which is estimated to be around 100 °C. Having said that, the reasonable range of parameter V_w is between 0.1 m/s to 1 m/s. The residual friction coefficient f_w in the velocity-dependent friction description is analogous to the dynamic friction coefficient of linear slip-weakening friction used in Lu et al. (2008), and so we consider values of $f_w = 0.2 \sim 0.34$ here. The results of friction parameter estimation are summarized in Table 4.1.

Table 4.1: Rate-and-state friction parameters

Parameter	Symbo	Value
Rate-and-state friction parameter	a	0.011
Rate-and-state friction parameter	b	0.016
Rate-and-state velocity weakening	$a - b$	-0.005
Characteristic slip	L	0.3 ~ 0.4 μm
Reference sliding velocity	V_*	1 $\mu\text{m/s}$
Reference friction coefficient	f_*	0.58
Residual friction coefficient	f_w	0.2 ~ 0.34
Critical sliding velocity for flash heating	V_w	0.1 ~ 1 m/s
Initial state variable	θ_0	60 s

4.3.2 Comparison of experimental and simulated rupture modes

We use the friction parameters listed in Table 4.1 to conduct rupture simulations on interfaces governed by enhanced rate-and-state friction. The prestress conditions in our simulations are based on the experimental situations with inclination angles from 20 to 30 degrees and two compressive load levels of 10 MPa and 14 MPa.

One representative series of rupture simulations with friction parameters $V_w = 0.2$ m/s, $L = 0.3$ μm , and $f_w = 0.2$ is shown in Fig.4.7. Unlike the map of rupture modes simulated with linear slip-weakening friction (Fig.4.1), the simulations in Fig.4.7 produce all experimentally observed rupture modes, including pulse-like and crack-like ruptures, some of which are supershear ruptures. In particular, pulse-like rupture is obtained in simulations that correspond to 23~25 degrees inclination angles for 10 MPa compressive load. As in experiments, variation of rupture mode from pulse-like to crack-like is obtained in simulations as inclination angle is increased. At the same time, there is no exact match with experimental results in terms of rupture modes at particular angles. Rupture modes are determined by sliding velocity histories at 10 mm away from the center of the interface, which is the same criterion discussed in section 4.2. Besides no rupture, pulse-like ruptures and crack-like ruptures, there is a “pulse-crack” rupture mode marked by squares in Fig.4.7. In this mode, rupture propagates as pulse-like rupture for a while before the once-healed region starts to slide again. Depending on the prestress level and interface strength, such re-activation of sliding may happen near the trailing edge of the sliding pulse, or close to the center of the interface. On the local velocity history profile, it often appears as a sliding pulse followed by a crack-like rupture.

In order to illustrate the typical rupture modes simulated using rate-and-state friction, Fig.4.8 showcases snapshots of sliding velocity distribution as well as local sliding histories for three cases, with the inclination angles of 25, 27, and 30 degrees, and the compressive load of 10 MPa. The left column is the spatial sliding velocity distributions at 15 μ s. For the case of 25 degrees, the bilateral pulse-like rupture in Fig.4.8a is approaching 20 mm location and maintaining substantial sliding speed at the rupture front. In contrast, the 30 degrees inclination angle results in a conventional crack-like rupture as shown in Fig.4.8e. At the intermediate angle of 27 degrees, rupture is pulse-crack mode at 15 μ s. The re-activation of sliding happens on the trailing end of the sliding pulse. This secondary rupture front develops and spreads backwards to sweep the central part of the interface. Up to 15 μ s, almost the entire central interface, except for a very small patch, has re-activated sliding. At later times (which are not shown here), all sliding patches are connected and a crack-like mode is established. In the right column, local sliding velocity history and normalized shear stress are plotted at the location 10 mm for three different angles. This allows us to observe the frictional signature of

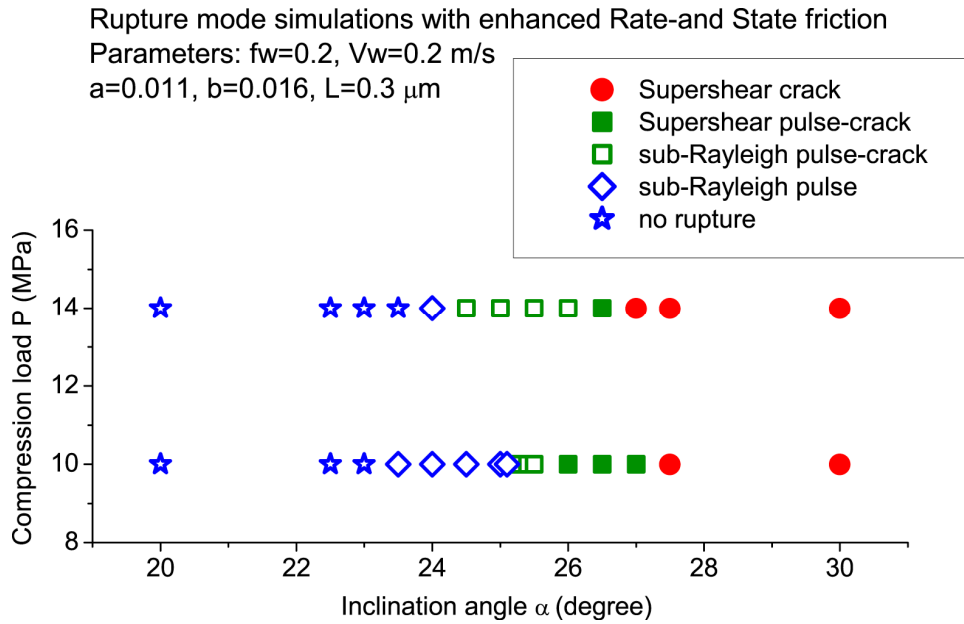


Figure 4.7: Rupture mode simulations with rate-and-state friction enhanced with flash heating. Friction parameters are chosen as: $f_* = 0.58$, $f_w = 0.2$, $L = 0.3$ μm , $a = 0.011$, $b = 0.016$, $(a - b) = -0.005$, $V_* = 1 \times 10^{-6}$ m/s, $V_w = 0.2$ m/s, initial $\theta = 60$ s. Same nucleation procedure as in slip-weakening calculations has been applied with the half nucleation size 6 mm and maximum normal stress reduction 7 MPa. Different rupture modes are marked by different symbols. The transition from pulse-like to crack-like with increasing the inclination angle is broadly consistent with our experimental results.

different rupture modes. The common feature is the normalized shear stress increases to the level of about 0.8 to initiate sliding. This effective static friction is higher than 0.6 used in linear slip-weakening friction because of the direct effect of rate-and-state friction. When sliding happens, the once high friction is quickly weakened to the level of about 0.2 in the vicinity of rupture front. Then, along with the decrease of sliding veloc-

ity, shear stress gradually increases due to the velocity-weakening feature. When the background shear stress is not sufficiently high to equal the dynamic friction and support the sliding, healing occurs and sliding forms a pulse-like rupture as shown in Fig.4.8(b). For higher prestress cases, the slip velocity does not go down as much, healing effect is not strong enough and hence sliding continues. For intermediate prestress case, the healing process cannot elevate the interface strength fast enough; hence when perturbation of shear stress arrives, it is possible for the once-healed interface to slide again.

Although rate-and-state friction stresses the importance of velocity-dependent friction, rupture front behaves similarly to slip-weakening friction during the dynamic rupture propagation process: shear stress increases from pre-loading level to the static strength of the interface to initiate sliding, and then weakens towards the dynamic strength level over some slip. The difference is that weakening is not linear with respect to the slip because of the inherent strong velocity dependence. After friction reaches dynamic level, it does not remain constant, instead, it evolves depending on the rupture mode. Fig.4.9a plots the normalized shear stress against slip for the three representative cases discussed in Fig.4.8. For comparison purpose, linear slip-weakening friction is also plotted, with the parameters adopted in section 4.2. In order to study the equivalence between two friction laws, the effective fracture energy is calculated as:

$$G = \int_0^{\delta_0} [\tau(\delta) - \tau_r] d\delta \quad (4.12)$$

where $\tau(\delta) = f\sigma$ is shear traction, τ_r is the residual shear stress, and the upper limit δ_0 of the integral in eq.(4.12) is the slip where residual shear stress is reached. For linear

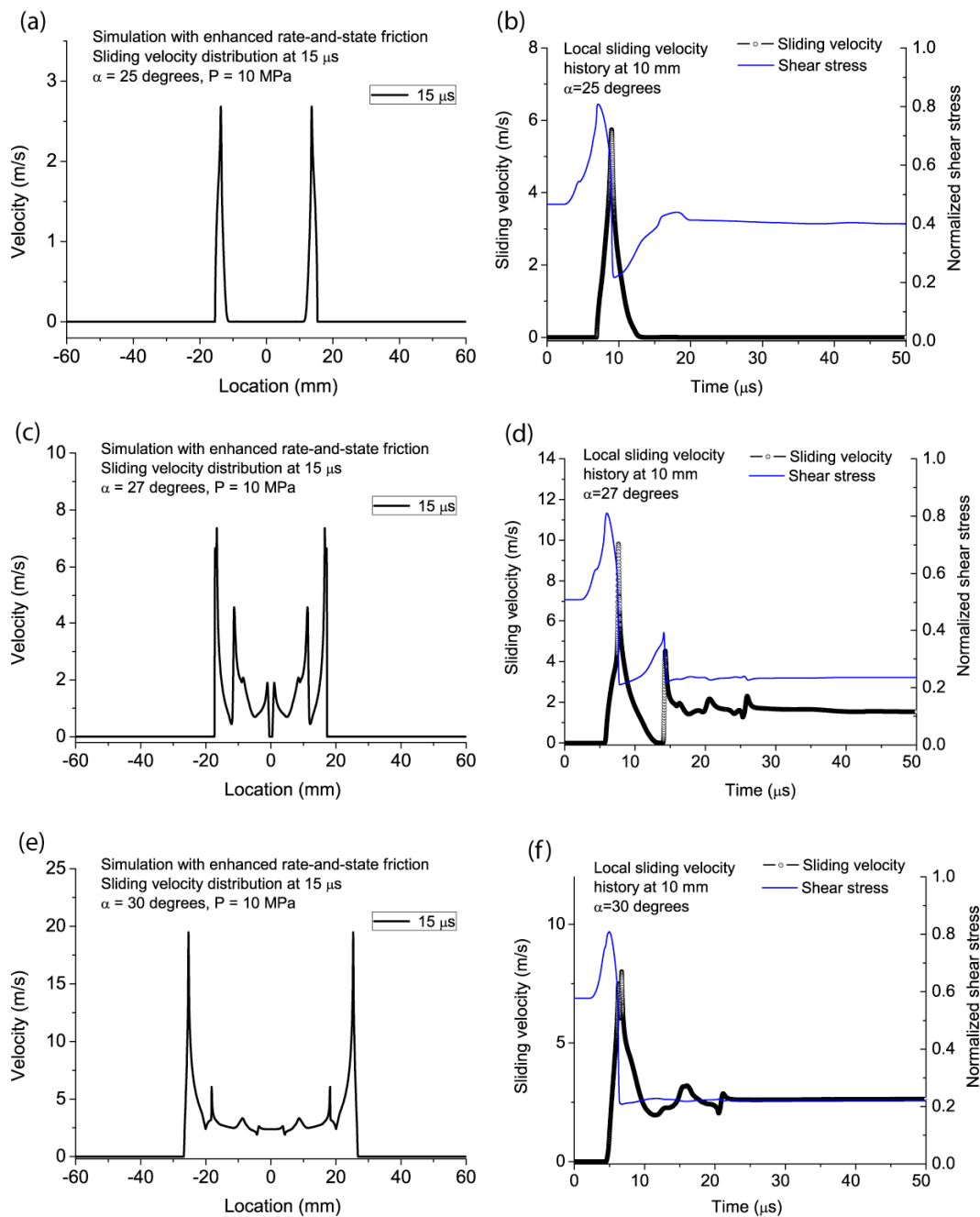


Figure 4.8: Three representative simulations with inclination angles of 25, 27, and 30 degrees and compressive load of 10 MPa. Left column is the sliding velocity distribution at 15 μs . The right column illustrates local sliding velocity and friction at 10 mm away from the center of the interface.

slip weakening friction, $\tau_r = \sigma f_d$ and $\delta_0 = D_c$; while for rate-and-state friction, τ_r is the minimum shear stress which is determined numerically and so is the corresponding slip δ_0 . The results are summarized in Table 4.2. As evident from the table, we get similar values of fracture energy for two different friction laws. However, the seismic ratio $s = \frac{\tau_s - \tau_0}{\tau_0 - \tau_d}$ is quite different. Seismic ratio of linear slip weakening law is smaller because of the lower value of τ_s . Hence we would expect simulations with linear slip-weakening friction to favor supershear transition. This is confirmed by comparing two diagrams of rupture mode in Fig.4.1 and Fig.4.7: there are more instances of supershear rupture in the case of slip-weakening friction. We also plot the normalized shear stress against sliding velocity to see how friction evolves during the rapid acceleration and healing in Fig.4.9b. A steady-state friction curve is superimposed onto the plot for comparison. Around the initiation of sliding, shear stress is higher than the corresponding steady-state friction. This situation drives sliding towards higher velocity, which is evident by the clockwise movement on the plot. Because of the velocity-weakening feature, the shear stress is getting closer to the steady state friction during such process; and for some cases two curves will converge and steady-state sliding is established as a result, e.g. for the 30 degrees case. However, for lower prestress case, e.g. 25 degrees, the shear stress evolution curve falls below the steady-state friction when velocity decreases, which leads to complete healing of the sliding. If we change the flash heating parameters f_w and V_w , we change the shape of the steady-state friction curve and ultimately the rupture mode selection.

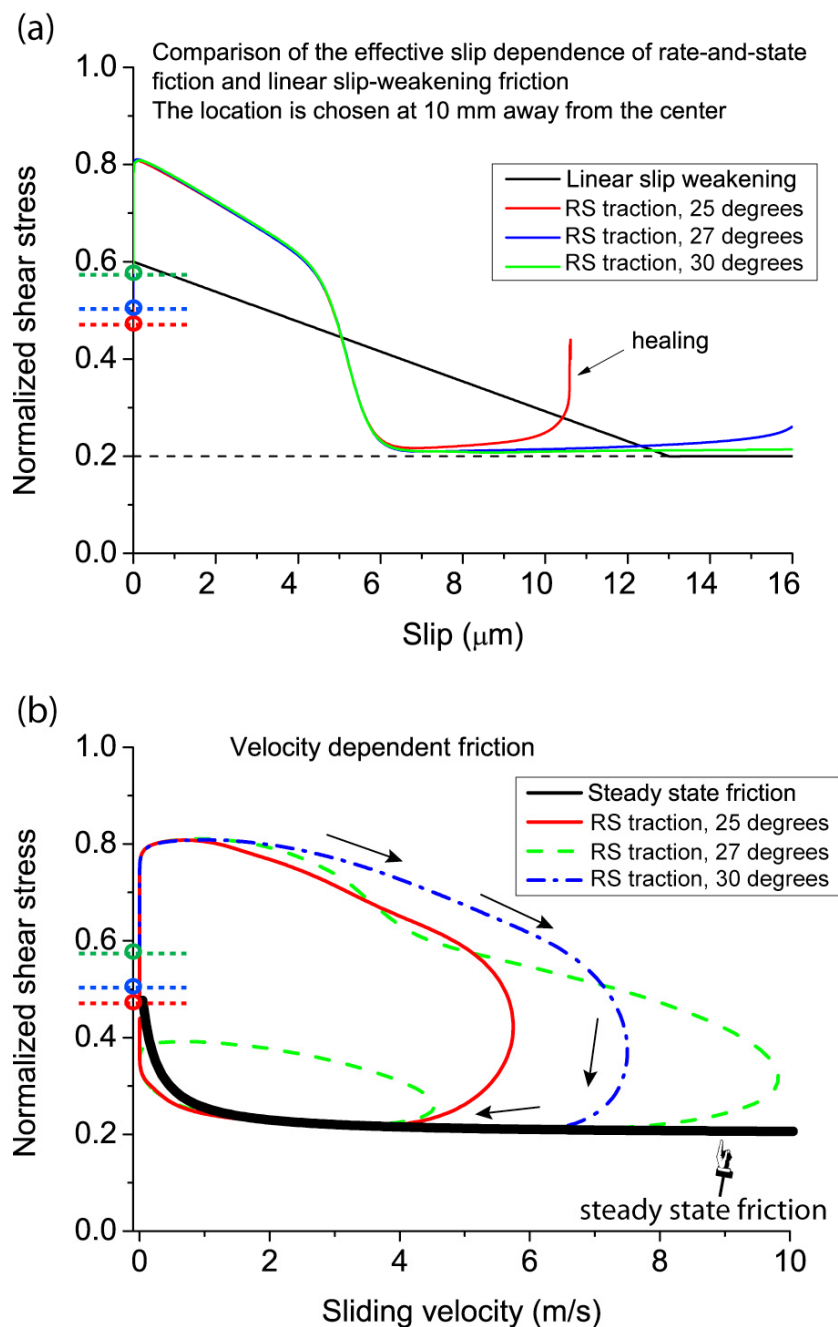


Figure 4.9: (a) Comparison of effective slip dependence of rate-and-state friction and linear slip-weakening friction. The local sliding history is at the location 10mm is shown (b) Friction evolution during the rupture propagation process. For crack-like rupture, friction eventually resides on the steady-state friction curve.

Table 4.3 shows the table of T based on the theory of Zheng and Rice (1998) to predict rupture mode. Table 4.3a is for the same friction parameters as used for Fig.4.9, while Table 4.3b has smaller values of f_w and V_w . As evident by the values in the table, smaller values of f_w and V_w lead to smaller T , which favors crack-like ruptures. In other words, stronger velocity weakening would promote sliding. Another notable feature in Table 4.3 is that all the values of T falls into crack-like regime. This supports our intuitive conclusion that the rupture nucleation mechanism in our simulations actually favors pulse-like rupture. The competing effect between stronger velocity weakening and nucleation mechanism helps to generate a map of rupture mode which qualitatively matches the experiments (Fig.4.7).

Table 4.2: Fracture energy for different friction laws (per unit area)

Note: compressive load $P = 10$ MPa

	Linear slip-weakening friction	Rate-and-state with $f_w = 0.2$, $V_w = 0.2$ m/s, $a = 0.011$, $b = 0.016$	Rate-and-state with $f_w = 0.1$, $V_w = 0.1$ m/s, $a = 0.011$, $b = 0.016$	Rate-and-state with $f_w = 0.2$, $V_w = 0.2$ m/s, $a = 0.005$, $b = 0.01$
25°	26 J/m ²	24.6 J/m ²	29.8 J/m ²	21.3 J/m ²
27°	26 J/m ²	25.1 J/m ²	29.9 J/m ²	21.6 J/m ²
30°	26 J/m ²	25.3 J/m ²	30.0 J/m ²	21.6 J/m ²

Table 4.3: Table of T generated based on the theory of Zheng and Rice (1998). Two sets of friction parameters are used: (a) $f_w = 0.2$, $V_w = 0.2$ m/s (b) $f_w = 0.1$, $V_w = 0.1$ m/s.

(a)

$P \setminus \alpha$	20°	21°	22°	23°	24°	25°	26°	27°	28°	29°	30°
14 MPa	0.14	0.11	0.09	0.07	0.06	0.05	0.04	0.04	0.03	0.03	0.03
10 MPa	0.21	0.16	0.12	0.1	0.08	0.07	0.06	0.05	0.05	0.04	0.04

Color	Predicted mode
	Pulse-like or no rupture
	Crack-like

Friction parameters:

$(a - b) = -0.005$

$f_s = 0.58, f_w = 0.2, V_w = 0.2$ m/s

(b)

$P \setminus \alpha$	20°	21°	22°	23°	24°	25°	26°	27°	28°	29°	30°
14 MPa	0.03	0.03	0.02	0.02	0.02	0.02	0.02	0.01	0.01	0.01	0.01
10 MPa	0.04	0.04	0.03	0.03	0.03	0.02	0.02	0.02	0.02	0.02	0.02

Color	Predicted mode
	Pulse-like or no rupture
	Crack-like

Friction parameters:

$(a - b) = -0.005$

$f_s = 0.58, f_w = 0.1, V_w = 0.1$ m/s

As suggested in the previous section, enhancing velocity weakening promotes crack-like rupture mode. In order to test this hypothesis, we use smaller values of flash heating parameters $f_w = 0.1$ and $V_w = 0.1$ m/s as in Table 4.3b while keeping everything else the same. The resulting map of rupture modes is presented in Fig.4.10a. We can see that there are many more instances of crack-like ruptures in this map and the region for pulse-like rupture is suppressed. In fact, for $P = 14$ MPa, there is no presence of pulse-like rupture; and for $P = 10$ MPa, there is only one pulse-like rupture case at 21 degrees. The plot of slip versus normalized shear stress is given in Fig.4.10b for three different inclination angles. It is evident that all three cases are for crack-like rupture because there is no healing process. And because of the decrease of dynamic friction, seismic ratio is even smaller which favors supershear transition. This is corroborated by the fact that there are more supershear rupture instances in Fig.4.10a than in Fig.4.7.

Another approach to changing the map of rupture modes is to vary rate-and-state friction coefficients a and b . For example, if we decrease a but keep $(a - b)$, the steady-state friction response is maintained but direct effect is reduced that leads to (1) reduced seismic ratio because of the smaller static friction strength, which promotes supershear rupture and (2) smaller fracture energy and relatively higher prestress, which promotes crack-like rupture mode.

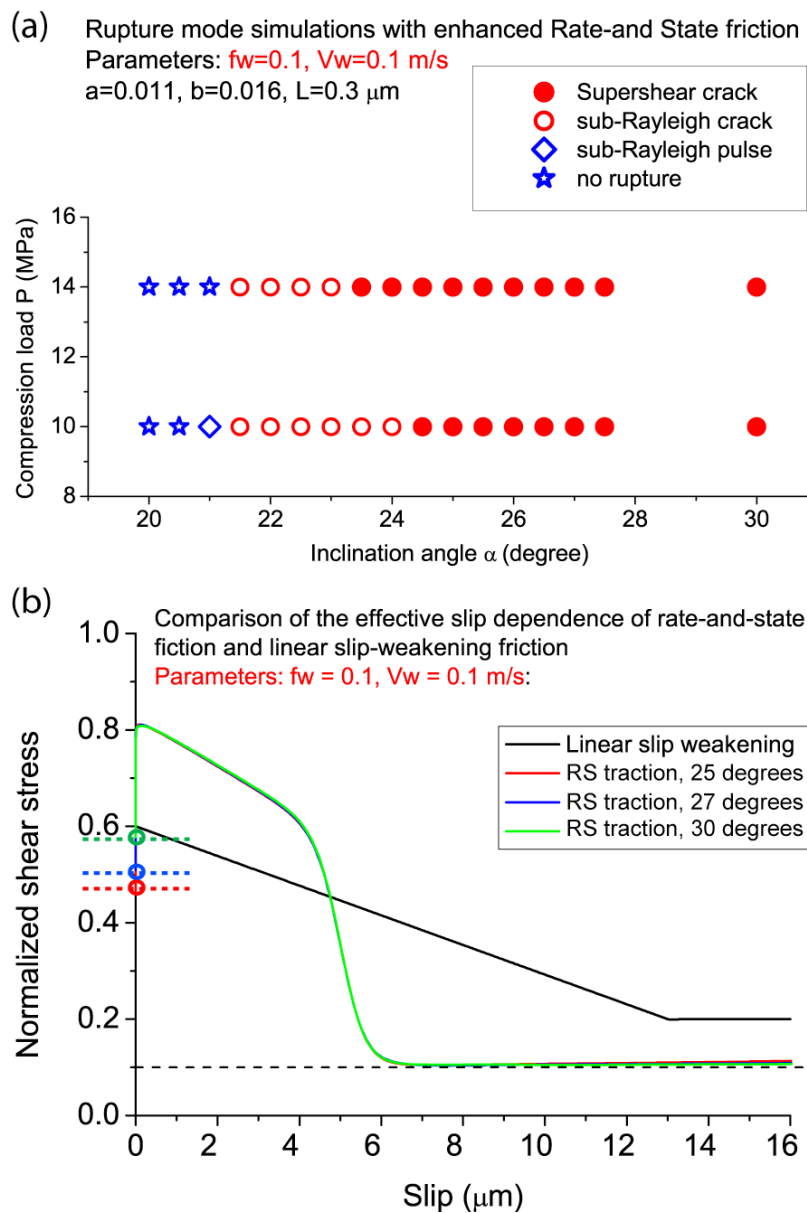


Figure 4.10: (a) Rupture mode simulations with flash-heating parameters $f_w = 0.1$ and $V_w = 0.1$ m/s. Compared with Fig. 4.7, more crack-like ruptures are present. (b) Effective slip dependence of friction. The residual friction is reduced to 0.1 and hence seismic ratio is smaller. Ruptures are more likely to transition to supershear speeds.

The results for a smaller value of $a = 0.005$ are illustrated in Fig. 4.11(a). We see that the general distribution of rupture modes is shifted to the left side by about 1 to 1.5 degrees comparing to Fig.4.7. The table of T would not change, because we maintain the value of $(a - b) = -0.005$. The absolute values of a and b do not enter the theory of Zheng and Rice (1998) and hence have no impact on the predicted rupture modes. As a matter of fact, Zheng and Rice (1998) considered two different combinations of (a, b) but they determined that the cut-off value of T does not need to be adjusted because of different a . While our simulations support that conclusion, as the map of rupture modes changes only slightly, the simulations also show that the impact of different values of a may be might be larger than expected, especially if more significant variations in a are considered.

If we look into the details of Fig.4.11a, there are two “abnormal” data points which correspond to 24.5 and 25 degrees and 14 MPa. They are sub-Rayleigh pulse-like ruptures positioned between the pulse-crack ruptures. For the two neighboring conditions, 24 degrees and 23.5 degrees, ruptures turn into a crack-like mode from the initial pulse-like stage. However, the mechanism is different: for 24 degrees case, the re-activation of sliding happens at the trailing end of the sliding pulse; while for 25.5 degrees case, additional sliding pulses emerge from the center of the interface and eventually join the main rupture to form a crack-like shape. For the two special cases of 24.5 and 25 degrees, rupture maintains its pulse-like shape during the entire course of the propagation. In Fig.4.12, the spatial distribution of the sliding velocity and accumulated slip are plotted every $5 \mu\text{s}$ for the case of 25 degrees and 14 MPa. It is evident that a sustained bi-lateral pulse-like

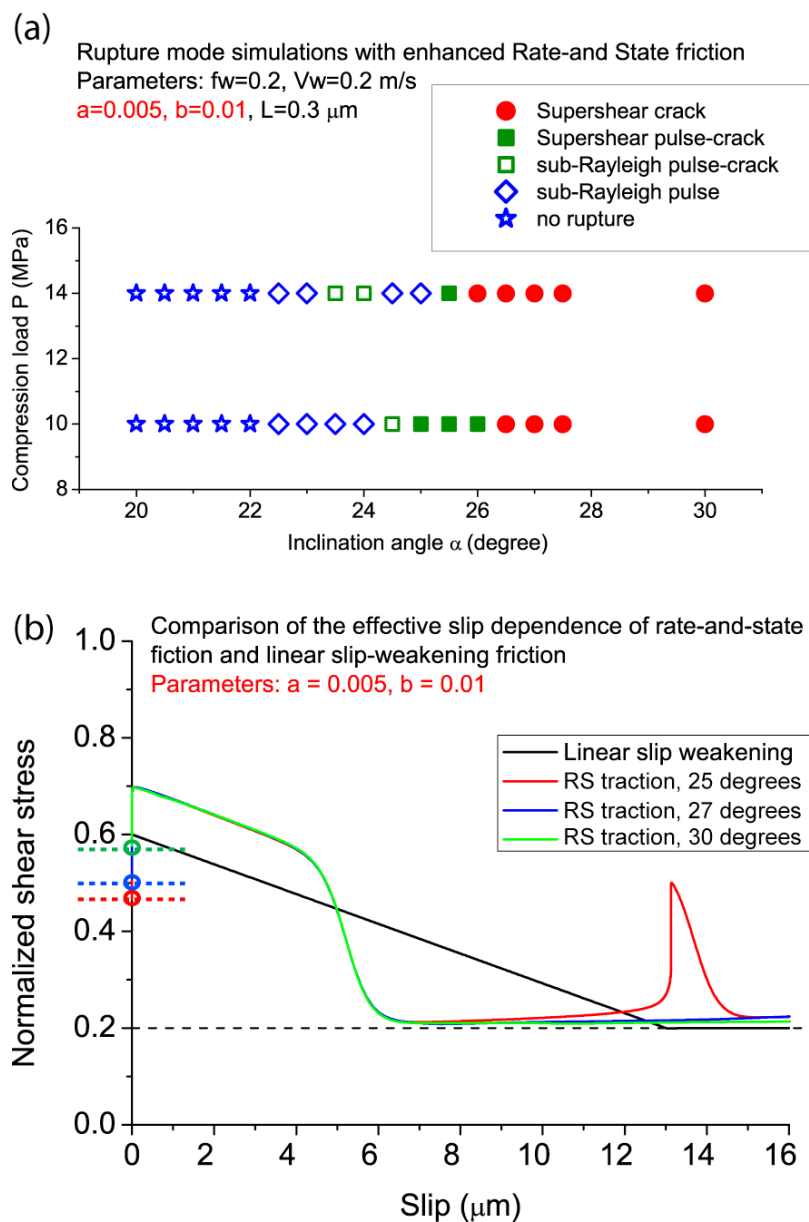


Figure 4.11: (a) Rupture mode simulations with rate-and-state friction parameters $a = 0.005$, $b = 0.01$, $(a - b) = -0.005$. Note that the direct effect is reduced but velocity weakening is maintained. According to the steady-state analysis of Zheng and Rice (1998), we would not anticipate a change in rupture modes. However, because of the lower effective static friction and fracture energy, this change promotes crack-like rup-

tures as well as supershear transition. (b) Comparison of effective slip dependence of enhanced rate-and-state friction and linear slip-weakening friction.

rupture is propagating with a growing peak velocity. These complex map of rupture modes indicates how sensitive the rupture modes are to the experimental conditions and our choices of friction parameters. These observations emphasize the importance of quantifying friction properties

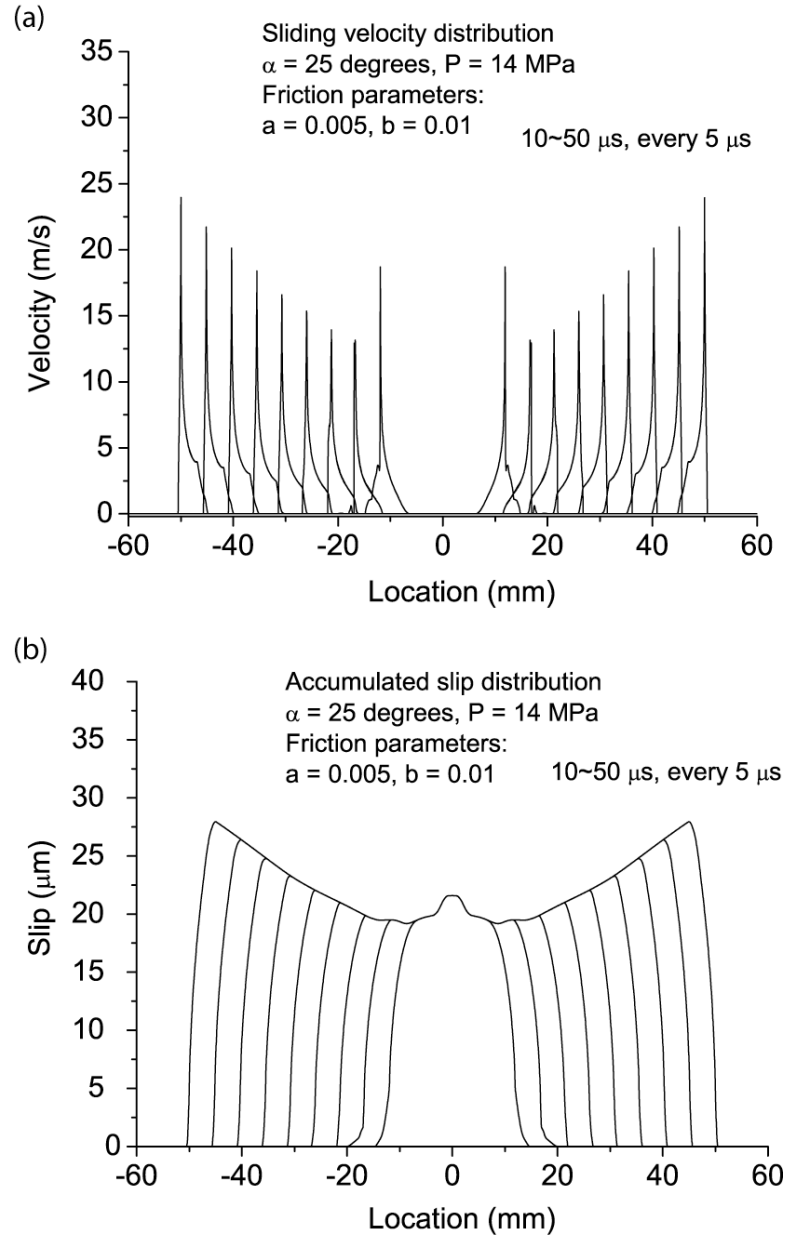


Figure 4.12: Growing pulse-like rupture at 25 degrees inclination angle and 14 MPa compressive load. The friction parameters are $a = 0.005$, $b = 0.01$. (a) Snapshots of velocity distribution every 5 μs . (b) Snapshots of accumulated slip every 5 μs .

Another parameter that does not enter the theoretical predictions of Zheng and Rice (1998) is the characteristic slip L . However, since the estimated critical crack size

$$L_c = \frac{\pi}{4} \frac{\mu L}{(b-a)\sigma} \quad (\text{Rice and Ruina, 1983})$$

linearly scales with L , varying L might change the nucleation and propagation characteristics of the rupture for the fixed length of the nucleation region in our model. Here we use four different values of L , ranging from 0.3 to 0.05 μm , to investigate this potential effect. Fig.4.13 shows the snapshots of sliding velocity distribution at 15 μs for different selection of L . Experimental conditions are chosen as inclination angle 20 degrees and compressive load 10 MPa. With the decrease of L , rupture mode varies from no rupture, to pulse-like rupture, pulse-crack rupture, then to crack-like rupture. One explanation is that the ratio of the nucleation region and the critical crack size is increased with the smaller value of L and hence the rupture initiation procedure creates a strong initial rupture which is then maintained by spontaneous propagation. Similar conclusion has been reached in Chapter 2, where we study supershear transition distance. These results indicate that the characteristics slip L would also impact rupture modes in our simulations, in addition to a and b as we discussed in the previous section.

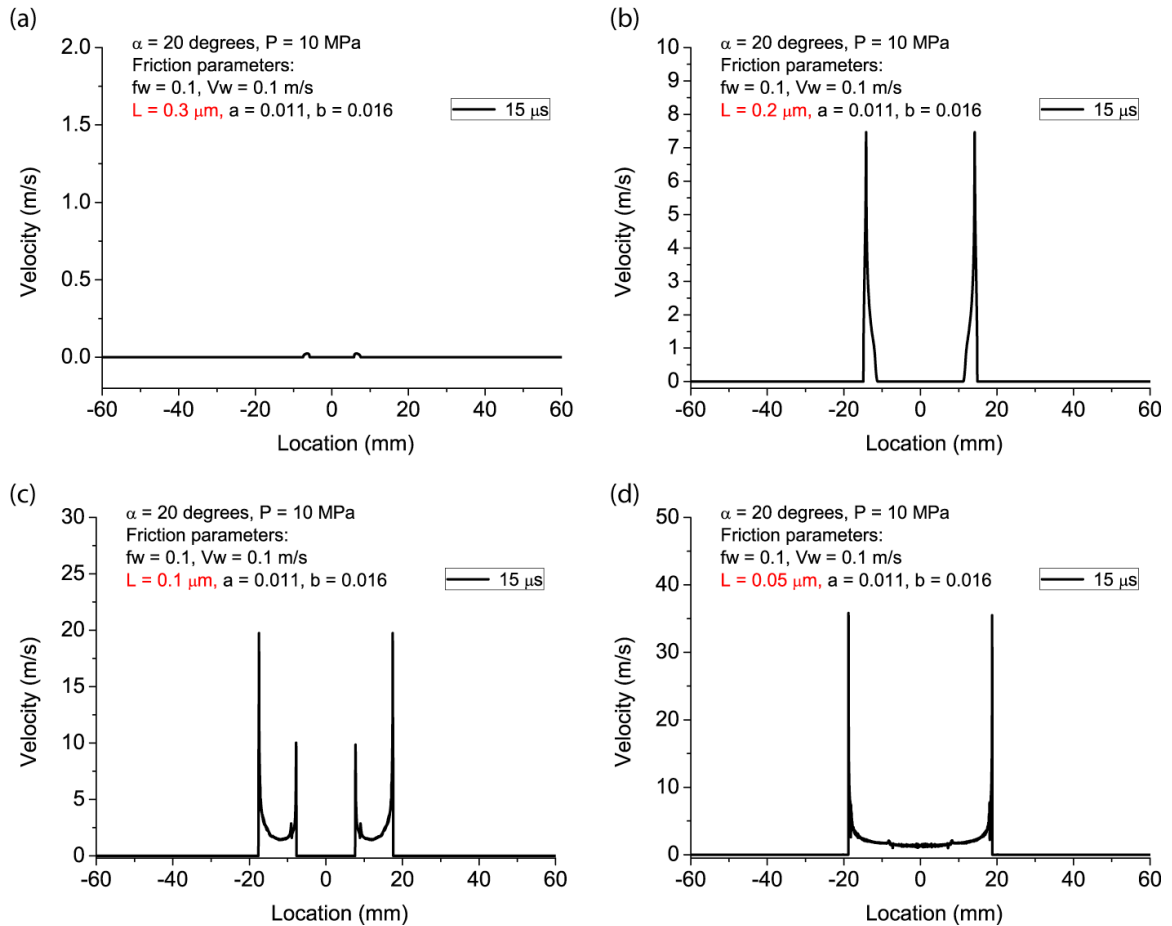


Figure 4.13: Rupture mode variation with different selection of characteristic slip L of the rate-and-state friction. Snapshots of sliding velocity at $15 \mu\text{s}$ are shown. Experimental conditions are the inclination angle of 20 degrees and compressive load of 10 MPa. (a) $L = 0.3 \mu\text{m}$. (b) $L = 0.2 \mu\text{m}$. (c) $L = 0.1 \mu\text{m}$. (d) $L = 0.05 \mu\text{m}$.

4.4 Conclusions and discussion

In this Chapter, we numerically model the rupture mode experiments with both linear slip-weakening friction and rate-and-state friction enhanced with additional weakening at

high slip rates. The results show that linear slip-weakening friction is unable to produce pulse-like rupture in our modeling. Even though the current dynamic rupture nucleation procedure creates initial slip pulses to the fault interface, those pulses could not be sustained on a slip-weakening fault: they either die out or develop into crack-like ruptures. This result emphasizes that other features of dynamic friction should be introduced into the constitutive law to match the experimentally observed rupture mode variation. In particular we need to add velocity weakening and stationary re-strengthening as proposed by previous studies (Heaton 1990; Perrin et al 1995; Zheng and Rice 1998).

Sustained pulse-like ruptures start to appear when we adopt the rate-and-state friction enhanced with flash heating. Through the collaboration with Brian Kilgore and Nick Beeler from USGS, we are able to measure rate-and-state friction of Homalite at low sliding velocity. The high-speed friction properties are estimated based on the flash-heating model. The results show that we can qualitatively produce rupture mode variation from pulse-like to crack-like, as what we observed in experiments. However, it is difficult to get precise agreement between modeling and experiments due to many uncertainties. The rupture nucleation mechanism has not been quantified yet. Values for several friction parameters are still rough estimations. The flash-heating effect has not been experimentally confirmed in Homalite, and its parameters have not been measured. In particular, the proper formulation of flash-heating may need to involve another state variable, with a different characteristic slip L . The direct effect of rate-and-state friction may be diminished at high slip rates from the values measured at low slip rates. Despite these uncer-

tainties, the current results already indicate that this modeling has potential to match experimental results if we constrain a number of model parameters.

In terms of the effects of specific parameters on rupture modes, we find that reducing the values of flash heating parameters V_w and f_w facilitates the crack-like rupture mode, as predicted by the theory of Zheng and Rice (1998). However, our simulations show that some parameters which were not included in the theory can still affect the establishment of rupture modes, in our experiments, in part due to their interaction with the nucleation procedure. In particular, the results depend on the individual values of a , b , and characteristic slip L .

Our studies show that we can use the rupture experiments of Chapter 3 as a benchmark problem to test and validate different friction models. This, in turn, can help us to advance our understanding of rupture dynamics and improve the current friction laws. The signature characteristics of our experiments, such as high temporal and spatial resolution, simple geometry and well-documented material properties, are necessary to construct a standard comparison problem.

Chapter 5

Future Work

5.1 Localized friction measurement at high slip rates

As we show in previous Chapters, friction properties at high slip rates play a significant role in rupture dynamics; in particular, certain characteristics of propagating shear ruptures, such as supershear transition distance and rupture mode, are very sensitive to the selection of friction parameters. The results in Chapter 4 illustrate that in addition to the efforts of measuring rate-and-state friction of Homalite, it is crucial to directly determine the friction response at the slip rates of the order of 1~10 m/s, which correspond to the sliding velocity level in the vicinity of rupture front and for much of the active rupture. The weakening process in that velocity regime is likely to dominate the behavior of sliding and determine rupture modes and other characteristics.

Here we present a design that will enable us to measure high-speed friction of Homalite in a setting that involves localized sliding velocity and stress measurement. Using the

impact shearing setup (Rosakis et al. 1999; Lykotrafitis et al. 2006), frictional sliding can be enforced by the strike from a projectile (Fig.5.1), which is launched from a compressed-air gas gun. At a location along the interface, a strain gage rosette would be glued to the surface of the specimen, either above or below the interface, to measure stress components during dynamic sliding. The velocimetry technique can be applied to measure sliding velocity at the same location where stress information is extracted. Depending on the pressure of the gas gun, the initial impact speed can vary from 1 m/s to 20 m/s or even higher, which covers all possible high speeds of interest. The design of the projectile is flexible and, in fact, can be creative to induce various types of sliding. One possibility is to machine a composite projectile made half of Homalite and half of steel, with Homalite on the striking side (Fig. 5.1). Because of the big mismatch in wave impedance, $(\rho c)_{steel} / (\rho c)_{Homalite} \approx 17.4$, the transmission wave from Steel-to-Homalite material boundary would result in roughly 1.9 times of the particle velocity of the incident wave. The two strikes, one from the initial impact between Homalite projectile and specimen and the other one from the transmission waves between steel and Homalite boundary within the projectile, would likely introduce two different levels of sliding velocity with a jump in between. This framework resembles the philosophy of velocity stepping tests of rate-and-state friction but operates at a much higher slip rate.

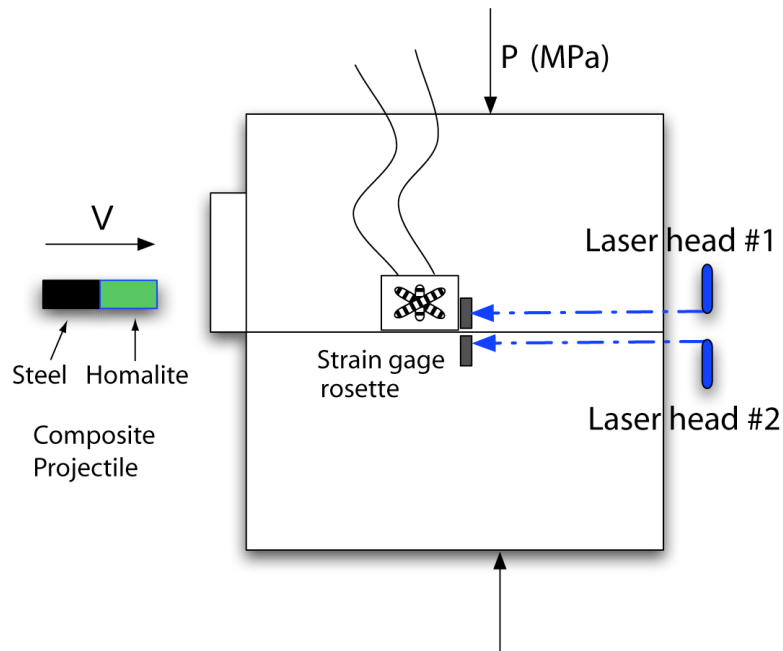


Figure 5.1: Experimental configuration for high-speed friction measurements. Two flat Homalite plates are compressed with P . At a chosen location, reflective membranes and a strain gage rosette are put near each other to measure the local sliding velocity as well as the stress components. A Steel-Homalite composite projectile is launched with a gas gun at a high speed of the order of 1~10 m/s. Interfacial sliding is induced by the impact shearing effect. A steel bar is attached to the side of the Homalite plate to avoid shattering.

In order to demonstrate the possibility of sustained slip velocities at the measurement locations as well as of the velocity jump scenario, we conduct finite element simulations with ABAQUS. Initial impact velocity $V = 10$ m/s and compressive load $P = 2$ MPa are applied to the system and linear slip-weakening friction is used to model the interface resistance to sliding. The resulting horizontal velocity field is shown in Fig. 5.2. At the

time of 15 μs , the initial compressive waves from the impact of the projectile (Homalite part) and specimen have propagated into the bulk of the material and initiated some sliding on the interface. At the same time, the reflection wave moves backwards and reaches the Steel-Homalite boundary, as evident by the distinct velocity difference in the center of the projectile. The higher-velocity steel part then pushes the Homalite part and effectively initiates a second strike with higher velocity. As a result, at the time of 45 μs , a bar-shaped higher velocity region moves into the bulk of the specimen and larger sliding velocity on the interface is expected to occur.

The simulated sliding velocity history at the location of 50 mm as marked in Fig.5.2 is plotted in Fig.5.3. There are two semi-constant stages of sliding velocity, with about 1.5 m/s and 3.5 m/s and duration of more than 25 μs , which should be sufficient to establish steady-state friction at each speed. In addition, the sharp velocity jump caused by the secondary strike can be used to study the direct effect and evolution of friction.

In conclusion, the preliminary calculations show promising results for the possibility of high-speed friction measurement using this experimental design. This experiment may significantly advance our understanding of high-speed friction. Such localized velocity-friction measurement will potentially reveal more details than possible to acquire in conventional friction tests that average over the entire specimens.

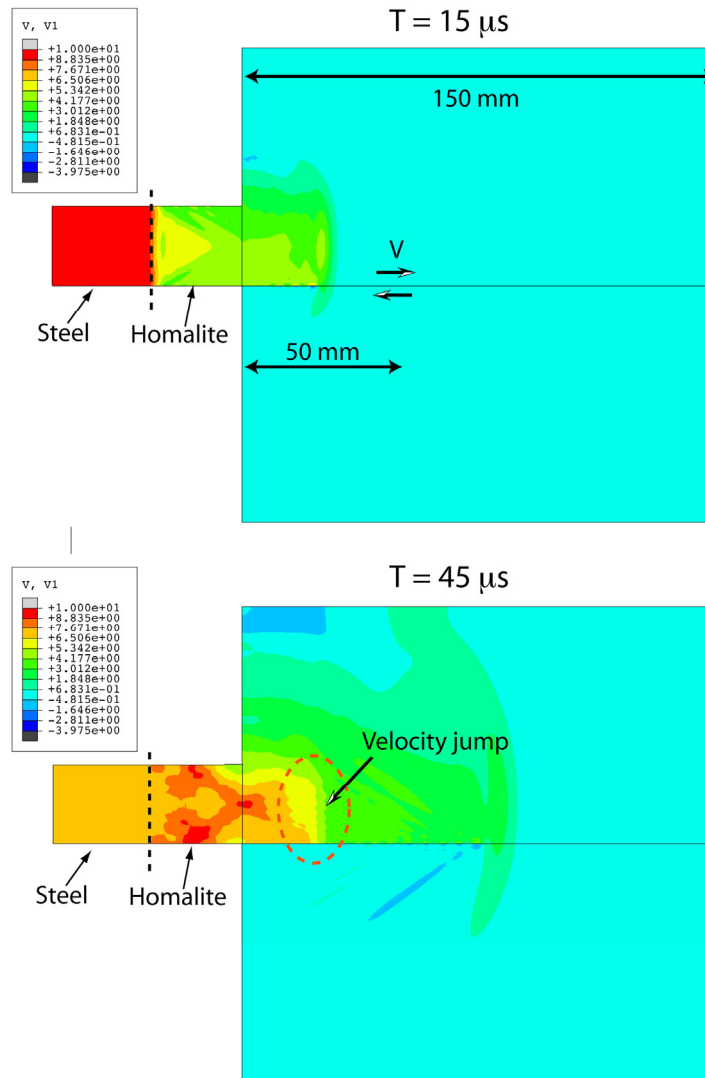


Figure 5.2: Finite element simulation of the horizontal velocity field by ABAQUS. Compressive load $P = 2$ MPa and initial impact speed $V = 10$ m/s are used. The interface is modeled using linear slip-weakening friction with $f_s = 0.6$, $f_d = 0.2$, $D_c = 13$ μm . The transmission waves from Steel-Homalite boundary in the projectile have higher speed. This would induce a velocity jump as evident by comparing the velocity field at 15 μs and 45 μs .

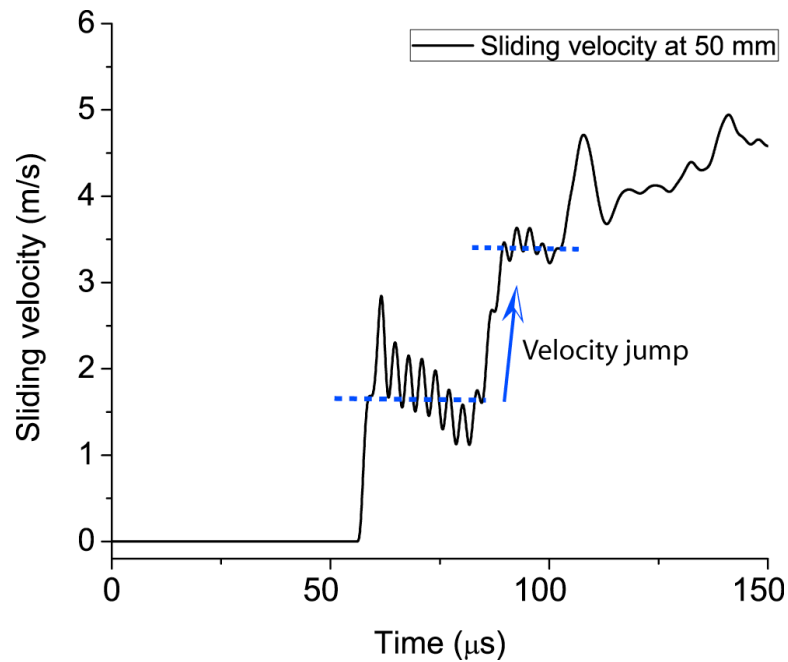


Figure 5.3: FEM-simulated sliding velocity at the location of 50 mm from the impact. There are two levels of sustained high velocity and a velocity jump from about 1.5 m/s to 3.5 m/s due to the transmission waves from the material boundary of Steel and Homalite in the projectile. This velocity profile can be used to study high-speed friction at two different levels and the frictional response to the velocity jump, similar to rate-and-state velocity stepping test but operating at a slip rate relevant to our dynamic rupture experiment.

5.2 Quantification of the wire explosion

The importance of quantifying rupture nucleation mechanism has been mentioned many times throughout the entire thesis, either from the modeling perspective or experimental perspective. The three signature features of the exploding wire technique: small affected region, short duration, and high intensity, make the quantification very challenging. It is possible that the wire explosion may open a small part of the interface around the explosion, initiating a small opening crack in the middle of the interface. We would need to quantify this effect of the magnitude and shape of normal stress reduction (as shown in Fig. 5.4). An array of velocity measurement points would surround the nucleation region and the velocity histories would be recorded for the inversion analysis. Based on the Green's function approach, the distributed nucleation intensity (which is also a function of time) could then be inferred numerically.

We have conducted two preliminary tests to measure the velocity response at horizontal and vertical directions as shown in Fig. 5.5. Since the horizontal interface is used, there is no frictional sliding involved in this test and all the information is due to the explosion only. There are several interesting features in the recordings. First of all, the initial velocity spike in the vertical measurement is two times larger than the horizontal counterpart. This indicates that the wave front generated by the explosion is not axisymmetric. This is consistent with the hypothesis that part of the interface would open. The second notable feature is the good repeatability of the measurement. Two independent experiments yield similar profiles of the velocity history as evident in Fig.5.5. The third feature

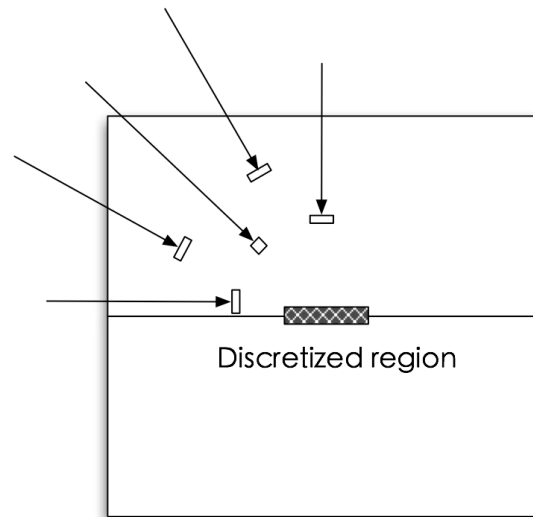


Figure 5.4: Proposed quantification of the explosion. An array of velocimetry measurement locations is positioned around the explosion site. The effect nucleation region is modeled as a distributed zone. Through numerical inversion, we plan to quantify the details of nucleation mechanism, such as strength and duration.

is the periodic oscillations which are likely coming from the 3D effect discussed in Chapter 3. These preliminary measurements show that this explosion quantification design would work. We are optimistic that with more measurements in the future, the rupture nucleation procedure, as well as friction properties as discussed in section 5.1, can be well constrained and integrated into modeling presented in Chapter 4 for more rigorous comparisons with experiments.

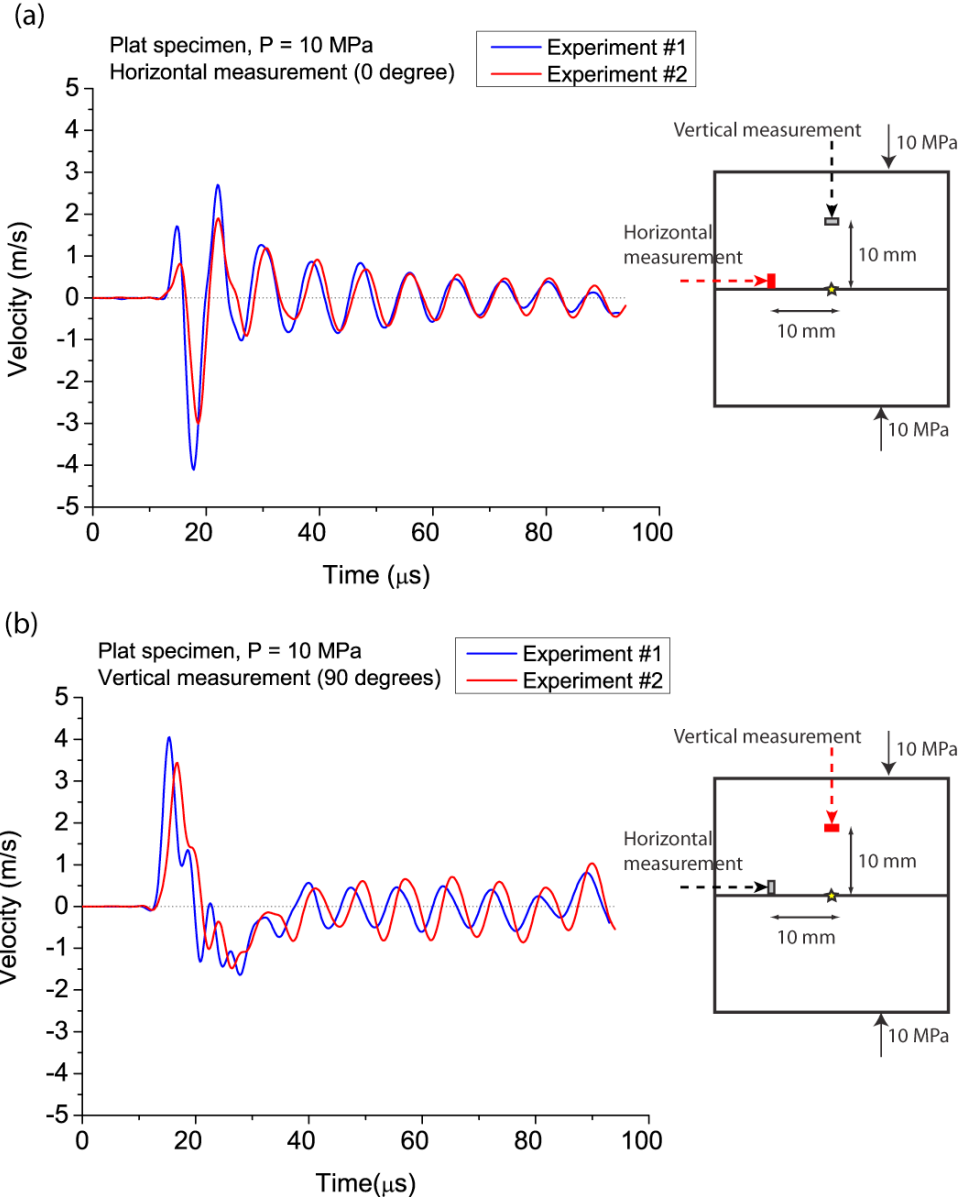


Figure 5.5: Preliminary velocimetry measurements for explosion quantification. Two laser beams are positioned along horizontal and vertical as shown. For a horizontal interface, there is no sliding, hence the measurement is entirely the response to the explosion. Two independent experiments are conducted to prove the good repeatability of the measurements. The fact that the vertical measurement has higher initial peak indicates that the wave front of the explosion is not perfectly axisymmetric.

5.3 Effect of inhomogeneities and complex fault geometries on rupture dynamics

In this thesis, most of the experiments and simulations are based on the homogeneous fault system. However, from field observations, the Earth crust is known to be highly inhomogeneous with a distribution of strong and weak patches. The local length of these strong/weak patches can often be comparable to the rupture propagation length. That means that if some inhomogeneous patch is located around the fault line, the influence of such an inhomogeneity on rupture propagation cannot be ignored and needs to be treated carefully. One obvious effect of such inhomogeneities is that their pressure influences the local normal and shear stress distribution at the vicinity of the rupture region. The question that naturally arises is whether and how such driving stress inhomogeneities will affect the rupture propagation characteristics. Possible ways to do so include the suppression/delay/acceleration of the transition from sub-Rayleigh to supershear as well as the possibility of influencing the rupture mode by inducing transitions from crack-like to pulse-like rupture behavior. Here we consider the case of material inhomogeneities which reside on either side of the fault line and do not intersect the fault.

There are several possible methods to induce driving stress inhomogeneities in a controlled manner. The first one is to machine two identical holes above and below the interface separating a pair of Homalite-100 plates as in Figure 5.6a. In this figure the connecting line of the two centers of the holes is chosen to be perpendicular to the interface.

Problem variables controlling the magnitude and the width of the inhomogeneity can be the distance between the holes as well as the hole diameters. The distance of the holes pair relative to the hypocenter can serve as another variable. For far-field load levels and fault plane angles corresponding to sub-Rayleigh to supershear rupture speed transitions (Xia, Rosakis and Kanamori, 2004), this distance can be chosen to be of the order of the transition length. This would allow us to directly observe the effect of local stress field reduction on suppressing the transition to supershear. Stiffer material, such as steel, can also be inserted into the hole to form a strong patch; while softer or porous material can be inserted to simulate a weak or more compliant patch. The velocimeters will also be integrated with the high-speed photography technique to investigate the rupture pattern at different locations. It is interesting to investigate whether the crack-like to pulse-like mode transitions can be triggered or suppressed by the presence of such local driving stress reduction or enhancements. An alternative way to induce stress inhomogeneities is to machine periodic arrays of holes at some region adjacent to the interface as shown in Figure 5.6b. The goal of this method is to decrease the local stiffness of the Homalite plate introducing periodic hole patterns of certain dimensions and density. Under far-field pressure loading, these small holes will deform and induce an inhomogeneous normal and shear stress distribution along the fault. The density and diameter of these periodic holes will serve as the variables controlling the magnitude and periodicity of the stress inhomogeneity.

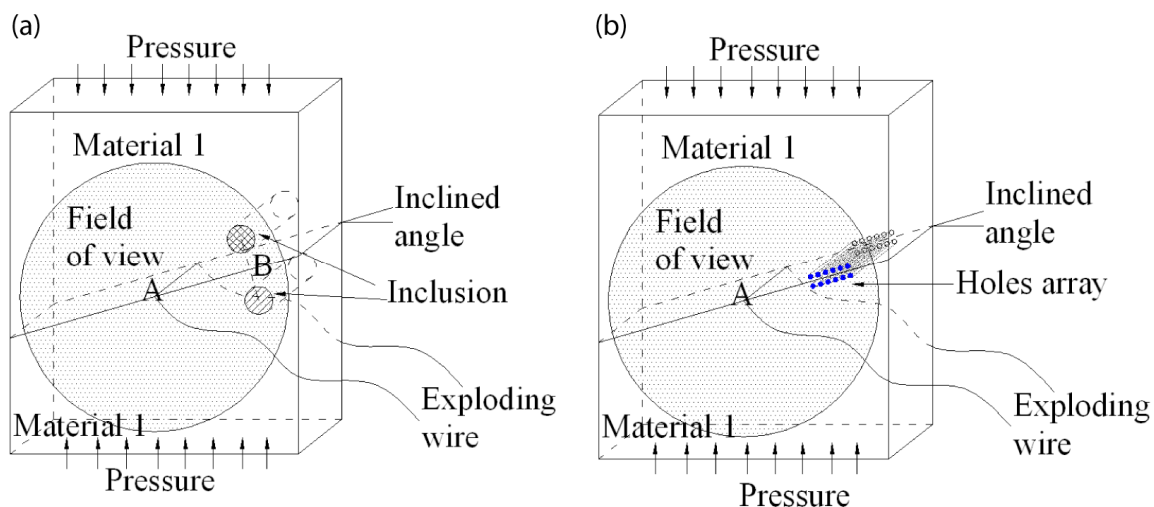


Figure 5.6: Stress inhomogeneities due to inclusions in the bulk of the material (a) Strong and weak patches model. (b) Array of holes model.

Different from local stress reduction or enhancement effects discussed above, this stress inhomogeneity can also be achieved by inducing various types of far field tectonic loading. Two representative cases are shown in Figure 5.7. These two cases correspond to (1) high driving stress near the nucleation region and low driving stress elsewhere (Figure 5.7a); (2) high driving stress on one side and low driving stress on the other (Figure 5.7b). In the laboratory, such loading inhomogeneities can be achieved by inducing displacement boundary condition control. Instead of applying uniform pressure through a flat steel plate, the top surface of the steel block is machined to be of certain geometry, such as one containing a step in the middle. Although Saint-Venant's principle will affect the stress distribution and particularly smooth out the driving stress inhomogeneity, a substantial stress inhomogeneity due to the discontinuous far field loading is still expected to exist along the fault.

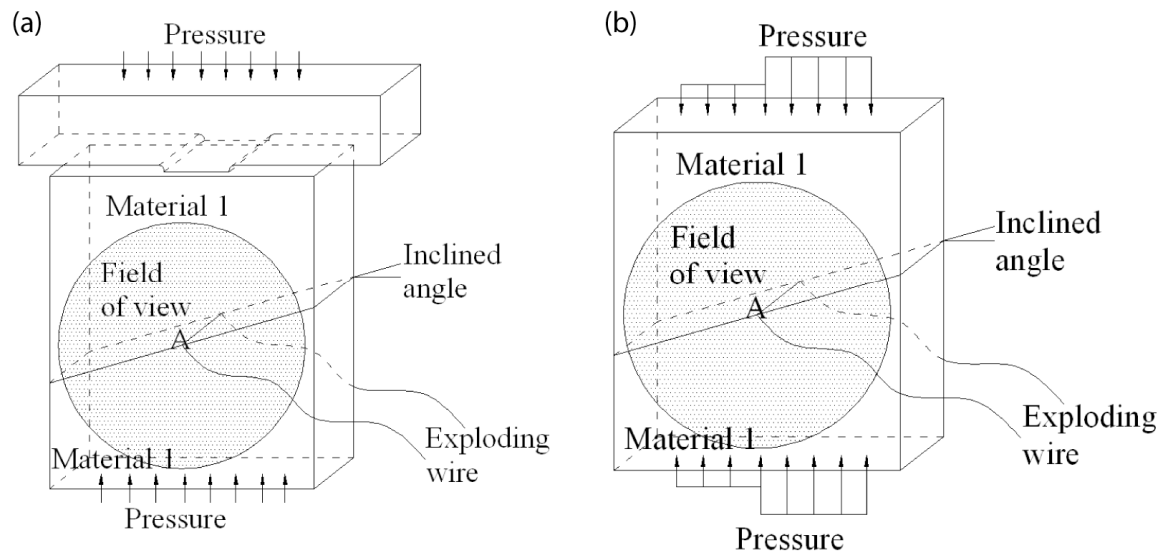


Figure 5.7: Inhomogeneous far-field loading: (a) High central stress (b) Step loading

We also consider controlled inhomogeneities in interfacial strength. In order to create variable heterogeneous interfacial strengths as described in Figure 5.8, glue and lubricant will be applied either periodically or randomly to an initially smooth interface. The rupture front will meet these interface strength inhomogeneities during propagation. Several interesting behaviors of the rupture, such as arrest/delay/acceleration, could be triggered by the interaction between the propagating rupture front and such inhomogeneities. The occurrence of various sliding modes, such as crack-like rupture, pulse-like rupture and multiple pulses, will also be investigated by velocimeters.

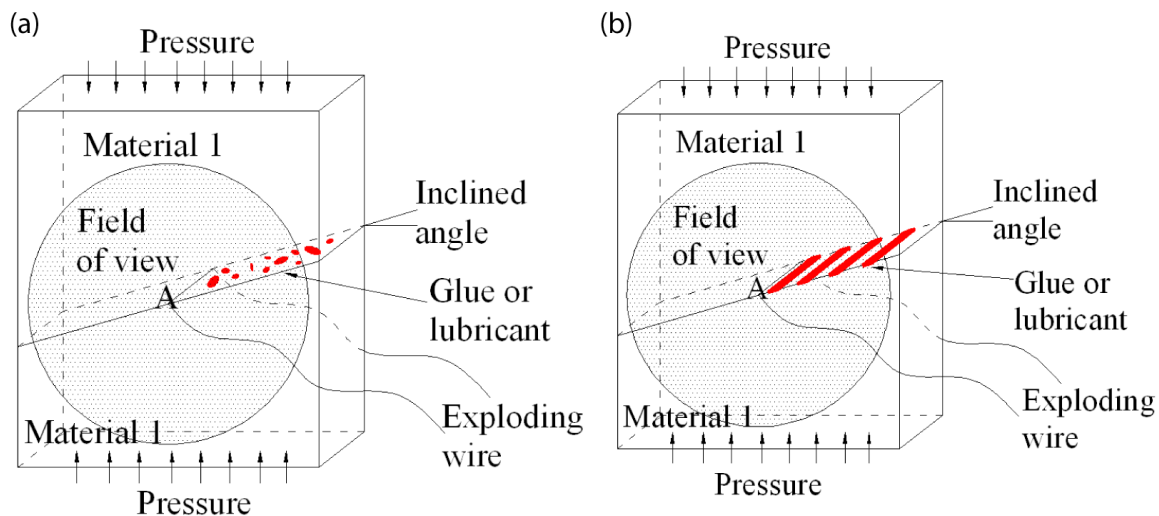


Figure 5.8: Interface strength inhomogeneity models: (a) Random dots (b) Periodic strips

In the current thesis, fault planes are assumed to be continuous and straight. However such idealized fault geometries are rarely present in real earthquakes. Actually, echelon, kinked and branched faults are prevalent in seismological observations. It is felt that it would be valuable to reproduce such more complex fault geometries in the laboratory so that their effect on rupture speed histories and sliding modes would be studied in a systematic way. During a single earthquake, rupture often jumps across several smaller faults segments. This phenomenon has been documented in relation to the 1966 Parkfield earthquake (Segall and Du, 1993), the 1999 Izmit, Turkey, earthquake (Harris, Dolan, Hartleb, and Day, 2000), and the 1992 Landers event (Zachariassen and Sieh, 1995). The field evidence in these cases suggests that rupture can jump between adjacent faults for stepover widths less than ~ 5 km. Similar results have been shown in the numerical work of Harris and Day (1999) who modeled the Izmit earthquake rupture which propagated over the segmented North Anatolian fault. The experiments are designed to visualize rup-

ture transmission across stepovers. The specimen can be constructed using several different techniques. One way would consist of machining the interfaces in a zigzag or 'z' pattern (Figure 5.9a). The sections representing the faults would be left to naturally mate by compression and friction, whereas the segment at the center would be bonded with a very strong adhesive having properties identical to those of the base material. Another way is to construct a multiple-layered system as in Figure 5.9b. The rupture could be triggered either on the top or on the bottom interfaces. Adhesive glue could be applied to the right side of the top interface thus creating a strong barrier retarding the rupture growth. In such a case the secondary interface could serve as the potential fault line for the rupture to jump to the bottom interface. Parameters such as stepover width and overlap will be chosen carefully to investigate the effect of offset geometries on the rupture speed. It should be noted that for the 1999 Chi-Chi earthquake, Ji, Helmberger, and Wald (2000) found evidence of offset induced slowdown while Wald and Heaton (1994) presented similar conclusions in relation to the 1992 Landers earthquake. It should also be mentioned that the experiments involve dimensions of the order of millimeters or centimeters compared to the kilometer length scales of offsets in the field. Appropriate scaling laws based on dimensional analysis may be able to relate our model laboratory results to real earthquake phenomena of the type described above.

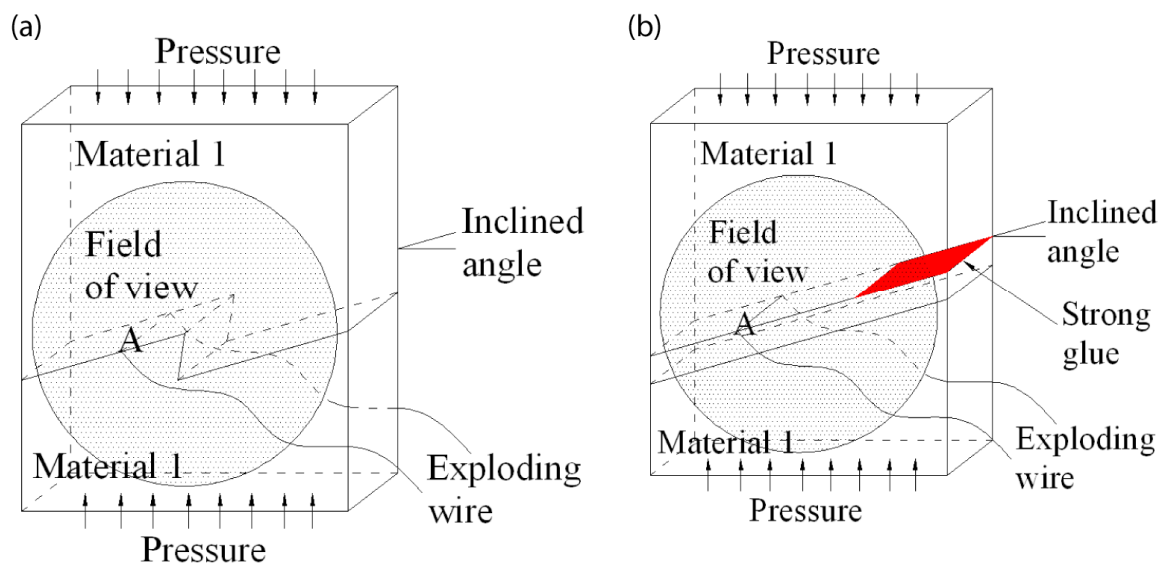


Figure 5.9: Complex Fault Geometries with steps and offsets (a) Zigzag fault system. (b) Multiple faults system

References

- Aagaard, B.T. & Heaton, T.H. (2004), Near-source ground motions from simulations of sustained intersonic and supersonic fault ruptures, *Bull. Seismol. Soc. Am.*, 94, 2064-2078.
- Abraham, F.F. & Gao, H. (2000), How fast can cracks propagate?, *Phys. Rev. Lett.*, 84, 3113-3116.
- Andrews, D. J., and Y. Ben-Zion (1997), Wrinkle-like slip pulse on a fault between different materials, *J. Geophys. Res.*, 102(B1), 553-571.
- Andrews, D.J. (1976), Rupture velocity of plane strain shear cracks, *J. Geophys. Res.*, 81, 5679-5687.
- Archuleta, R. J. (1984), A faulting model for the 1979 Imperial-Valley earthquake, *J. Geophys. Res.*, 89(NB6), 4559-4585.
- Beeler, N. M., and T. E. Tullis (1996), Self-healing slip pulses in dynamic rupture models due to velocity-dependent strength, *Bull. Seismol. Soc. Am.*, 86(4), 1130-1148.

- Ben-Zion, Y. (2001), Dynamic ruptures in recent models of earthquake faults, *J. Mech. Phys. Solids*, 49(9), 2209-2244.
- Bernard, P. & Baumont, D. (2005), Shear Mach wave characterization for kinematic fault rupture models with constant supershear rupture velocity, *Geophys. J. Int.*, 162, 431-447.
- Beroza, G. C., and T. Mikumo (1996), Short slip duration in dynamic rupture in the presence of heterogeneous fault properties, *J. Geophys. Res.*, 101(B10), 22449-22460.
- Bhat, H.S., Dmowska, R., King, G.C.P., Klinger, Y. & Rice, J.R. (2007), Off-fault damage patterns due to supershear ruptures with application to the 2001 M/sub w/ 8.1 Kokoxili (Kunlun) Tibet earthquake, *J. Geophys. Res., B, Solid Earth*, 112, 1-19.
- Bouchon, M. S., M. Bouin, H. Karabulut, M. Toksoz, M. Dieterich, and A. Rosakis (2001), How fast is rupture during an earthquake? New insights from the 1999 Turkey earthquakes, *Geophys. Res. Lett.*, 28(14), 2723-2726.
- Bouchon, M., and M. Vallee (2003), Observation of Long Supershear Rupture During the Magnitude 8.1 Kunlunshan Earthquake, *Science*, 301(5634), 824-826.
- Broberg, K.B. (1989), The near-tip field at high crack velocities, *Int. J. Fracture*, 39, 1-13.
- Burridge, R. (1973), Admissible speeds for plane-strain self-similar shear cracks with friction but lacking cohesion, *Geophys. J. Royal Astro. Soc.*, 35, 439-455.
- Burridge, R., G. Conn, and L. B. Freund (1979), Stability of a rapid mode-II shear crack with finite cohesive traction, *J. Geophys. Res.*, 84(NB5), 2210-2222.

- Cochard, A. D. L., and R. Madariaga (1994), Dynamic faulting under rate-dependent friction, *Pure Appl. Geophys.*, 142(3-4), 419-445.
- Cochard, A., and J. R. Rice (2000), Fault rupture between dissimilar materials: Ill-posedness, regularization, and slip-pulse response, *J. Geophys. Res.*, 105(B11), 25891-25907.
- Cochard, A., and R. Madariaga (1996), Complexity of seismicity due to highly rate-dependent friction, *J. Geophys. Res.*, 101, 25321-25336.
- Dally, J.W. & Riley, W.F. (1991), *Experimental stress analysis*, edn, Vol., pp. Pages, McGraw-Hill, New York.
- Das, S. (2007), The need to study speed, *Science*, 317, 905-906.
- Das, S., and K. Aki (1977), Numerical study of 2-dimensional spontaneous rupture propagation, *Geophys. J. Royal Astro. Soc.*, 50(3), 643-668.
- Day, S. M. (1982), Three-dimensional finite difference simulation of fault dynamics: Rectangular faults with fixed rupture velocity, *Bull. Seismol. Soc. Am.*, 72(3), 705-727.
- Day, S. M., G. Yu, and D. J. Wald (1998), Dynamic stress changes during earthquake rupture, *Bull. Seismol. Soc. Am.*, 88(2), 512-522.
- Day, S.M. (1982), 3-Dimensional simulation of spontaneous rupture - the effect of non-uniform prestress, *Bull. Seismol. Soc. Am.*, 72, 1881-1902.
- Di Toro, G., D. L. Goldsby, and T. E. Tullis (2004), Friction falls towards zero in quartz rock as slip velocity approaches seismic rates, *Nature*, 427(6973), 436-439.

- Dieterich, J. H. (1979), Modeling of rock friction. 1. Experimental results and constitutive equations, *J. Geophys. Res.*, 84(NB5), 2161-2168.
- Dieterich, J. H. (1981), *Constitutive properties of faults with simulated gouge*, in *Mechanical Behavior of Crustal Rocks, Geophysical Monograph*, AGU, edited by N. L. Carter, et al., pp. 103–120, Washington, DC.
- Dieterich, J. H., and B. D. Kilgore (1994), Direct observation of frictional contacts-new insights for state-dependent properties, *Pure Appl. Geophys.*, 143(1-3), 283-302.
- Dieterich, J. H., and B. D. Kilgore (1996), Imaging surface contacts: Power law contact distributions and contact stresses in quartz, calcite, glass and acrylic plastic, *Tectonophysics*, 256(1-4), 219-239.
- Dunham, E. M., and R. J. Archuleta (2005), Near-source ground motion from steady state dynamic rupture pulses, *Geophys. Res. Lett.*, 32(3), L03302.
- Dunham, E.M. & Archuleta, R.J. (2004), Evidence for a supershear transient during the 2002 Denali fault earthquake, *Bull. Seismol. Soc. Am.*, 94, S256-S268.
- Ellsworth, W.L., Celebi, M., Evans, J.R., Jensen, E.G., Kayen, R., Metz, M.C., Nyman, D.J., Roddick, J.W., Spudich, P. & Stephens, C.D. (2004), Near-field ground motion of the 2002 Denali fault, Alaska, earthquake recorded at Pump Station 10, *Earthquake spectra*, 20, 597-615.
- Festa, G., and J. P. Vilotte (2006), Influence of the rupture initiation on the intersonic transition: crack-like versus pulse-like modes, *Geophys. Res. Lett.*, 33(15), L15320.

- Freund, L.B. (1979), Mechanics of dynamic shear crack propagation, *J. Geophys. Res.*, 84, 2199-2209.
- Gao, H., Y. Huang, and F. F. Abraham (2001), Continuum and atomistic studies of inter-sonic crack propagation, *J. Mech. Phys. Solids*, 49(9), 2113-2132.
- Geubelle, P. H., and D. V. Kubair (2001), Intersonic crack propagation in homogeneous media under shear-dominated loading: numerical analysis, *J. Mech. Phys. Solids*, 49(3), 571-587.
- Geubelle, P. H., and J. R. Rice (1995), A spectral method for three-dimensional elastodynamic fracture problems, *J. Mech. Phys. Solids*, 43(11), 1791-1824.
- Harris, R. A., and S. M. Day (1993), Dynamics of fault interaction - parallel strike-slip faults, *J. Geophys. Res.*, 98, 4461-4472.
- Heaton, T. H. (1990), Evidence for and implications of self-healing pulses of slip in earthquake rupture, *Phys. Earth Planet. In.*, 64(1), 1-20.
- Ida, Y. (1972), Cohesive force across tip of a longitudinal-shear crack and Griffiths specific surface-energy, *J. Geophys. Res.*, 77(20), 3796.
- Johnson, E. (1992), The influence of the lithospheric thickness on bilateral slip, *Geophys. J. Int.*, 108(1), 151-160.
- Kostrov, B. V. (1966), Unsteady propagation of longitudinal shear cracks, *J. Appl. Math. Mech.*, 30(6), 1241.
- Lapusta, N., and J. R. Rice (2004), Earthquake sequences on rate and state faults with strong dynamic weakening, *Eos Trans. AGU*, 85(47), T22A-05.

- Lapusta, N., J. R. Rice, Y. Ben-Zion, and G. Zheng (2000), Elastodynamic analysis for slow tectonic loading with spontaneous rupture episodes on faults with rate- and state-dependent friction, *J. Geophys. Res.*, 105(B10), 23765-23789.
- Liu, Y., and N. Lapusta (2008), Transition of mode II cracks from sub-Rayleigh to inter-sonic speeds in the presence of favorable heterogeneity, *J. Mech. Phys. Solids*, 56(1), 25-50.
- Lu, X., Lapusta, N. & Rosakis, A.J., 2007. Pulse-like and crack-like ruptures in experiments mimicking crustal earthquakes, *Proceedings of the National Academy of Sciences of the United States of America*, 104, 18931-18936.
- Lu, X., Lapusta, N. & Rosakis, A.J. (2008), Analysis of supershear transition regimes in rupture experiments: the effect of nucleation conditions and friction parameters, *submitted to Geophys. J. Int.*
- Lu, X., Rosakis, A.J., & Lapusta, N. (2008), Rupture modes in laboratory earthquakes: effect of fault prestress and nucleation conditions, *manuscript in preparation*.
- Lu, X., N. Lapusta, and A. J. Rosakis (2005), Testing friction laws by comparing simulation results with experiments of spontaneous dynamic rupture, *Eos Trans. AGU*, 86(52), S32B-07.
- Lykotrafitis, G., A. J. Rosakis, and G. Ravichandran (2006), Particle velocimetry and photoelasticity applied to the study of dynamic sliding along frictionally-held bi-material interfaces: Techniques and feasibility, *Exp. Mech.*, 46(2), 205-216.
- Lykotrafitis, G., A. J. Rosakis, and G. Ravichandran (2006), Self-Healing Pulse-Like Shear Ruptures in the Laboratory, *Science*, 313(5794), 1765-1768.

- Madariaga, R. & Olsen, K.B. (2000), Criticality of rupture dynamics in 3-D, *Pure Appl. Geophys.*, 157, 1981-2001.
- Madariaga, R. (1976), Dynamics of an expanding circular fault, *Bull. Seismol. Soc. Am.*, 66(3), 639-666.
- Needleman, A., and A. J. Rosakis (1999), The effect of bond strength and loading rate on the conditions governing the attainment of intersonic crack growth along interfaces, *J. Mech. Phys. Solids*, 47(12), 2411-2449.
- Nielsen, S. B., J. M. Carlson, and K. B. Olsen (2000), Influence of friction and fault geometry on earthquake rupture, *J. Geophys. Res.*, 105(B3), 6069-6088.
- Nielsen, S., and R. Madariaga (2003), On the self-healing fracture mode, *Bull. Seismol. Soc. Am.*, 93(6), 2375-2388.
- Ohnaka, M. (2003), A constitutive scaling law and a unified comprehension for frictional slip failure, shear fracture of intact rock, and earthquake rupture, *Journal of Geophysical Research-Solid Earth*, 108(B2).
- Olsen, K. B., R. Madariaga, and R. J. Archuleta (1997), Three-Dimensional Dynamic Simulation of the 1992 Landers Earthquake, *Science*, 278(5339), 834-838.
- Perrin, G., J. R. Rice, and G. Zheng (1995), Self-healing slip pulse on a frictional surface, *J. Mech. Phys. Solids*, 43(9), 1461-1495.
- Prakash, V. (2004), Pilot studies to determine the feasibility of using new experimental techniques to measure sliding resistance at seismic slip rates, SCEC Annu. Prog. Rep. 2004, South. Calif. Earthquake Cent., Los Angeles.

- Prakash, V., and F. Yuan (2004), Results of a pilot study to investigate the feasibility of using new experimental techniques to measure sliding resistance at seismic slip rates, *Eos Trans. AGU*, 85(47), Fall Meet. Suppl., Abstract T21D-02.
- Rice, J.R, Ruina A.L. (1983). Stability of steady frictional slipping. *J. Appl. Mech.* 105:343–49.
- Rice, J. R. (1999), Flash heating at asperity contacts and rate-dependent friction, *Eos Trans. AGU*, 80(46), Fall Meet. Suppl., F6811
- Rice, J. R. (2006), Heating and weakening of faults during earthquake slip, *J. Geophys. Res.*, 111, B05311.
- Robinson, D. P., C. Brough, and S. Das (2006), The M-w 7.8, 2001 Kunlunshan earthquake: Extreme rupture speed variability and effect of fault geometry, *J. Geophys. Res.*, 111, B08303.
- Rosakis, A. J., K. W. Xia, G. Lykotrafitis, and H. Kanamori (2007), Dynamic Shear Rupture in Frictional Interfaces: Speeds, Directionality and Modes, in *Treatise in Geophysics*, edited by G. Schubert and H. Kanamori, Elsevier.
- Rosakis, A. J., O. Samudrala, and D. Coker (1999), Cracks faster than the shear wave speed, *Science*, 284(5418), 1337-1340.
- Rosakis, A.J. (2002), Intersonic shear cracks and fault ruptures, *Adv. Phys.*, 51, 1189 - 1257.
- Rosakis, A.J., Xia, K.W., Lykotrafitis, G. & Kanamori, H. (2007), Earthquake Seismology Dynamic Shear Rupture in Frictional Interfaces: Speeds, Directionality and Modes, in *Treatise in Geophysics*, eds. Schubert, G. & Kanamori, H. Elsevier.

- Ruina, A. (1983), Slip instability and state variable friction laws, *J. Geophys. Res.*, 88(NB12), 359-370.
- Samudrala, O., Y. Huang, and A. J. Rosakis (2002), Subsonic and intersonic shear rupture of weak planes with a velocity weakening cohesive zone, *J. Geophys. Res.*, 107(B8), 2170.
- Shi, Z. Q., and Y. Ben-Zion (2006), Dynamic rupture on a bimaterial interface governed by slip-weakening friction, *Geophys. J. Int.*, 165(2), 469-484.
- Shi, Z., Y. Ben-Zion, and A. Needleman (2008), Properties of dynamic rupture and energy partition in a solid with a frictional interface, *J. Mech. Phys. Solids*, 56(1), 5-24.
- Tsutsumi, A., and T. Shimamoto (1997), High-velocity frictional properties of gabbro, *Geophys. Res. Lett.*, 24(6), 699-702.
- Tullis, T. E., and D. L. Goldsby (2003), Flash melting of crustal rocks at almost seismic slip rates, *Eos Trans. AGU*, 84(46), S51B-05.
- Xia, K.W., Rosakis, A.J. & Kanamori, H. (2004), Laboratory earthquakes: The sub-Rayleigh-to-supershear rupture transition, *Science*, 303, 1859-1861.